Aston University

Some pages of this thesis may have been removed for copyright restrictions.

If you have discovered material in AURA which is unlawful e.g. breaches copyright, (either yours or that of a third party) or any other law, including but not limited to those relating to patent, trademark, confidentiality, data protection, obscenity, defamation, libel, then please read our Takedown Policy and contact the service immediately

Numerical modelling of devices and advanced transmission schemes embracing Raman effect

Nayot Kurukitkoson

Doctor of Philosophy

Aston University

January 2004

This copy of the thesis has been supplied on condition that anyone who consults it is understood to recognise that its copyright rests with its author and that no quotation from the thesis and no information derived from it may be published without proper acknowledgement.

Aston University

Numerical modelling of devices and advanced transmission schemes embracing Raman effect

Nayot Kurukitkoson
Doctor of Philosophy

January 2004

Summary

This thesis presents a theoretical investigation on applications of Raman effect in optical fibre communication as well as the design and optimisation of various Raman based devices and transmission schemes. The techniques used are mainly based on numerical modelling. The results presented in this thesis are divided into three main parts.

First, novel designs of Raman fibre lasers (RFLs) based on Phosphosilicate core fibre are analysed and optimised for efficiency by using a discrete power balance model. The designs include a two stage RFL based on Phosphosilicate core fibre for telecommunication applications, a composite RFL for the 1.6 μm spectral window, and a multiple output wavelength RFL aimed to be used as a compact pump source for flat gain Raman amplifiers. The use of Phosphosilicate core fibre is proven to effectively reduce the design complexity and hence leads to a better efficiency, stability and potentially lower cost.

Second, the generalised Raman amplified gain model approach based on the power balance analysis and direct numerical simulation is developed. The approach can be used to effectively simulate optical transmission systems with distributed Raman amplification.

Last, the potential employment of a hybrid amplification scheme, which is a combination between a distributed Raman amplifier and Erbium doped amplifier, is investigated by using the generalised Raman amplified gain model. The analysis focuses on the use of the scheme to upgrade a standard fibre network to 40 Gb/s system.

Keywords: Nonlinear Optics, Raman effect, Raman Amplification, Raman Fibre Lasers, Hybrid Amplification

To Mum and Dad

"Many of life's failures are people who did not realize how close they were to success when they gave up."

—Thomas Edison (1847–1931)

Acknowledgements

This research was inspired by those minds who worked tirelessly to search for the light of inventions. I honour them.

I would like to express my gratitude and sincere thanks to many people involved in various parts of this research both directly and indirectly, since the first day of my study towards a PhD degree in the Photonics Research Group at Aston University, Birmingham until the preparation of this thesis presentation.

First of all, the deepest and most grateful sense of appreciation is due to Dr. Sergei Turitsyn, my supervisor, for his guidance, encouragement and understanding. It was a privilege to work with him, who always impressed me with his wealth of original ideas and perceptive visions. Special thanks go to Prof. Keith Blow for many profound discussions especially during the initial stage of my study and for his support in various ways.

I would like to thank my collaborators and co-authors of my papers whose contributions have brought about numerous successes in our research works. First of all, I acknowledge an immensely appreciable support of Prof. Andrew Kurkov and his colleagues from the Russian Academy of Science, Moscow who provided some experimental results presented in this thesis. I thank Dr. Erwan Pincemin and colleagues from France Telecom for some collaborations in the works on high speed transmission systems.

I am much indebted to Dr. Marc Eberhard and Dr. Vladimir Mezentsev for their continuing encouragement, friendship and support, particularly in the development of my skill and knowledge in Object-Oriented Programming for scientific computing.

I thank Dr. Hiroto Sugahara for his long-lasted friendship and invaluable discussions during my first year at Aston. Dr. Waiyapot Suttawassuntorn deserves special thanks for his continuous support in many ways both academically and socially.

I owe much gratitude and deep appreciation to Dr. Juan Diego Ania Castañón for his time and labour in answering my questions, discussions and proof-reading of this thesis. His kind personality and friendship are deeply appreciated.

Many thanks go to student fellows and staff members of the Photonics Research Group who helped create a wonderful research environment that has also made my stay in the wonderful City of Birmingham much more memorable. Dr. Sonia Boscolo often came to my office to offer her regular greeting and computer problems. Dr. Andy Lee, Yicheng Lai, Dr. Wai Mun Wong, Filip Floreani, Dr. Stanislav Derevyanko, Ashley Grey, Ranjeet Bhamber and Supun Athukorale must be acknowledged for having helped create an impressive international environment and their long moral supports. I thank Rachel Won who is both my colleague and flatmate for her friendship and patience when the Thai community came to cook in our kitchen. Her curious mind has also intrigued me many times and often led to an understanding of various theory.

I would like to dedicate my special thanks to a number of people who has continuously supported my research and life in the UK. First of all, I would like to thank Prof. Monai Krairiksh of ReCCIT, KMITL, Thailand for his generosity in letting

me use his laboratory and facility when I was spending my holiday in Thailand. My sincere thanks go to Dr. Komsak Meksamoot, Amorn Jiraseree-Amornkun, Panisa Keowsawat and Arkhom Suvannakita for their everlasting friendship and moral support. Without them, I would not have made this far in the academic career. I thank Thaveesub Laoamornpanich who, in spite of being often relocated to many strangest places on this planet, always gave me a shout when he came back to the civilisation. I would also like to thank Srisupa Palakvangsa-Na-Ayudhya, my first friend in the UK, for her continuous support and wonderful friendship. Special thanks go to both past and present members of Thai community at Aston. Our wonderful community has impressed me so much, and it helped compensate for the feeling of being so far away from home.

I would like to acknowledge the Royal Thai government for their financial support through a Royal Thai government scholarship.

I feel so much grateful to my family, my father Montri and my brother Chayoot. Their open-minds, to have allowed me experimenting around with household electrical and electronic appliances during my childhood, gave me a chance to fall in love with science and engineering that have finally become my obsessive career. My success is always dedicated to my mother Bhairoh who does not live to see her result of lifetime affords in raising a son.

Last but not least, I specially thank my beloved Ampa Thanuthanomrad for her patience and understanding in the way of my academic career and the time I spent abroad without her.

Contents

1 **Introduction** **15**
- 1.1 Historical perspective . . . 15
- 1.2 Thesis outline . . . 24

2 **Optical fibres and optical communication** **27**
- 2.1 Introduction . . . 27
- 2.2 Optical fibre characteristics . . . 27
  - 2.2.1 Optical losses . . . 29
  - 2.2.2 Chromatic dispersion . . . 31
  - 2.2.3 Fibre nonlinearities . . . 34
- 2.3 Wave propagation in optical fibres . . . 36
- 2.4 Impact of important effects in optical communication . . . 40
  - 2.4.1 Group velocity dispersion . . . 41
  - 2.4.2 Higher order dispersion . . . 44
  - 2.4.3 Self phase modulation and cross phase modulation . . . 47
- 2.5 Conclusions . . . 48

3 **Raman effect in optical fibre** **50**
- 3.1 Introduction . . . 50
- 3.2 Raman effect: The historical perspective . . . 52
- 3.3 Spontaneous scattering of light in material media . . . 54
- 3.4 Stimulated Raman scattering . . . 56
  - 3.4.1 Classical model of stimulated Raman scattering . . . 57
  - 3.4.2 Power balance model for Raman amplification . . . 63
  - 3.4.3 Effective core area for stimulated Raman scattering . . . 66
  - 3.4.4 Transient stimulated Raman scattering . . . 67
- 3.5 Noise in Raman amplification . . . 71
- 3.6 Conclusions . . . 73

4 **Raman fibre lasers** **76**
- 4.1 Introduction . . . 76
- 4.2 Modelling of Raman fibre lasers . . . 77
- 4.3 Single stage Raman fibre laser . . . 80
- 4.4 Two stage Raman fibre laser based on Phosphosilicate core fibre . . . 83
  - 4.4.1 Laser characteristics . . . 84
  - 4.4.2 Cavity optimisation . . . 86

4.4.3 Full scale optimisation 87
4.4.4 Tolerance of the optimal regime 89
4.4.5 Laser threshold 90
4.4.6 Comparison with experimental results 92
4.5 Efficiency spectrum comparison between Ge- and P-doped Raman fibre laser 92
4.6 Composite Raman fibre laser for 1.6 μm spectral window 95
4.6.1 Laser design 96
4.6.2 Cavity modelling and laser characteristics 97
4.6.3 Comparison with the experimental results 99
4.6.4 Optimisation of the composite Raman fibre laser 100
4.7 Multiple output wavelength Raman fibre laser 102
4.7.1 Laser design 104
4.7.2 Analysis and optimisation of Phosphosilicate section 105
4.7.3 Multiple output wavelength section: cavity modelling 107
4.7.4 Cavity optimisation 110
4.7.5 Characteristics of the optimal regime 111
4.8 Conclusions 113

5 Modelling of Raman amplification in optical transmission systems 116
5.1 Introduction 116
5.2 Generalised Raman amplified gain model 117
5.2.1 Full frequency power balance model 119
5.2.2 Effective attenuation 120
5.3 Direct numerical simulation model of the Raman amplified transmission system 123
5.3.1 Incorporation of the generalised Raman gain into the nonlinear Schrödinger equation 124
5.3.2 Normalisation of the nonlinear Schrödinger equation 124
5.3.3 Noises in Raman amplified transmission line 125
5.4 Conclusions 129

6 Upgrade of a standard fibre network to 40 Gb/s per channel using a hybrid amplification scheme 131
6.1 Introduction 131
6.2 Nonlinearity management 133
6.2.1 Optimisation of the system configuration using the average power approach 134
6.2.2 Direct numerical analysis 136
6.3 Impact of the dispersion maps on the transmission performance . . . 139
6.3.1 Comparison of the dispersion map performance 140
6.3.2 Transmission performance under the optimal configuration . . 143
6.4 Optimisation of the span average dispersion 143
6.5 Conclusions 148

7 Conclusions 150

A Fibre specification and data summary 156

B Split-step Fourier method 160

C Modelling of some important devices in the optical transmission system 164

Publications 174

Bibliography 176

Abbreviations

ASE	amplified spontaneous emission
AGWN	additive Gaussian white noise
BER	bit-error rate
BVP	boundary value problem
CW	continuous wave
DCF	dispersion compensating fibre
DDM	dense dispersion management
DM	dispersion management
DRA	distributed Raman amplifier
DSF	dispersion shifted fibre
EDFA	Erbium doped fibre amplifier
FBG	fibre Bragg grating
FEC	forward error correction
FWM	four-wave mixing
FWHM	full-width at half maximum
GVD	group velocity dispersion
MFD	mode field diameter
NF	noise figure
NLS	nonlinear Schrödinger equation
NOLM	nonlinear optical loop mirror
NPS	nonlinear phase shift
NRZ	non-return-to-zero
ODE	ordinary differential equation
OSNR	optical signal-to-noise ratio
PMD	polarisation mode dispersion
PRBS	pseudo-random bit sequence
RFL	Raman fibre laser
RMS	root mean square
RZ	return-to-zero
SBS	stimulated Brillouin scattering
SMF	single mode fibre
SNR	signal-to-noise ratio
SPM	self-phase modulation
SRS	stimulated Raman scattering
TDM	time division multiplexing
WDM	wavelength division multiplexing
XPM	cross-phase modulation

List of Figures

2.1 Parts of fibre optics cable (not to scale) 28
2.2 Loss profile of a single mode fibre 30
2.3 Attenuation curves for some modern transmission fibres. (after Ref. [28] ©2003 Springer) 31
2.4 Dispersion parameter D versus wavelength for serveral commercial fibre types. (after Ref. [28] ©2003 Springer) 34
2.5 Pulse broadening due to GVD in the absence of loss and nonlinearity. The launched pulse has Gaussian shape with an initial pulse width of 12.5 ps and the peak power of 1 mW 42
2.6 Single pulse propagation in a lossless dispersion managed line. 45
2.7 Variation of chirp parameter with propagated distance for a Gaussian pulse under a dispersion management. 45
2.8 Effect of the third order dispersion on a Gaussian pulse with an initial pulse width of 12.5 ps propagated in a fibre in the absence of loss, nonlinearity and k''. The solid curve represents the initial pulse at $z = 0$ km and the dashed curve represents the pulse at $z = 4\ L'_D \simeq 22,000$ km 46
2.9 Optical spectra of a Gaussian pulse with an initial pulse width of 12.5 ps propagated in a fibre in a presence of SPM only. Solid, dashed and dotted curves represent the spectrum at $z = 0, z = 10\ L_{NL}$ and $z = 20\ L_{NL}$ where $L_{NL} \simeq 1000$ km, respectively. 48

3.1 Comparison between signal energy evolution in an optical fibre with EDFAs (dashed line) and backward pumped DRAs (solid line). The amplifier spacing is 100 km. 52
3.2 Light scattering. (a) Spontaneous scattering. (b) Cancellation of scattered lights in a completely homogeneous medium. 55
3.3 Spectrum of light scattering in a medium. 56
3.4 Quantum picture of Raman scattering. 57
3.5 Molecular description of stimulated Raman scattering. 58
3.6 Raman gain spectrum obtained from the single-damped-oscillator model (solid curve) compared to a measured Raman gain (dashed curve) . . 62
3.7 Measured Raman gain spectrum for fused silica at a pump wavelength $\lambda_P = 1\mu$m. (after Ref. [47] ©1980 IEEE) 65

3.8 Raman gain efficiency spectra for some commercial transmission fibre. The spectra were measured with a reverse-pump at 1455 nm. (after Ref. [28] ©2003 Springer) 66
3.9 Comparison between the temporal variations of the Raman response function $h_R(t)$ (a) given by the single-damped-oscillator model and (b) obtained by the actual Raman gain spectrum of silica glass. . . . 68

4.1 Schematic diagram of Raman fibre lasers. 78
4.2 Problem definition for the Raman fibre laser power balance model. . . 79
4.3 Output power characteristic comparison between the experiment (square dot) and values predicted by the power balance model for a single stage RFL with $L = 500$ m (solid line). 82
4.4 Output power characteristic comparison between the experiment (square dot) and values predicted by the power balance model for a single stage RFL with $L = 1000$ m (solid line). 82
4.5 Raman gain spectrum comparison between the P-doped (solid curve) and Ge-doped (dash curve) fibres. 84
4.6 Schematic diagram of the two-stage RFL based on P-doped fibre. . . 85
4.7 Power evolution of forward (right arrow) and backward (left arrow) pump and Stokes waves. Dashed, dash-dotted, and solid lines represent the pump, 1st- and 2nd-order Stokes powers, respectively. (a) $R_{out} = 15\%$ (b) $R_{out} = 1\%$ (c) $R_{out} = 50\%$. 86
4.8 Optimal reflectivity versus input power 88
4.9 Conversion efficiency versus input power 88
4.10 Contour plots of the conversion efficiency at several P_{in} 89
4.11 Tolerance of the RFL performance to the deviation in (a) the reflectivity of output coupler ($L = 500$ m) (b) the cavity length ($R_{out} = 15\%$) 90
4.12 Laser threshold variation as a function of (a) cavity length (b) output reflectivity and (c) optimal laser configuration for various input power. 91
4.13 Comparison of the experimental results and simulations ($R_{out} = 15\%, L = 500$ m) 92
4.14 Slope efficiency spectrum of (a) Yb-doped fibre laser (b) Ge-doped (DCF) and P-doped RFLs 94
4.15 Total slope efficiency of the RFLs pumped by the Yb-doped double clad fibre laser (solid line ≡ 5-stage Ge-doped, dotted line ≡ 6-stage Ge-doped, dashed line ≡ P-doped RFLs) 95
4.16 Schematic diagram of the composite Raman fibre laser. 97
4.17 Problem definition of the composite Raman fibre laser. 98
4.18 Power evolution of forward (right arrow) and backward (left arrow) pump and Stokes waves with in the cavity of composite Raman fibre laser. 100
4.19 Output power of the composite RFL versus the output power of Yb-laser. Square dots represent the experimental results and the solid line is numerical prediction. 101
4.20 Output power characteristics of the composite RFL optimised at various input powers. 102

4.21 Gain-flattened three pump Raman amplifier schematic diagram. . . . 103
4.22 Gain spectrum of the three pump Raman amplifier. 103
4.23 Schematic diagram of the multiple output wavelength composite Raman fibre laser. 105
4.24 Problem definition of the multiple output wavelength composite Raman fibre laser. 105
4.25 Conversion efficiency contour of the P-doped stage for a number of input powers. (a) $P_{in} = 2$ W, (b) $P_{in} = 3$ W, (c) $P_{in} = 4$ W and (d) $P_{in} = 5$ W. 107
4.26 Conversion efficiency of the multiple output wavelength stage as a function of its cavity length. 111
4.27 Variation of conversion efficiency against the deviation of output powers from their optimal settings. (a) Fixed P_{out5} (b) Fixed P_{out4} (c) Fixed P_{out3}. 112
4.28 Optimal cavity length for various power partition settings. 113

5.1 Deterministic power signals and pumps in a considered frequency window. 118
5.2 Forward propagating power signal evolution of a Raman amplified 4–ch WDM system with a backward pump. 121
5.3 Power spectra (a) forward propagation at $z = 0$ km (b) backward propagation at $z = 0$ km (c) forward propagation at $z = 100$ km (d) backward propagation at $z = 100$ km. 121
5.4 Example of the effective attenuation. 123
5.5 Representation of noise field in the numerical simulations. 127
5.6 Autocorrelation of the piecewise noise field $< U(\Omega)\ U^*(\Omega') >$. 127
5.7 Signal representation in time and frequency domain. 128

6.1 Hybrid amplification system schematic. 134
6.2 Superimposed contour plots for the OSNR and the NPS versus input signal and η. The think line follows the optimal input signal for each η. 135
6.3 Signal energy evolution in the transmission path with hybrid amplification. $\eta = 0.55$. 137
6.4 Contour plot showing the maximum propagation distance (in km) versus η and input peak power. Note that the maximum distance is determined from the worst channel. 138
6.5 Q-factor evolution of each channel. The inset figure shows the eye diagram of channel 2 at 1400 km. 138
6.6 Dispersion map. 140
6.7 Schematic diagram of the 3-map transmission. 141
6.8 Plot of $\log(BER)$ against launch peak power for different dispersion map after three map periods. 142
6.9 Contour plot showing the optimal error-free transmission distance for the symmetric map (Map 1) against the launch peak power and η. (a) Error-free distance determined from the worst channel. (b) Error-free distance determined from the middle channel (channel 8). 144

6.10 Contour plot showing the optimal error-free transmission distance for the asymmetric map (Map 2) against the launch peak power and η. (a) Error-free distance determined from the worst channel. (b) Error-free distance determined from the middle channel (channel 8). 144
6.11 Schematic diagram of the 8 × 40 Gb/s system. 145
6.12 Contour plot showing the optimal error-free transmission distance for the symmetric map (Map 1) against the launch peak power and span average dispersion. (a) Error-free distance determined from the worst channel. (b) Error-free distance determined from the middle channel (channel 4). 146
6.13 Contour plot showing the optimal error-free transmission distance for the asymmetric map (Map 2) against the launch peak power and span average dispersion. (a) Error-free distance determined from the worst channel. (b) Error-free distance determined from the middle channel (channel 4). 147

A.1 Attenuation vs. wavelength of the G. 652 SMF. 157
A.2 Raman gain coefficient of the G. 652 SMF measured at the pump wavelength of 1 μm. 157
A.3 Attenuation vs. wavelength of the DCF. 158
A.4 Raman gain coefficient of the DCF measured at the pump wavelength of 1420 nm. 159

B.1 Temporal signal field. 163
B.2 Spectral signal field. 163

C.1 Example of the 5th order Bessel electrical filter. (a) The magnitude of the transfer function. (b) Phase of the transfer function. 168
C.2 Evaluation of the Q-factor from an eye diagram. 170
C.3 Algorithm to determine the value Q-factor from a sequence of data signal. 173

List of Tables

2.1 Characteristics of some commercial fibres. 29

4.1 Spectral band under 0.3 dB/km loss in ordinary single mode optical fibre 77
4.2 Fibre parameters for the single stage RFL. 81
4.3 Simulation parameters 85
4.4 Simulation parameters of the first stage (P-doped fibre). 99
4.5 Simulation parameters of the second stage (DSF). 99
4.6 Optimal parameters of the composite RFL optimised for some input powers 101
4.7 Simulation parameters for the first section (P-doped fibre) of the multiple output wavelength composite Raman fibre laser. 106
4.8 Simulation parameters for the first section (P-doped fibre) of the multiple output wavelength composite Raman fibre laser. 106
4.9 Attenuation parameters used in the simulation of the second section (Ge-doped fibre) of the multiple output wavelength composite Raman fibre laser. 109
4.10 Raman gain coefficients used in the simulation of the second section (Ge-doped fibre) of the multiple output wavelength composite Raman fibre laser. 109

A.1 Single mode fibre G. 652 specification. 156
A.2 Dispersion compensating fibre specification. 158

Chapter 1

Introduction

1.1 Historical perspective

During the fundamental transformation inherent in globalisation, the definition of telecommunication has to be extended to an integration of all media establishing integrated service networks. Technological advancement in the areas of telecommunication has increased the reliance on telecommunications and information technology in every area of human life, in all sectors of economic and social activity, and in the pursuit of knowledge and the expression of culture.

From an engineering point of view, that global telecommunication and information technology revolution has resulted in a surge of data traffic and has greatly increased the demand for ultra-high speed transmission links. Optical communication has been proven to be the only reasonable choice to meet such a demanding requirement [1]. Optical fibre can transmit ultra high speed information with extremely low loss over a wide range of wavelengths. By virtue of this outstanding property, fibre-optic communication technologies have been applied to a variety of transmission systems throughout the world, such as international undersea networks and terrestrial links [2, 3].

The deployment of optical fibre cable in telecommunications was boosted by the invention of lasers in 1960's [1]. Since then the physical properties of optical fibres have been studied intensively. Lightwave is guided within an optical fibre core by total internal reflection at the interface between the core possessing a higher refractive index and the cladding layer with a lower refractive index.

In the early years of this technology, the signal propagating in an optical fibre suffered a great deal of fibre loss, which exceeds 1000 dB/km. The loss was due to a presence of impurities in the fibre material. It was, however, proposed in 1966 that the loss could be minimised to the possible limiting point for transmission medium [4]. The significant revolution of optical fibre began in 1970 when a silica fibre exhibiting 20 dB/km loss could be fabricated [5]. At present, modern optical fibres have the minimum loss of approximately 0.2 dB/km in the vicinity of 1.55 μm. The loss is mainly contributed by material absorption in the far-infrared region and Rayleigh scattering arising from random density fluctuations that take place during fibre fabrication. Pure silica absorbs light at a wavelength around 2 μm, while Rayleigh scattering loss is dominant at short wavelengths.

A finite number of guided modes are supported by the optical fibre. The lowest mode is HE_{11} followed by TE_{01} and TM_{01}. When more than two guided modes propagate simultaneously in an optical fibre, the received signal suffers a distortion because each mode propagates with different speed and hence arrives at different time. This phenomenon arising from velocity mismatch of each mode is known as intermodal or multimode dispersion which limits the transmission speed and distance. However, when the core diameter of the optical fibre gets smaller, only the lowest mode is allowed to propagate so that the multimode dispersion would disappear. An optical fibre that supports only one mode of propagation is known as a single mode fibre (SMF).

Although the intermodal dispersion is not present in SMF, there still exists an inherent dispersion in which the refractive index changes slightly with frequency. The phenomenon is recognised as chromatic dispersion. This type of dispersion brings about a dependence of group velocity on frequency (or wavelength) resulting in a situation that different spectral components of an optical pulse propagate at different velocities leading to pulse broadening. As a result, the signal is distorted at the receiver end in a way similar to the intermodal dispersion. This phenomenon is referred to as group velocity dispersion (GVD).

Chromatic dispersion has two contributions: material dispersion and wave-guide dispersion. Material dispersion originates from the physical properties of silica, *i.e.* a retarded response of bound electrons in silica for lightwave electric fields which gives rise to the frequency dependence of the refractive index. On the other hand, waveguide dispersion arises from the geometry of the guided structure of the core radius. The latter thus allows optical fibre designers to achieve a desired dispersion profile by adjusting the geometry of the fibre core.

Although optical fibre has long been recognised as a linear device, it also exhibits some nonlinear phenomena when the light intensity is increased [6]. Nonlinear effects in optical fibres have been classified into two main categories: (1) nonlinear refractive index arising from the nonlinear electric polarisation of bound electrons in silica, and (2) stimulated inelastic scattering arising from an excitation of vibrational mode of silica molecules. Since silica based optical fibres do not exhibit second order nonlinear effects due to the inversion symmetry of molecules, third order nonlinearity (known as *Kerr* nonlinearity) is the lowest order nonlinear electric polarisation in optical fibres.

Kerr effect introduces an intensity dependence of refractive index resulting in an intensity dependent phase shift. The nonlinear phase shift introduced by the optical field over itself is called self-phase modulation (SPM) whereas the cross phase modulation (XPM) is a phase shift induced by other light copropagating with different frequencies or polarisations. These nonlinear phase shifts give rise to a spectral broadening and by interplaying with GVD may produce a considerable amount of pulse distortion.

In addition to phase modulation, when phase matching conditions are satisfied, the third order nonlinearity induces a parametric process referred to as four wave mixing (FWM), which results from a beating between two signals at different wavelengths, and creates new tones at other two wavelengths. This leads to inter-channel crosstalk in wavelength division multiplexing (WDM) systems. The effect reduces performance on WDM transmission and imposes a limit on its characteristics such as the number of channels and channel spacing.

As for the inelastic scattering processes, part of the incident energy is transferred to a vibrational mode excitation in silica, which eventually generates a scattered light wave with downshift frequency. Furthermore, once the incident power exceeds a threshold value, the power of scattered light grows exponentially. Stimulated Raman scattering (SRS) causes the energy transfer to optical phonons whereas stimulated Brillouin scattering (SBS) transfers the energy into acoustic phonons. Since the SBS scatters light in the backward direction, the threshold of SBS limits the launched optical power. On the one hand, the energy transfer among channels may result in an increase of noise or cross talks in communication systems. On the other hand, SRS can be turned to advantage as it has recently drawn a considerable attention due to its potential to provide amplification to high speed signals resulting in an improved transmission performance as well as to give birth to a number of applications relying on its principle [2, 6]

In the early stages of optical communication, the limiting factor of transmission speed and distance was intermodal dispersion [1]. To overcome this problem, SMF was deployed so that the higher order modes reach cutoff. This requires a core radius of less than 10 μm and fractional index change of less than 1% at the core-cladding interface. Since SMF exhibits zero dispersion at 1.3 μm, lightwave systems at an early age were initially operated at this wavelength.

Once intermodal dispersion was controlled, the next problem of the system in the beginning era was the fibre loss, which also became the main limiting factor for the transmission distance. Fortunately, advances in fibre fabrication technology have made possible low loss optical fibre with an attenuation of 0.2 dB at 1.55 μm. In the past, electronic regeneration has been employed periodically to compensate for the loss of optical fibres in transmission systems [1]. The regenerator consists of detectors, amplifiers and re-transmitters; all operate in electrical domain. However, the main problems of electronic regeneration are power requirements, bandwidth limitations and high costs. A remarkable breakthrough occurred in the early 1990s when Erbium-doped fibre amplifiers (EDFAs) were introduced and became commercially available [7]. These amplifiers allow direct amplification of optical signals without having to convert them to electrical domain. The systems therefore do not suffer from the limitation imposed by the electronic based amplifiers.

Because loss has become a major concern, transmission at the wavelength with lowest attenuation (0.2 dB at 1.55 μm) is preferable in spite of the non-zero chromatic dispersion. At some points, transmission turned from loss limited to dispersion limited instead. The difficulty was overcome by the invention of dispersion shifted fibres (DSFs) exhibiting minimum dispersion at 1.55 μm by controlling the waveguide dispersion. As discussed previously, this is possible through a careful design of the core structure so that the zero dispersion wavelength is shifted from 1.3 μm to the vicinity of 1.5 μm. Note that we have almost complete control over the choices of GVD values. It is thus possible to fabricate an optical fibre with the opposite sign of GVD that compensates for the high amount of accumulated GVD of the transmission fibre. These fibres are referred to as dispersion compensating fibres (DCFs).

In modern optical transmission systems, EDFAs are widely used to compensate for the losses. However, the EDFA itself introduces optical noise due to amplified spontaneous emission (ASE), which was not present in systems employing electronic repeaters. Therefore, a lightwave system deploying EDFAs must operate at relatively high power in order to refrain signal from being buried by the ASE noise. Such a high power enhances the significance of nonlinear effects that become the major problem in high-speed long-distance systems.

The first attempt to deal with nonlinear effects is to make the effects acceptably small by keeping signal power as low as possible and by using special dispersion maps. Dispersion Management (DM) is a technique that the transmission link is comprised with multiple sections of carefully chosen optical fibres with different lengths and GVDs. The technique allows a low average GVD of the entire link while keeping the local GVD (GVD of each segment) high enough to reduce the effects of SPM, XPM and FWM in the systems. The attempt aims to avoid the nonlinear effects and maintain the signal power to remain in the linear transmission regime. Optical modulation in non-return-to-zero (NRZ) bit format is generally used due to its narrower spectral bandwidth. However, at a high bit rate the NRZ bit format is found to be more susceptible to nonlinearity. Research shows that the return-to-zero (RZ) format is more tolerant to nonlinearity [8, 9] and consequently becomes more popular to be employed in high bit rate transmission systems. A pulse modulated in RZ format propagating through DM line is sometimes referred to as a chirped RZ pulse or nonlinear supported RZ pulse.

An alternative way to deal with nonlinearity is to turn it to advantage. In 1973, *Hasegawa* and *Tappert* [10] proposed and showed theoretically that stationary pulse propagation in optical fibre is possible. They derived the Nonlinear Schrödinger (NLS) equation for the propagation of the slowly varying envelope of an optical pulse in a fibre with the presence of dispersion and nonlinearity. The equation yields "soliton" solutions which can propagate undistorted along the fibre due to an interplay between GVD and nonlinearity. Solitons thus do not suffer from either pulse broadening in the presence of GVD or spectral broadening due to SPM. Moreover, the integrable nature of the NLS equation guarantees the stability of soliton propagation and at the same time indicates that any pulse of arbitrary shape launched with a proper amount of power evolves itself into a soliton during propagation. This also implies the robustness of soliton that can still preserve its properties even under the presence of periodic perturbations such as non-adiabatic loss and lumped amplification.

The discovery attracted profound interest as an ultimate solution to overcome the nonlinear effects in long haul high speed optical communication systems. However, soliton-based transmission unfortunately encounters some technical difficulties unique to solitons. One of the most serious issues is the phenomenon referred to as *Gordon-Haus* effect [11] which crucially limits the available capacity and transmission distance in soliton-based systems. Gordon-Haus effect is a timing jitter which originates from a random fluctuation of the carrier frequency of solitons caused by the nonlinear interaction with ASE noise.

Nonlinear interaction between two neighbouring solitons in a single channel also degrades the performance since two solitons, when in-phase, experience an attracting force and tend to collide with each other. This effect also gives a contribution to the timing jitter resulting in the system bit error rate (BER) limitation. To avoid the attraction effect, the interval between solitons should be set at least five times as large as the pulse width [12].

Moreover, in wavelength division multiplexing (WDM) systems, solitons at different wavelengths (channels) can also induce a timing jitter. Once pulses in different channels having different speed (due to different carrier frequencies) walk pass through each other, they experience a nonlinear phase shift due to the other pulse's intensity. The process, so called XPM, causes a change in the pulse velocity during the time of collision. In an ideal system with no loss, solitons interact elastically with each other. Their amplitudes and velocities remain the same as those prior to the collision because of the symmetry of the whole collision process. Nevertheless, they experience temporal displacement after the collision by an amount given by the integral of the temporary frequency shift along the distance. The situation becomes much worse within periodically inserted lumped amplifiers because of a breakdown of the symmetry resulting in a residual frequency shift. This again contributes to the timing jitter and reduces the system performance.

Several techniques have been proposed to overcome these limitations, such as the use of bandpass filters [13]. Narrow bandwidth filters inserted periodically are able to stabilise the amplitude and frequency of a soliton. The principle relies on the fact that the soliton amplitude is always proportional to the inverse of its pulse width. Suppose that the amplitude increases (due to the ASE noise, for instance), this would result in a decrease of the pulse width and hence an increase of the spectral width. The increased spectral width is cut off by the filter which brings back the amplitude to its original fixed point. Each filter, however, requires the addition of excess gain to compensate for the loss of energy resulting from the filtering. Therefore the excess gain, at the same time, amplifies linear waves within the filter bandwidth every time the pulse goes through a filter. This leads to a significant growth of noise and may eventually destroy the pulse.

The growth of linear wave can be avoided by using sliding filters [14] whereby the central frequency of the filter is gradually shifted. In this scheme, the glowing linear wave eventually falls in the dissipative region of the filter and can be eliminated while the soliton central frequency is shifted.

Another attempt to separate the noise from solitons is the use of synchronous modulators [15, 16]. This scheme has demonstrated to great effect a full soliton control and achieved unlimited transmission distance. However, synchronous modulation is not compatible with WDM transmission, since the pulses in different channels propagating with different speeds have to be re-timed separately. This requires a demultiplexing and multiplexing of all channels every time they go through modulators.

Among those attempts to overcome the limitations imposed on soliton-based transmission, a significant breakthrough has been achieved by the introduction of dispersion managed (DM) solitons [17, 18]. A DM soliton is a new stable nonlinear pulse which propagates through programmed dispersion segments. The dispersion management, which was originally introduced to suppress nonlinear effects in linear transmission systems, now supports solitons in the nonlinear propagation. The pulses are supported by both linear dispersion and nonlinearity in the dispersion managed system resulting in a quasi-stationary pulse propagation.

In fact, the motivation to develop dispersion managed systems for soliton propagations is the demand in reducing Gordon-Haus effect. This can be achieved by taking advantage of the fact that the Gordon-Haus timing jitter is decreased by reducing the total amount of GVD. Smith *et al.* [17] numerically showed that DM solitons, whose shape is close to Gaussian, exist in a periodically dispersion managed fibre. A DM soliton has enhanced energy compared with the energy of a classical soliton in a fibre with the same average GVD. The energy enhancement is an important property in soliton transmission since it allows the suppression of Gordon-Haus jitter by reducing the average GVD without facing the degradation of signal to noise ratio (SNR). Indeed, the DM soliton is found to exist even when the average GVD is zero, so that the Gordon-Haus effect is fully suppressed.

Although DM solitons provide a solution in reducing timing jitter, its large magnitude of the pulse width oscillations due to GVD variations is found to produce enhanced interaction between adjacent solitons, thereby limiting the bit rate in each wavelength channel. This problem may be minimised by a proper choice of the dispersion map via the map strength [17]; however, the fragility of DM solitons still remains. This is a consequence of the fact that, though a DM soliton is constructed by a balance between properly averaged GVD and nonlinearity, it does not have the robust nature of an ideal conventional soliton. The intrachannel interaction problem of DM solitons becomes more serious when operating at higher bit-rates, since the pulses tend to overlap more.

An alternative way to avoid the problems encountered by DM solitons in high bit-rate transmission systems is to use densely dispersion managed (DDM) solitons [19, 20] in which the dispersion period is made much shorter than the amplifier span. The pulses therefore are not allowed to spread too much and are expected to encounter less interaction problems. This method, however, requires a new type of optical fibre with periodic change of dispersion. To date, the solution may not be practical from an engineering standpoint.

Other advanced soliton controls have been proposed, such as the use of nonlinear loop mirrors (NOLMs) [21]. The use of in-line NOLMs is an effective technique for all-optical passive 2R (reshape and retransmit) regeneration. Again, the implementation of advanced soliton control will result in an increase in the system overall costs.

An alternative is to turn back to the linear side. A quasi-linear mode [22, 23] has recently become more popular. By using a large map strength, the pulses are allowed to spread and overlap with adjacent pulses, but the peak intensity is considerably reduced to avoid nonlinear interactions. In this case, the transmission distance is only limited by the noise. For long-haul transmissions, forward error correction (FEC) techniques are often used. The technique consists of embedding some header information for error correction purpose.

During the development of optical amplifiers, EDFA has been brought to its limit as the demand for bandwidth grows recklessly. At present, WDM transmission systems are using up the entire gain band of EDFA.

EDFAs used in WDM transmission systems are called lumped amplifiers, in which the gain is provided only at the amplifier positions in the transmission line. The discontinuity of the gain also perturbs pulse stability. In contrast, distributed amplifiers retain the optical signal power level over a distance. Therefore they obviously present a better noise performance than the conventional lumped amplifiers [24].

Distributed amplification can be realised by exploiting the stimulated Raman scattering (SRS) effect mentioned previously. A fraction of energy of an incident wave is transfered into an emitted field (Stokes field) whose frequency is red-shifted with respect to the frequency of the incident beam. The stimulated process can be used to transfer energy from a co-(or counter) propagating pump to a signal at a lower frequency resulting in an amplification of the latter. As the gain of Raman amplifiers is relatively low, the signal is gradually amplified while propagating down the fibre. Therefore Raman amplifiers are distributed by nature.

In fact, the idea of Raman amplification was introduced some time ago. Unfortunately the lack of appropriate power sources has delayed the development of Raman amplifier technology for more than 10 years. However, several high-power diode pump sources have become commercially available recently. Coincidentally with the limit of EDFA, Raman techniques have drawn a considerable attention as a new hope to find a breakthrough for solving the present problems for higher transmission speeds.

Most part of this thesis thus focuses on the application of Raman techniques to enhance the performance of high speed optical communication systems. The scope covered by this thesis includes the study of Raman effect in optical fibre, the development of Raman devices particularly Raman fibre lasers (RFLs) and the employment of distributed Raman amplification to upgrade the existing terrestrial links based on standard optical fibres.

1.2 Thesis outline

Reflecting the recent trends in fibre optic communication systems, this thesis provides a theoretical investigation on the feasibility of exploiting Raman effects to enhance the performance of optical communication systems. The research began with the development of a discrete power balance model used to describe the power interaction within Raman based devices turning a passive optical fibre into an active gain medium, which is the underlying principle of Raman amplifiers. The model is only concerned with a few important power signal components in frequency domain that play an important role in the devices. Subsequently, the same model was modified to describe the power interaction within the cavity of RFLs, which can be used to pump Raman amplifiers, allowing one to study its characteristics and perform the cavity optimisation. Next, the discrete model was further developed to account for all interactions of power signals in a whole frequency range of interest. The full frequency model can be used to analyse the gain spectrum of Raman amplifiers and thus provides the information of the signal dynamic and noise within an optical transmission system. In conjunction with an optical transmission system simulation by means of solving the nonlinear Schrödinger equation, this technique allows one to numerically investigate characteristics of a transmission system with Raman amplification and to carry out the optimisation for its performance. Summarising the study and results obtained in the research, the thesis presentation is organised as follows:-

In this chapter, a history of optical fibre communication systems is summarised. The problems experienced in the development of the optical communication systems and their solutions are addressed in a chronological order.

Chapter 2 reviews theory and properties of optical fibres used in telecommunication systems. Important fibre characteristics that affect the performance of optical communications such as optical losses, chromatic dispersion and fibre nonlinearity will be discussed.

Chapter 3 deals with a theoretical background on Raman effects. Its historical perspective ranged from a discovery of spontaneous Raman scattering phenomenon by C.V. Raman in 1928 to a stimulated version of scattering typically employed by most Raman devices will be presented. The development of a simple discrete power balance model to describe the power signal transfer within the Raman devices will also be discussed. The potential application of the model in numerically simulating Raman devices including other influential effects such as noise and double Rayleigh scattering (DRS) will be addressed.

Chapter 4–6 present the results from the author's research. In Chapter 4, the principles, designs, analysis and optimisations of various novel types of RFLs will be described. Most analysis and optimisations are carried out by using the developed numerical model. Some experimental results will also be presented for the sake of comparison and validity of the model.

Chapter 5 is devoted to describe the development of a technique, so called generalised Raman gain model, effectively used to simulate transmission systems with Raman amplification. The technique will be used in Chapter 6 to analyse and optimise the 40 Gb/s WDM transmissions with hybrid amplifiers over standard fibre networks.

Finally, the thesis conclusions are given in Chapter 7.

Chapter 2

Optical fibres and optical communication

2.1 Introduction

Since its introduction in the early 1970s, optical fibre has become the global medium for broadband telecommunication networks. Relying on the basic principle of total internal reflection, optical fibre is capable of guiding lightwave signals without any regeneration nor amplification for hundreds of kilometres–much longer than any conventional electrical transmission line. If the signal is amplified periodically, transmission over transoceanic distance is possible.

This chapter is intended to provide an overview of optical fibre characteristics and an understanding of important phenomena related to fibre optics communication.

2.2 Optical fibre characteristics

The most commonly used type of optical fibre consists of a central core surrounded by a cladding layer. The core and cladding each has a constant refractive index that is slightly higher for the core to allow total internal reflection. This type of fibre is called "step index fibre" [1] which is shown schematically in Figure 2.1.

There are two major types of step index fibre, namely multimode and single mode step index fibres. The multimode fibre has a core diameter of around 50 μm

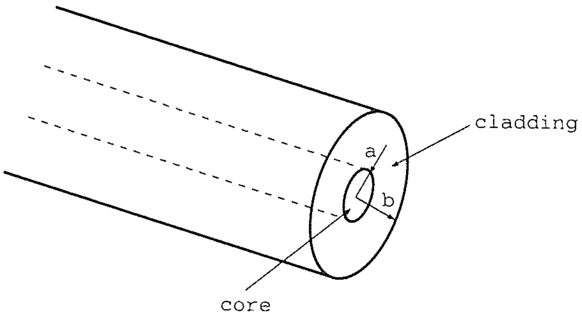

Figure 2.1: Parts of fibre optics cable (not to scale)

or greater, which is large enough to allow propagation of many modes within the fibre core. This effect will cause signal distortion due to intermodal dispersion as discussed in Section 1.1. For high bit rate systems, single mode step index fibre is more suitable since the signal propagating though it does not suffer from the intermodal dispersion. This is possible by making the core small enough to allow the propagation of only one transverse electromagnetic mode (typically HE_{11}). Generally, the core diameter must be in the range of 2 to 10 μm. In this thesis, we shall consider only single mode step index fibre.

To characterise a single mode fibre, two important parameters, namely relative core-cladding index difference (Δ) and normalised frequency (V) are of interest. The relative core-cladding index difference is defined by

$$\Delta = \frac{n_1 - n_2}{n_1}, \tag{2.1}$$

and the normalised frequency is defined by

$$V = \frac{2\pi}{\lambda} a NA. \tag{2.2}$$

The numerical aperture (NA) is given by

$$NA = \sqrt{n_1^2 - n_2^2}, \tag{2.3}$$

where n_1 and n_2 are refractive indices of the core and cladding respectively. a is the core radius and λ is the propagation wavelength. Fundamentally, the number of modes supported by an optical fibre can be determined by normalised frequency V. A step index fibre supports only one mode if $V < 2.405$.

Parameters	SMF-28e	DCF	TL	RTL	TW	LEAF
Attenuation @1550 nm [dB/km]	0.19	0.65	0.21	0.28	0.2	0.2
Dispersion (D) [ps/nm/km]	17	-100	8	-16	6.4	4
Dispersion slope (D_λ) [ps/nm^2/km]	0.086	-0.41	0.058	-0.116	0.04	0.06
Nonlinear refractive index (n_2) [$\times 10^{-20}$ m^2/W]	2.3	2.52	2.7	2.7	2.33	2.7
Effective area @1550 nm (A_{eff}) [μm]	80	19	65	25	50	72

† SMF-28e: Corning SMF-28e® [25]
DCF: Standard dispersion compensating fibre
TL: Alcatel Teralight® [26]
RTL: Alcatel Reverse Teralight® [26]
TW: Lucent Truewave® [27]
LEAF: Corning LEAF® [25]
†† The parameter n_2 for TL, RTL and LEAF fibres are approximate values.

Table 2.1: Characteristics of some commercial fibres.

2.2.1 Optical losses

An important parameter that fundamentally limits transmission distance is a measure of power loss during optical signal propagation inside the fibre. When a signal with power P_{in} is launched into the fibre, the signal will suffer optical loss and decrease exponentially when traversing the fibre. The power level at a point in optical fibre is given by

$$P(z) = P_{in} e^{-\alpha z}, \tag{2.4}$$

where z is the traversed distance at the point of interest and α is the fibre attenuation constant. It is customary to express the attenuation constant in units of dB/km by using the relation

$$\alpha_{dB} = 10\ \alpha \log(e) \simeq 4.343\ \alpha. \tag{2.5}$$

Some attenuation parameters for commercial fibres can be found in Table 2.1.

The attenuation in optical fibre results from the contributions of various effects. Two major contributions are material absorption and Rayleigh scattering. Absorption is a complex phenomenon that is governed by the laws of energy exchange at atomic level. Pure silica absorbs light in the ultraviolet and in the far-infrared region. The absorption in the ultraviolet region is mainly due to electronic and molecular transitions whereas the vibrational transition process is responsible for the absorption in the far-infrared region beyond 2 μm [6].

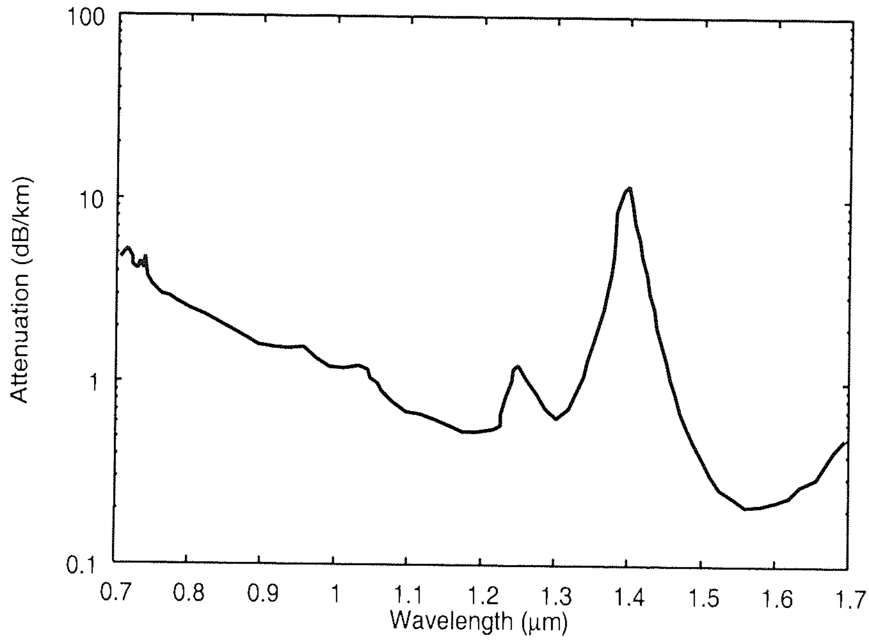

Figure 2.2: Loss profile of a single mode fibre

Nonetheless, the presence of even a small amount of impurities can lead to high peaks of absorption in the infrared region, too. OH-ion from water moisture, with a fundamental vibrational absorption peak at 2.73 μm, is the most significant impurity affecting fibre loss in the infrared region. Moreover, its overtone near 1.37 μm is also responsible for the absorption peak in the transmission wavelength. Such OH absorption peaks hence limit optical transmission to three wavelength windows centred at 0.85, 1.3 and 1.55 μm, respectively. From a practical viewpoint, care must be taken in the fabrication process to minimise the OH-impurity level to achieve a low loss optical fibre.

Rayleigh scattering is another fundamental source of loss arising from random density fluctuations of the fused silica, resulting in random variations in the reflective index of the transmission medium. These local fluctuations scatter light in all directions and hence result in intrinsic fibre loss. The Rayleigh scattering loss is inversely proportional to the light wavelength, and thus it dominates the loss at short wavelengths. Figure 2.2 shows the measured loss profile of a standard single mode telecom fibre. The minimum loss is about 0.2 dB/km at 1.55 μm. Figure 2.3 depicts the attenuation curves for various modern transmission fibres.

Apart from the losses due to material absorption and Rayleigh scattering, there are yet a number of factors that may contribute to the fibre loss. They mainly arise from the engineering process required in the installation of a fibre optic cable, such as bending loss, splicing loss and mode field diameter (MFD) mismatch loss. Advanced technology and careful engineering design are therefore necessary to minimise these losses.

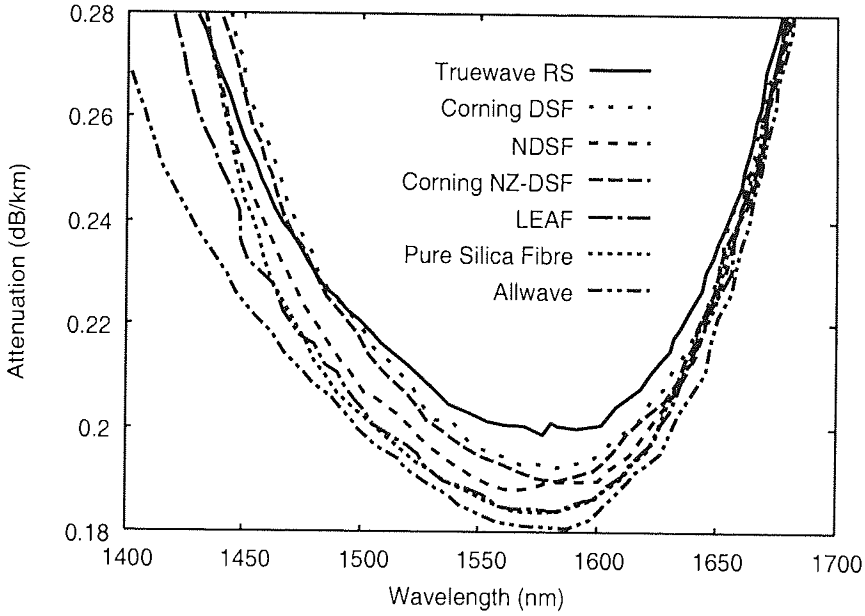

Figure 2.3: Attenuation curves for some modern transmission fibres. (after Ref. [28] ©2003 Springer)

2.2.2 Chromatic dispersion

In a single mode fibre, the intermodal dispersion, which is a result of more than two guided modes propagating simultaneously and arriving at different time, does not exist. However, chromatic dispersion or intramodal dispersion may occur. The effect originates from finite spectral linewidth of optical source. Since optical sources do not generally emit only a single frequency but a band of frequencies, there may be propagation delay differences between the different spectral components of the transmitted signal, resulting in pulse broadening. The delay differences may be caused by the dispersive properties of the material (material dispersion) and guidance effects within the waveguide structure.

The origin of material dispersion can be explained by considering the characteristic resonance frequencies at which the medium absorbs the electromagnetic radiation through oscillations of bound electrons. This gives rise to a dependence of the material refractive index on the frequencies. The refractive index can be well approximated by Sellmeier equation [29]

$$n^2(\omega) = 1 + \sum_{j=1}^{m} \frac{B_j \omega_j^2}{\omega_j^2 - \omega^2}, \tag{2.6}$$

where ω_j is the material resonance frequency and B_j is the strength of the jth resonance. This equation is a good approximation of the refractive index as long as ω is far from the medium resonances. The parameters are to be obtained experimentally. For bulk fused silica, these parameters are found to be $B_1 = 0.6961663, B_2 = 0.4079426, B_3 = 0.8974794, \lambda_1 = 0.0684043\ \mu\text{m}, \lambda_2 = 0.1162414\ \mu\text{m}$, and $\lambda_3 = 9.896161\ \mu\text{m}$ [6].

In the context of signal transmission in optical fibre, the dependence of the refractive index on the spectral components results in the variation of the mode propagation constant k as a function of frequency. To gain a deeper understanding, it is customary to account for the effect of dispersion by expanding the propagation constant $k(\omega)$ in a Taylor series around the centre frequency ω_0:

$$\begin{aligned} k(\omega) &= k\Big|_{\omega=\omega_0} + \frac{\partial k}{\partial \omega}\Big|_{\omega=\omega_0} (\omega - \omega_0) \\ &+ \frac{1}{2}\frac{\partial^2 k}{\partial \omega^2}\Big|_{\omega=\omega_0} (\omega - \omega_0)^2 + \frac{1}{6}\frac{\partial^3 k}{\partial \omega^3}\Big|_{\omega=\omega_0} (\omega - \omega_0)^3 + \cdots , \end{aligned} \tag{2.7}$$

Each Taylor component can be interpreted as follows. The first component is the propagation constant describing the phase velocity of the pulse carrier. The pulse envelope moves at the group velocity expressed by the second term ($v_g = (\partial k/\partial \omega|_{\omega=\omega_0})^{-1}$) while the third term is responsible for pulse broadening. The cubic term is higher order dispersion, which is related to dispersion slope to be discussed later. For simplicity, constant variables k', k'' and k''' are defined to represent the constant coefficients in the second, third and fourth terms respectively. These parameters are also related to the refractive index $n(\omega)$ and its derivatives via the relations

$$\begin{aligned} k' &= \frac{\partial k}{\partial \omega}\bigg|_{\omega=\omega_0} = \frac{1}{c}\left(n + \omega\frac{dn}{d\omega}\right) = \frac{n_g}{c} = \frac{1}{v_g}, && (2.8) \\ k'' &= \frac{\partial^2 k}{\partial \omega^2}\bigg|_{\omega=\omega_0} = \frac{1}{c}\left(2\frac{dn}{d\omega} + \omega\frac{d^2n}{d\omega^2}\right) \simeq \frac{\omega}{c}\frac{d^2n}{d\omega^2} \simeq \frac{\lambda^3}{2\pi c^2}\frac{d^2n}{d\lambda^2}, && (2.9) \end{aligned}$$

where n_g is the group index and c is the speed of light.

In optical fibre engineering, it is common to use the dispersion parameter D in place of k''. The relation between these two parameters is

$$D = \frac{dk'}{d\lambda} = -\frac{2\pi c}{\lambda^2}k''. \qquad (2.10)$$

If $\lambda = 1.55$ μm, a short hand version of the equation becomes

$$k''\Big|_{1.55\ \mu\mathrm{m}} \quad [\mathrm{ps}^2/\mathrm{km}] = -1.275D\Big|_{1.55\ \mu\mathrm{m}} \quad [\mathrm{ps/nm/km}]. \qquad (2.11)$$

An interesting feature of chromatic dispersion is that D vanishes at a wavelength of about 1.27 μm [1] and becomes positive for longer wavelengths. The wavelength at which $D = 0$ is referred to as the zero-dispersion wavelength λ_D that divides the dispersion into two regions. The shorter wavelength side, where D is negative (or k'' is positive), is referred to as the *normal* dispersion region whereas the longer wavelength side is recognised as the *anomalous* dispersion region. In the normal-dispersion regime, the lower frequency (red-shifted) components of an optical pulse travel faster than the higher frequency (blue-shifted) components. The opposite occurs in the anomalous-dispersion regime [6].

The zero-dispersion wavelength discussed earlier has been measured from a bulk fused silica. The actual dispersion of optical fibre generally deviates from the above value due to a contribution of dielectric waveguiding effect. The total dispersion must therefore be a combination of the material dispersion and the waveguide dispersion. Typically, single mode fibres exhibit total $\lambda_D \simeq 1.31$ μm. Note that the waveguide dispersion depends on fibre design characteristics such as the refractive index profile and the physical core-cladding structure. This feature can be used to shift the zero-dispersion wavelength λ_D to the vicinity of 1.55 μm where the fibre loss is minimum. This type of fibre is referred to as dispersion-shifted fibre (DSF), and finds a great potential in high speed optical communication systems. Figure 2.4 illustrates the dispersion parameter curves versus wavelengths for some commercial fibres.

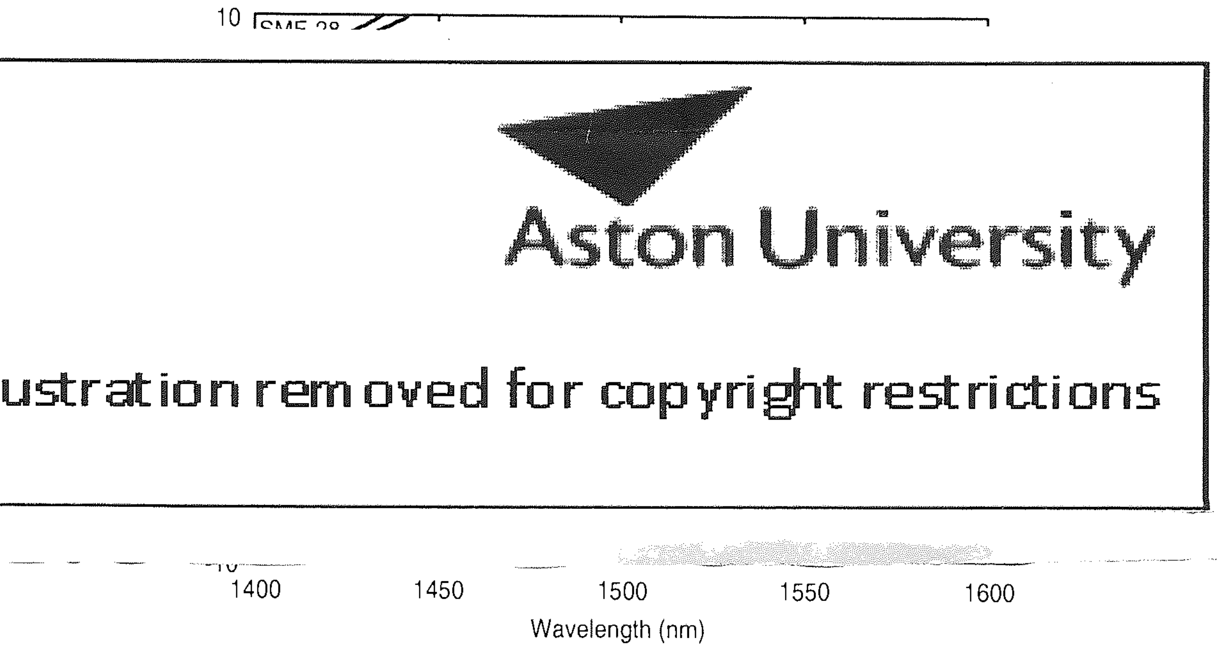

Aston University
Illustration removed for copyright restrictions

Figure 2.4: Dispersion parameter D versus wavelength for serveral commercial fibre types. (after Ref. [28] ©2003 Springer)

Other types of special dispersion profile, such as dispersion flattened fibres, can also be realised by properly designing the core-cladding structure. The dispersion parameters for various types of modern telecommunication fibres are summarised in Table 2.1.

2.2.3 Fibre nonlinearities

In the early stages of optical communication, signals were launched into the fibre with a relatively low power. The optical fibre was recognised at that time as a linear device. However, as the bit rate increased, a higher launch power was required to ensure that enough photons per bit were received at the receiver to achieve a good bit error rate (BER). In other words, the signal power must be high enough to avoid being buried by noise. As the power increases, the nonlinear effects in optical fibres become more significant and make an impact on the quality of optical communication systems. This section will discuss the major nonlinear effects in optical fibres and their properties.

Nonlinear effects in fused silica optical fibres have been classified into two main categories. The first one is nonlinear refractive index arising from nonlinear electric polarisation of bound electrons in silica. The intense light interacts with the dielectric medium, whose response results in the change of the refractive index with the light intensity.

The second category is stimulated inelastic scattering, in which the optical field transfers parts of its energy to the nonlinear medium in the form of vibrational excitation modes of silica. Two important effects in optical fibres fall into this category, namely stimulated Raman scattering (SRS) and stimulated Brillouin (SBS) scattering. SRS transfers energy from the incident field into optical phonons and thus creates photons at the down-shifted Stokes frequency, where in contrast, SBS transfers the energy to the Stoke waves via acoustic phonons. A detailed discussion of SRS will be given in Chapter 3.

As for the nonlinear refractive index, the origin of the nonlinear response can be understood by considering the influence of incident light over the medium properties. The induced polarisation $\boldsymbol{P}$ from the electric dipoles in the electric field $\boldsymbol{E}$ is

$$\begin{aligned} \boldsymbol{P} &= \int_{-\infty}^{t} \epsilon_0 \chi^{(1)}(\boldsymbol{r}, t-\tau_1) \cdot \boldsymbol{E}(\boldsymbol{r}, \tau_1) d\tau_1 \\ &+ \iint_{-\infty}^{t} \epsilon_0 \chi^{(2)}(\boldsymbol{r}, t-\tau_1, t-\tau_2) : \boldsymbol{E}(\boldsymbol{r}, \tau_1)\boldsymbol{E}(\boldsymbol{r}, \tau_2) d\tau_1 d\tau_2 \qquad (2.12) \\ &+ \iiint_{-\infty}^{t} \epsilon_0 \chi^{(3)}(\boldsymbol{r}, t-\tau_1, t-\tau_2, t-\tau_3) \vdots \boldsymbol{E}(\boldsymbol{r}, \tau_1)\boldsymbol{E}(\boldsymbol{r}, \tau_2)\boldsymbol{E}(\boldsymbol{r}, \tau_3) d\tau_1 d\tau_2 d\tau_3, \end{aligned}$$

where $\chi^{(1)}$, $\chi^{(2)}$ and $\chi^{(3)}$ represent the linear, second and third order nonlinear susceptibility tensors, having the dependence on the spatial coordinates $\boldsymbol{r}$ of the material, and

$$\begin{aligned}\left(\chi^{(1)}\cdot\boldsymbol{E}\right)_i &= \sum_j \chi^{(1)}_{ij}E_j\\ \left(\chi^{(2)}:\boldsymbol{EE}\right)_i &= \sum_{j,k}\chi^{(2)}_{ijk}E_jE_k\\ \left(\chi^{(3)}\vdots\boldsymbol{EEE}\right)_i &= \sum_{j,k,l}\chi^{(3)}_{ijkl}E_jE_kE_l,\end{aligned} \tag{2.13}$$

where i, j, k and l are the axis of polarisation (x, y, z). However, in silica glass optical fibre, the second order nonlinear effect $(\chi^{(2)})$ disappears due to the centrosymmetric crystal structure of silica.

In the common analysis of light propagating through optical fibres used in optical communication, the nonlinear effects that have drawn the most attention originate from the third order susceptibility $(\chi^{(3)})$, which is responsible for various important phenomena, namely nonlinear refraction, third harmonic generation and four-wave mixing. However, the latter two phenomena require phase matching conditions that are hardly satisfied under normal circumstances. Most of the nonlinear effects in optical fibres, therefore, originate from nonlinear refraction so that the medium refractive index becomes intensity dependent as a result from the contribution of $\chi^{(3)}$. Thus

$$\widetilde{n}(\omega, |E|^2) = n(\omega) + n_2 I, \tag{2.14}$$

where $n(\omega)$ is the linear part as given in Eq. (2.6), I is the light intensity and n_2 is nonlinear index coefficient defined as,

$$n_2 = \frac{3}{8n}\mathrm{Re}(\chi^{(3)}_{xxxx}), \tag{2.15}$$

where $\mathrm{Re}(\cdot)$ is the real part of a complex value. The field is assumed to be linearly polarised so that only $\chi^{(3)}_{xxxx}$ contributes to the refractive index. This nonlinearity is referred to as *Kerr* nonlinearity.

2.3 Wave propagation in optical fibres

To analyse the impact of those effects discussed previously on the performance of optical communication systems, one needs to understand how a lightwave signal propagates in optical fibre. In this section, we derive the nonlinear Schrödinger equation that governs the dynamics of signal propagation in the optical fibre.

We shall formally begin the formulation with the well known Maxwell's equations [30],

$$\nabla \times \boldsymbol{E} = -\mu \frac{\partial \boldsymbol{H}}{\partial t} \tag{2.16}$$

$$\nabla \times \boldsymbol{B} = \epsilon \frac{\partial \boldsymbol{E}}{\partial t} \tag{2.17}$$

$$\nabla \cdot \boldsymbol{D} = 0 \tag{2.18}$$

$$\nabla \cdot \boldsymbol{B} = 0 \tag{2.19}$$

where $\boldsymbol{D} = \epsilon \boldsymbol{E}$ and $\boldsymbol{B} = \mu \boldsymbol{H}$, and $\boldsymbol{D}, \boldsymbol{E}, \boldsymbol{B}$ and $\boldsymbol{H}$ represent electric flux density, electric field intensity, magnetic flux density and magnetic field intensity, respectively. To establish a wave equation, we apply a curl operator at both sides of Eq. (2.16) and substitute Eq. (2.17) into the result. Thus

$$\nabla \times \nabla \times \boldsymbol{E} = -\mu \frac{\partial}{\partial t}(\nabla \times \boldsymbol{H}) = -\mu\epsilon \frac{\partial^2 \boldsymbol{E}}{\partial t^2}. \tag{2.20}$$

From a vector identity $\nabla \times \nabla \times \boldsymbol{A} = \nabla(\nabla \cdot \boldsymbol{A}) - \nabla^2 \boldsymbol{A}$, Eq. (2.20) yields,

$$\nabla(\nabla \cdot \boldsymbol{E}) - \nabla^2 \boldsymbol{E} = -\mu\epsilon \frac{\partial^2 \boldsymbol{E}}{\partial t^2} \tag{2.21}$$

Since the medium is purely dielectric and thus no charge particles exist, Eq. (2.18) holds. The magnetic properties of silica can also be ignored, the permeability is thus given by the free space permeability μ_0. As a result, Eq. (2.21) yields

$$\nabla^2 \boldsymbol{E}(\boldsymbol{r}, t) - \mu_0 \epsilon \frac{\partial^2}{\partial t^2} \boldsymbol{E}(\boldsymbol{r}, t) = 0, \tag{2.22}$$

Because the permittivity ϵ is a function of frequency ω as a result of chromatic dispersion, it is simpler to work in Fourier domain, thus

$$\nabla^2 \widetilde{\boldsymbol{E}}(\boldsymbol{r}, \omega) + \omega^2 \mu_0 \epsilon \widetilde{\boldsymbol{E}}(\boldsymbol{r}, \omega) = 0, \tag{2.23}$$

where $\widetilde{\boldsymbol{E}}(\boldsymbol{r}, \omega)$ is the Fourier transform of $\boldsymbol{E}(\boldsymbol{r}, t)$ defined by

$$\widetilde{\boldsymbol{E}}(\boldsymbol{r}, \omega) = \int_{-\infty}^{\infty} \boldsymbol{E}(\boldsymbol{r}, t) \exp(i\omega t) dt. \tag{2.24}$$

It is convenient to define the propagation constant $k^2 = (n\omega/c)^2 = \omega^2\mu_0\epsilon$. Eq. (2.23) then becomes

$$\nabla^2\widetilde{\boldsymbol{E}}(\boldsymbol{r},\omega) + k^2\widetilde{\boldsymbol{E}}(\boldsymbol{r},\omega) = 0. \tag{2.25}$$

The above equation may be solved under a proper set of boundary conditions for a full description of the wave solutions in the optical fibre. This section, however, is intended to focus only on the propagation of wave packets that carry information. Therefore, we shall neglect all transverse components and then assume that there is no variation of the field in other directions apart from the propagation direction. In the Cartesian coordinate system, the assumption leads to yield $\partial/\partial x = 0$ and $\partial/\partial y = 0$ when the light is propagating along the z-axis. Eq. (2.25) can then be reduced to a scalar form

$$\frac{\partial^2}{\partial z^2}\widetilde{E}_z(z,\omega) + k^2\widetilde{E}_z(z,\omega) = 0. \tag{2.26}$$

To solve Eq. (2.26), an essential step is to apply the quasi monochromatic approximation, which assumes that the waveform has a slowly varying envelope, or has a narrow spectrum with respect to its carrier frequency. This assumption is valid for consideration of a pulse whose width is much wider than the carrier time period. In general, this assumption is approximately valid for pulse widths > 1 ps. Using the monochromatic approximation, we can simply assume a solution for the above equation such that

$$E_z(z,t) = Q(z,t)\exp(ik_0z - i\omega_0t), \tag{2.27}$$

where $Q(z,t)$ is the slowly varying wave envelope, k_0 and ω_0 are the propagation constant and the angular frequency of the carrier, respectively.

We apply the Fourier transform to the assumed solution and obtain

$$\widetilde{E}_z(z,\omega) = \widetilde{Q}(z,\omega - \omega_0)\exp(ik_0z). \tag{2.28}$$

When we substitute Eq. (2.28) into Eq. (2.26), we can eliminate the second order partial derivative term $(\partial^2\widetilde{Q}/\partial z^2)$ due to the slowly varying nature of the wave envelope. We also approximate the factor $k^2 - k_0^2 \simeq 2k_0(k - k_0)$. Thus we obtain

$$i\frac{\partial\widetilde{Q}}{\partial z} + (k - k_0)\widetilde{Q} = 0. \tag{2.29}$$

If one solves Eq. (2.25) applying the quasi monochromatic approximation for the full description of light propagating in the fibre including the transverse components (that we have so far omitted), the electric field should take the general form as

$$E_z(x,y,z;t) = F(x,y)Q(z,t)\exp(ik_0z - i\omega_0t), \tag{2.30}$$

where $F(x,y)$ is the mode field distribution in the fibre cross section. The Eq. (2.14) can be rewritten as

$$\widetilde{n}(\omega,|Q|^2) = n_0 + \frac{|Q|^2}{A_{eff}}n_2, \tag{2.31}$$

where n_0 is the refractive index of the medium at carrier frequency. A_{eff} is the effective area given by [31]

$$A_{eff} = \frac{\left(\iint_{-\infty}^{\infty}|F(x,y)|^2dxdy\right)^2}{\iint_{-\infty}^{\infty}|F(x,y)|^4dxdy}. \tag{2.32}$$

Recalling the relation $k = n\omega/c$, we now redefine k as

$$k = k(\omega,|Q|^2) = \frac{n_0\omega}{c} + \frac{n_2\omega}{c}\frac{|Q|^2}{A_{eff}}. \tag{2.33}$$

In a similar way to Eq. (2.7), we employ the Taylor expansion on the propagation constant k around ω_0 and $|Q|^2 = 0$

$$\begin{aligned} k(\omega,|Q|^2) &= k\Big|_{\omega=\omega_0,|Q|^2=0} + \frac{\partial k}{\partial\omega}\Big|_{\omega=\omega_0,|Q|^2=0}(\omega-\omega_0) + \frac{\partial k}{\partial|Q|^2}\Big|_{\omega=\omega_0,|Q|^2=0}|Q|^2 \\ &+\frac{1}{2}\frac{\partial^2k}{\partial\omega^2}\Big|_{\omega=\omega_0,|Q|^2=0}(\omega-\omega_0)^2 + \frac{1}{2}\frac{\partial^2k}{\partial\left[|Q|^2\right]^2}\Big|_{\omega-\omega_0,|Q|^2=0}\left[|Q|^2\right]^2 \\ &+\frac{1}{6}\frac{\partial^3k}{\partial\omega^3}\Big|_{\omega=\omega_0,|Q|^2=0}(\omega-\omega_0)^3 + \frac{1}{6}\frac{\partial^3k}{\partial\left[|Q|^2\right]^3}\Big|_{\omega-\omega_0,|Q|^2=0}\left[|Q|^2\right]^3 + \cdots, \end{aligned} \tag{2.34}$$

Substituting Eq. (2.33) into Eq. (2.34), we find that

$$k - k_0 = k'(\omega-\omega_0) + \frac{1}{2}k''(\omega-\omega_0)^2 + \frac{1}{6}k'''(\omega-\omega_0)^3 + \frac{n_2\omega_0}{cA_{eff}}|Q|^2, \tag{2.35}$$

neglecting all higher order nonlinear terms. We subsequently substitute Eq. (2.35) into Eq. (2.29) and see that

$$i\frac{\partial\widetilde{Q}}{\partial z} + \left\{k'(\omega-\omega_0) + \frac{1}{2}k''(\omega-\omega_0)^2 + \frac{1}{6}k'''(\omega-\omega_0)^3 + \frac{n_2\omega_0}{cA_{eff}}|Q|^2 + \right\}\widetilde{Q} = 0. \tag{2.36}$$

The last step is to perform an inverse Fourier transform to obtain the wave envelope in time domain. From Eq. (2.28), we can define the inverse transform of the wave envelope as

$$\begin{aligned} Q(z,t) &= \int_{-\infty}^{\infty} \widetilde{E}(z,\omega)e^{-i(\omega-\omega_0)t} \cdot e^{-ik_0 t} d(\omega-\omega_0) \\ &= \int_{-\infty}^{\infty} \widetilde{Q}(z,\omega-\omega_0)e^{-i(\omega-\omega_0)t} d(\omega-\omega_0), \end{aligned} \tag{2.37}$$

which leads to the transform operator $(\omega-\omega_0) \Longleftrightarrow i\partial/\partial t$. Hence in the time domain, Eq. (2.36) becomes

$$i\left\{\frac{\partial Q}{\partial z} + k_0'\frac{\partial Q}{\partial t}\right\} - \frac{k_0''}{2}\frac{\partial^2 Q}{\partial t^2} - \frac{ik_0'''}{6}\frac{\partial^3 Q}{\partial t^3} + \frac{\omega_0}{c}\frac{n_2}{A_{eff}}|Q|^2 Q = 0. \tag{2.38}$$

For the sake of convenience, we employ a frame of reference moving with the wave envelope at the group velocity $v_g = 1/k_0'$ by making the transformation $\tau = t - k_0' z$, thus

$$i\frac{\partial Q}{\partial z} - \frac{k_0''}{2}\frac{\partial^2 Q}{\partial \tau^2} - \frac{ik_0'''}{6}\frac{\partial^3 Q}{\partial \tau^3} + \frac{2\pi}{\lambda_0}\frac{n_2}{A_{eff}}|Q|^2 Q = 0. \tag{2.39}$$

where λ_0 is the wavelength of the carrier.

So far, we have considered the case in which the fibre loss has been omitted. In the lossy case, the fibre attenuation can be included as

$$i\frac{\partial Q}{\partial z} - \frac{k_0''}{2}\frac{\partial^2 Q}{\partial \tau^2} - \frac{ik_0'''}{6}\frac{\partial^3 Q}{\partial \tau^3} + \frac{2\pi}{\lambda_0}\frac{n_2}{A_{eff}}|Q|^2 Q = -\frac{i\alpha}{2}Q, \tag{2.40}$$

where α represents the linear attenuation coefficient. Finally we arrive at the NLS equation accordingly. Note nonetheless that, in order to numerically solve this NLS equation, one may consider to normalise it to maintain a high computational accuracy. The detailed discussion regarding the normalisation will be given in Chapter 5.

2.4 Impact of important effects in optical communication

In optical communication, a number of effects arising from fibre loss, dispersion and nonlinearity simultaneously limit the capacity of the system. Fibre loss may be overcome easily in some systems by using amplification techniques. However, the other two are rather complicate to deal with. In this section, we review some important effects that are of concern in limiting the performance of optical communication systems.

2.4.1 Group velocity dispersion

As discussed in Section 2.2.2, the parameter k'' is responsible for pulse broadening and is referred to as group velocity dispersion (GVD). This phenomenon results from the frequency dependence of the propagation constant k, or in other words, the material refractive index and waveguide structure of the optical fibre. The effect is to cause different spectral components to propagate at different velocities resulting in a linear chirp in the carrier across the pulse and eventually inducing pulse broadening. For an arbitrary pulse envelope $f(t)$, a linearly chirped pulse is defined as

$$Q(z,t) = f(t)\exp(-\frac{iC}{2}\frac{t^2}{t_0^2}), \tag{2.41}$$

where C is the chirp parameter and t_0 is the pulse width. By considering Eq. (2.41), one may notice that the instantaneous frequency increases linearly from the leading to the trailing edge of the pulse for a positive C. This effect is referred to as the "positive chirp or up-chirp". Negative chirp or down-chirp is simply the opposite situation when C is negative. During the propagation GVD also introduces a linear chirping to the pulse. A positive chirp is introduced when propagating in an anomalous dispersion regime and vice versa for a normal regime.

As the GVD arises from different frequency components travelling at different velocities, a shorter pulse (wider spectrum) will experience GVD more seriously. It is convenient to introduce the dispersion length L_D, which provides a length scale over which the GVD becomes important. Dispersion length L_D is proportional to the square of pulse width and the inverse of the absolute value of k'', and is defined as

$$L_D = \frac{t_0^2}{|k''|}, \tag{2.42}$$

where t_0 is the pulse width, which is related to its full-width at half-maximum

(FWHM) pulse width as follows:

$$t_{FWHM} = 2\sqrt{\ln 2}\, t_0 \simeq 1.665\, t_0 \quad \text{for Gaussian pulse} \tag{2.43}$$

$$t_{FWHM} = 2\ln(1+\sqrt{2})\, t_0 \simeq 1.763\, t_0 \quad \text{for hyperbolic sech pulse} \tag{2.44}$$

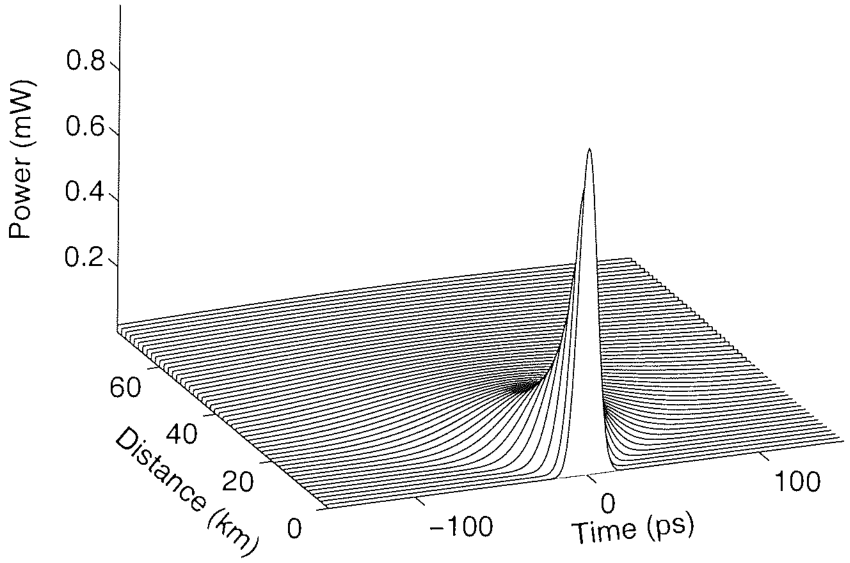

Figure 2.5: Pulse broadening due to GVD in the absence of loss and nonlinearity. The launched pulse has Gaussian shape with an initial pulse width of 12.5 ps and the peak power of 1 mW

Under the condition that the propagation distance is comparable or longer than the dispersion length L_D, GVD will play an important role in the propagation, resulting in severe pulse broadening. Figure 2.5 illustrates the propagation of a single Gaussian pulse launched in an ideal optical fibre whose k'' is similar to that of standard SMF. The pulse appears to disperse completely only after 20 km as the dispersion length L_D is only 2.6 km for this pulse width. Had we used a wider pulse, for instance, a pulse width of 25 ps, the propagation would have suffered much less dispersion as the degree of dispersion effect varies with the square of the pulse width.

In the case of a pulse having Gaussian form, it is rather simple to derive a general formula describing the pulse width variation throughout the propagation. Neglecting the nonlinear, higher order dispersion and attenuation terms in Eq. (2.40), we thus have

$$i\frac{\partial Q}{\partial z} - \frac{k_0''}{2}\frac{\partial^2 Q}{\partial \tau^2} = 0. \tag{2.45}$$

This equation can be readily solved by using the Fourier method. If $\widetilde{Q}(z,\omega)$ is the Fourier transform of $Q(z,\tau)$, definition of which is defined in Eq. (2.24), Eq. (2.45) can be transformed into the Fourier domain as

$$i\frac{\partial \widetilde{Q}}{\partial z} + \frac{k_0''}{2}\omega^2\widetilde{Q} = 0, \tag{2.46}$$

whose solution is given by

$$\widetilde{Q}(z,\omega) = \widetilde{Q}(0,\omega)\exp\left(i\frac{k_0''}{2}\omega^2 z\right). \tag{2.47}$$

For a Gaussian pulse with the initial pulse width τ_0 and the initial chirp C_0

$$Q(0,\tau) = \exp\left(-\frac{1}{2}(1+iC_0)\frac{\tau^2}{\tau_0^2}\right), \tag{2.48}$$

its Fourier transform takes the form

$$\widetilde{Q}(0,\omega) = \left(\frac{2\pi\tau_0}{\sqrt{1+iC_0}}\right)^{\frac{1}{2}} \exp\left[-\frac{1}{2}\omega^2\left(\frac{\tau_0^2}{1+iC_0} - ik_0''z\right)\right]. \tag{2.49}$$

By substituting Eq. (2.49) into Eq. (2.47) and carrying out the integration and the inverse Fourier transform, the amplitude at any point z along the fibre is given by

$$Q(z,\tau) = \left(\frac{\tau_0}{\tau_0^2 - ik_0''z + k_0''C_0 z}\right)^{\frac{1}{2}} \exp\left[-\frac{1}{2}\frac{\tau^2(1+iC_0)}{\tau_0^2 - ik_0''(1+iC_0)z}\right]. \tag{2.50}$$

One may notice from Eq. (2.50) that a Gaussian pulse maintains its shape on propagation but its width may vary and become

$$\tau_1 = \tau_0\left[1 + \frac{z^2}{L_D^2}(1+C_0^2) + 2\ \mathrm{sgn}(k_0'')\frac{z}{L_D}C_0\right]^{\frac{1}{2}}. \tag{2.51}$$

Similarly, one may work out the general formula for the chirp parameter variation of the propagating pulse, and find that

$$C_1 = C_0 + \mathrm{sgn}(k_0'')(1+C_0)\frac{z}{L_D}. \tag{2.52}$$

The above equation shows that the chirp parameter varies linearly in the case that only dispersion is present.

For an initially unchirped Gaussian pulse, Eq. (2.51) takes a simple form as [6]

$$\tau_1 = \tau_0 \sqrt{1 + \left(\frac{z}{L_D}\right)^2}. \tag{2.53}$$

GVD is a linear effect and can be compensated for by using a straightforward strategy. As previously mentioned in Section 2.2.2, one may design an optical fibre with a shifted dispersion curve or even an inverse dispersion sign at a particular range of wavelengths. An optical fibre which has been specifically designed to compensate for the accumulated dispersion is referred to as dispersion compensating fibre (DCF). We may use the DCF to compensate for the accumulated dispersion induced by GVD during the propagation through the transmission fibre. By periodically compensating for accumulated GVD with carefully located DCF, the pulse can be restored completely to its original shape. This technique is widely known as "dispersion management". Figure 2.6 shows the propagation of a single Gaussian pulse in a lossless dispersion managed system. The initial pulse width is again 12.5 ps with 1 mW peak power. The accumulated dispersion is compensated for every 100 km of transmission fibre using DCFs. The linear chirp parameter of this pulse is shown in Figure 2.7, where one may see that the pulse returns to chirp-free (so called transform limited state) after the dispersion has been compensated for by DCFs. Note that the pulse broadening behaviour also depends on the initial chirp of the launched pulse. For example, if a pulse with negative chirp is launched into an optical fibre under an anomalous dispersion regime, the pulse will experience compression at the beginning until the residual chirp has been fully compensated for and become a chirp free pulse. Then the broadening will continue as usual.

2.4.2 Higher order dispersion

Our discussions on dispersion induced pulse broadening in Section 2.4.1 are restricted to the effect of k'' only. Under some particular circumstances at which the higher order dispersion terms, such as k''', play an important role, one may need to understand what effect the inclusion of these higher order terms will have on the pulse propagation. This section is devoted to discuss such issue.

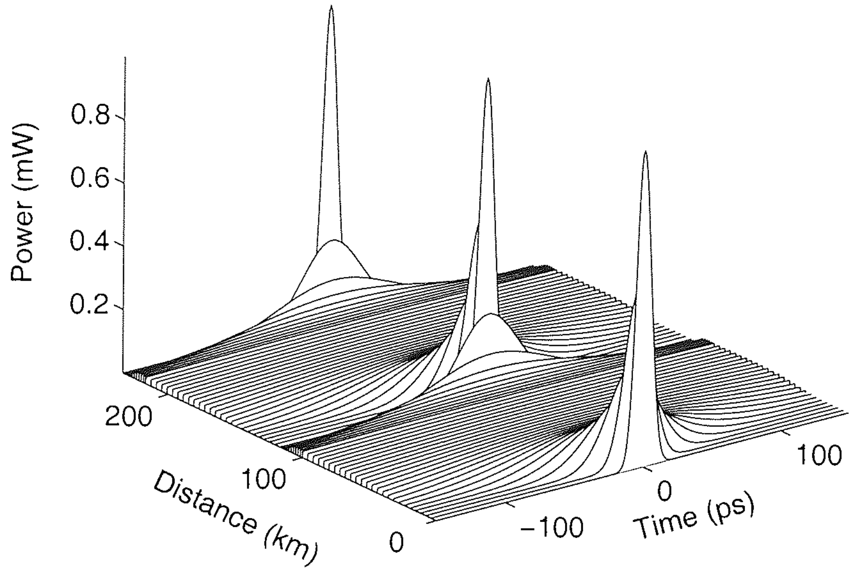

Figure 2.6: Single pulse propagation in a lossless dispersion managed line.

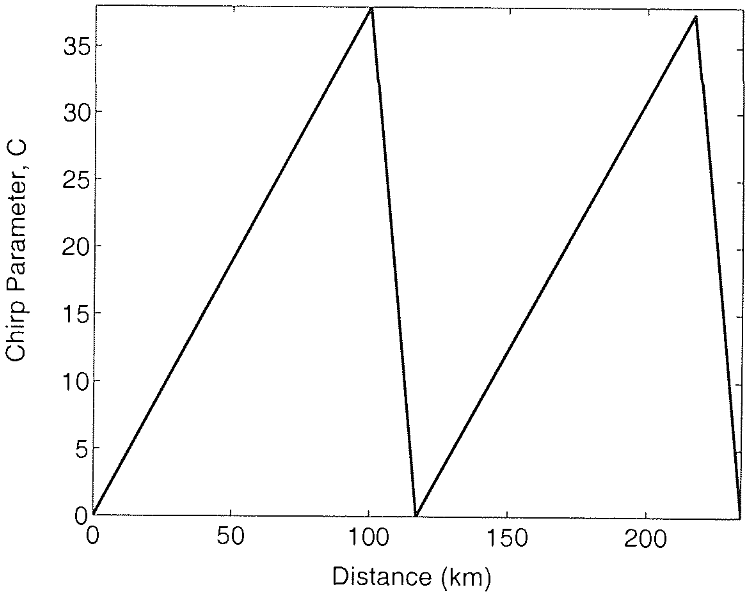

Figure 2.7: Variation of chirp parameter with propagated distance for a Gaussian pulse under a dispersion management.

In general, there are two circumstances in which k''' plays a crucial role in pulse propagation. The first one is when the pulse wavelength nearly coincides with the zero-dispersion wavelength λ_D where $k'' \simeq 0$. In this case, the k''' term is dominant and has to be taken into account. The second circumstance is when ultrashort pulses with pulse width $t_0 < 0.1$ ps are considered [6]. It is then necessary to include the k''' term, since the frequency difference between the pulse spectral width and carrier frequency is not small enough to justify the truncation of Taylor expansion in Eq. (2.7). Understanding this fact, it is convenient to define a dispersion length associated with the higher order dispersion term as

$$L'_D = \frac{t_0^3}{|k'''|}. \tag{2.54}$$

The higher order dispersion plays an important role if $L'_D \lesssim L_D$. Figure 2.8 depicts the pulse shapes at $z = 4\ L'_D$ of an initially unchirped Gaussian pulse (solid curve) propagated in an artificial optical fibre in the absence of loss, nonlinearity and k''.

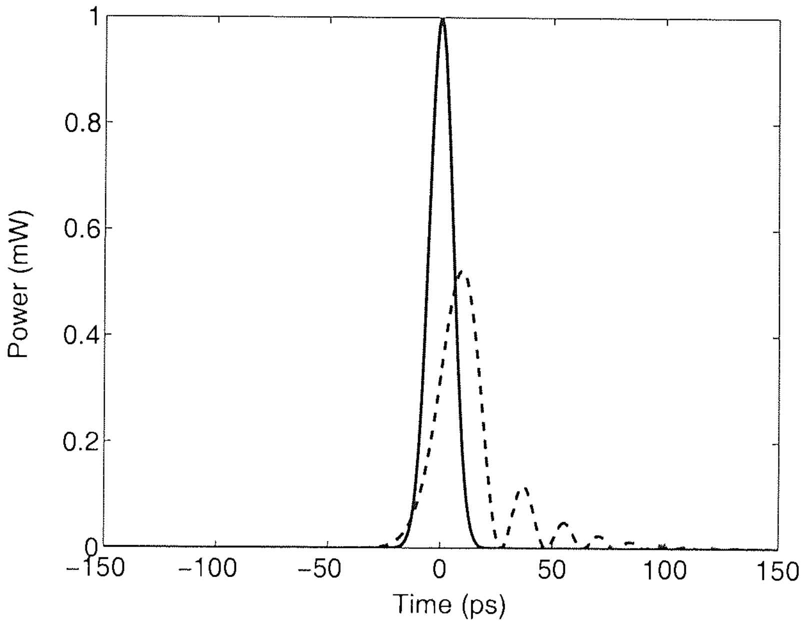

Figure 2.8: Effect of the third order dispersion on a Gaussian pulse with an initial pulse width of 12.5 ps propagated in a fibre in the absence of loss, nonlinearity and k''. The solid curve represents the initial pulse at $z = 0$ km and the dashed curve represents the pulse at $z = 4\ L'_D \simeq 22,000$ km

One may see that the effect of higher order dispersion is to distort the pulse shape such that it becomes asymmetric with an oscillatory structure near one of its edges. The oscillation appears near the trailing edge of the pulse for the case of positive k''', and the opposite occurs when k''' is negative. The higher order dispersion may be compensated for by using a carefully designed DCF, which compensates not only for the effects of k'', but also for the effects of k'''. Note that k''' is often referred to in the context of optical communication and in fibre specifications as the dispersion slope D_λ which is related to k''' by

$$k''' = \frac{(D_\lambda \lambda_0 + 2D)\,\lambda_0^3}{(2\pi c)^2}, \tag{2.55}$$

where D is dispersion parameter and λ_0 is the carrier wavelength.

2.4.3 Self phase modulation and cross phase modulation

As discussed in Section 2.2.3, the nonlinear refractive index arising from $\chi^{(3)}$ nonlinearity is responsible for self phase modulation (SPM) and cross phase modulation (XPM). The former can be described as the effect of which a light propagating down the fibre experiences when the refractive index becomes a function of the light intensity. The SPM gives rise to an intensity dependent phase shift inducing a distortion in the pulse spectrum, while the temporal pulse shape remains undistorted as long as the GVD does not play a role. As in the previous section, it is useful to introduce a nonlinear length L_{NL} over which the nonlinear effects become important for pulse evolution along a fibre of length L. Thus the nonlinear length L_{NL} is defined as

$$L_{NL} = \left(\frac{2\pi}{\lambda_0}\frac{n_2}{A_{eff}}P_0\right)^{-1}, \tag{2.56}$$

where n_2, A_{eff} and P_0 are the nonlinear index coefficient, effective area and pulse peak power, respectively. In optical communication, nonlinearity plays an important role only if $L \gtrsim L_{NL} \lesssim L_D$. Figure 2.9 shows the optical spectra of a Gaussian pulse at $z = 0, z = 10\ L_{NL}$ and $z = 20\ L_{NL}$ in a presence of nonlinearity only. The spectra are clearly distorted and some new frequency components are generated as the propagation distance increases.

As mentioned previously, SPM only introduces a distortion in the pulse spectrum, whereas the pulse shape remains undistorted. However, this is not the case when GVD becomes important, because the SPM induces a nonlinear chirp across the pulse that GVD will translate into a pulse broadening or compression. In the anomalous dispersion regime, the interplay between SPM and GVD will support a

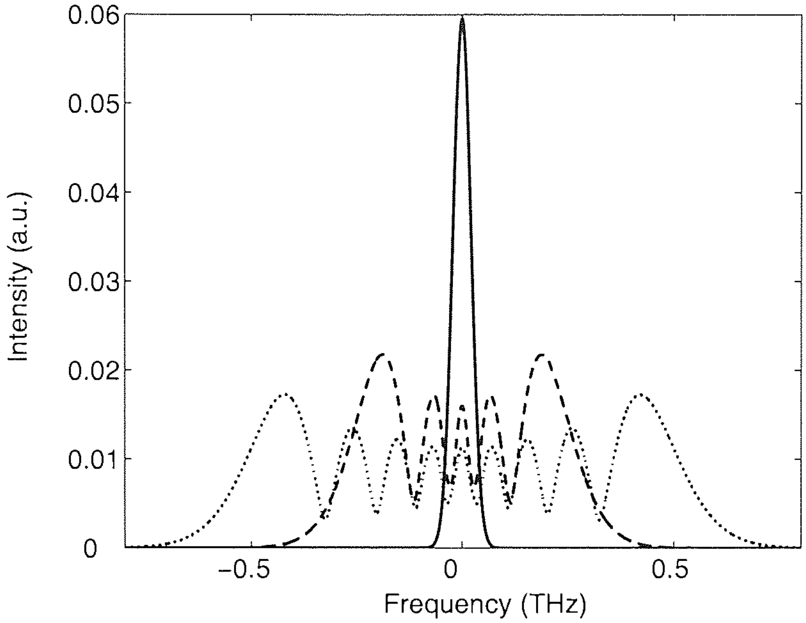

Figure 2.9: Optical spectra of a Gaussian pulse with an initial pulse width of 12.5 ps propagated in a fibre in a presence of SPM only. Solid, dashed and dotted curves represent the spectrum at $z = 0, z = 10\ L_{NL}$ and $z = 20\ L_{NL}$ where $L_{NL} \simeq 1000$ km, respectively.

stationary pulse–so called a "soliton", which can propagate undistorted over a long distance [31].

Another nonlinear effect, with a similar origin to the SPM, is cross phase modulation (XPM), which arises when two or more optical waves copropagate inside a fibre and interact with each other through the nonlinearity. The nonlinear refractive index of a wave does not depend only on its own intensity, but also on an intensity of other copropagating waves.

2.5 Conclusions

In this chapter, a review of the theory and properties of optical fibres in the context of optical communication has been given. To understand the mechanism behind the optical signal transmission in a fibre, important fibre characteristics have been discussed in details, namely optical losses, chromatic dispersion and fibre nonlinearities. A simple derivation of the nonlinear Schrödinger equation that governs the pulse propagation dynamic has also been presented. The equation may be applied to analyse the influence of each fibre characteristics over the dynamic of optical signal propagation in communication systems. We briefly discussed some important effects in this chapter.

Considering those fibre characteristics, we presented the impact of some important effects in optical communication. The effect from fibre loss causes the signal power to decrease exponentially along the propagation. Chromatic dispersion, which is the dominant dispersion effect in single mode fibres, is responsible for pulse broadening as a result of group velocity dispersion (GVD) in which different spectral components travel at different velocities leading to pulse chirping. The effect of higher order dispersion, which causes asymmetric oscillatory pulse structure, has also been reviewed. Finally, we presented the effects of nonlinearity on the pulse spectra through self phase modulation (SPM) and cross phase modulation (XPM).

Chapter 3

Raman effect in optical fibre

3.1 Introduction

As the demand in ultra-high capacity optical links grows exponentially due to a surge in data traffic, the entire optical bandwidth must be used to accommodate an increasing number of data channels. In the 1.55 μm window, there is about 100 nm bandwidth, which corresponds to 15 THz of optical frequency bandwidth. At 40 Gb/s bit rate, the uncertainty relationship gives approximately 40 GHz as the limit for optical frequency spacing. This would mean that the wavelength window might be able to accommodate around 375 channels. However, the fibre nonlinear effects such as cross-phase modulation (XPM) and four-wave mixing (FWM) have always brought about the limit and set the maximum number of channels to around 150 channels for a typical 100 GHz channel spacing of a 40 Gb/s per channel system yielding a total of 6 Tb/s transmission.

Such a large bandwidth has brought conventional optical amplification techniques to their limit. Recently, the most popular optical amplification technology has been Erbium-doped fibre amplifiers (EDFAs) because its high gain and relatively wide bandwidth. However, the typical bandwidth provided by each EDFA is only 20 nm, limited by the emission cross section of Erbium ions. A wider bandwidth can be achieved by the use of multiple dopant, which may widen the bandwidth up to 48 nm [7]. To cover the whole range of 1.55 μm transmission window, one needs to employ two types of EDFA, each of which operates in different bandwidths, namely the C-band (1525 – 1562 nm) and the L-band (1570 – 1615 nm), respectively.

Nevertheless, the recent development of high speed long haul node-to-node transmission has seen not only the demand for an increased transmission bandwidth, but also an increase in requirement of other criteria such as cost reduction by allowing a longer amplifier spacing and reduction of signal distortion to allow a longer transmission link.

To fulfil such demanding criteria, the use of Raman effect in optical fibres enables a development of a new type of optical amplifiers called Raman amplifier. The amplifier relies on the intrinsic properties of silica fibres to obtain signal amplification meaning that the fibre loss can be compensated for *within* the transmission fibre. An amplifier that relies on this principle is commonly known as a distributed Raman amplifier (DRA) [3]. Unlike EDFAs whose amplification band depends on the dopant, Raman gain can be achieved in most bands by adjusting the pump wavelengths. Therefore, the Raman gain band only depends on the availability of the pump wavelengths. Typically, the usable gain bandwidth of a Raman amplifier pumped by a single wavelength is approximately 48 nm. However, a flat gain Raman amplifier covering the whole range of C+L bands was implemented by using 12 pump wavelengths [32, 33].

The distributed nature of Raman amplifiers also helps to improve the optical signal-to-noise ratio (OSNR) [34] along the transmission. As we may see from Figure 3.1, the signal energy does not sink too much when a DRA scheme is employed, thanks to the distributed nature of the amplifier, compared to the case of lumped EDFAs, in which the signal level drops considerably and may be buried at some point by the noise. This will also lead to the fact that the DRA provides a better OSNR than the lumped EDFA, and thus a longer amplification span is possible.

This chapter is devoted to the study of the underlying theory behind Raman amplification. The Raman effect in optical fibre will be reviewed. We will also present the general models to characterise Raman amplifiers and Raman based devices.

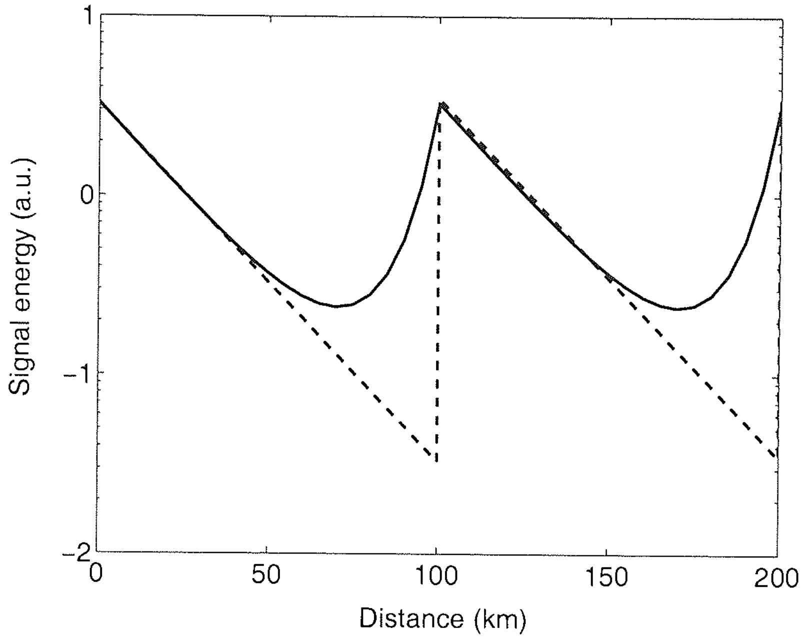

Figure 3.1: Comparison between signal energy evolution in an optical fibre with EDFAs (dashed line) and backward pumped DRAs (solid line). The amplifier spacing is 100 km.

3.2 Raman effect: The historical perspective

In 1928, C.V. Raman made the unexpected and highly surprising discovery that light scattered from a liquid sample did not contain only the light with a wavelength identical to the incident light, but also contained other wavelengths at either side of the light source spectral line in the frequency domain. An interesting feature of this observation is that the foreign spectra followed when the primary light spectrum was displaced, in such a way that the frequency distance between the light source and the foreign spectra was constant. When an extra light source was employed, a new pair of foreign spectra appeared themselves round the source spectrum. Raman investigated the universal character of this phenomenon by experimenting with a large number of media as scattering samples, and found the same effect everywhere. The explanation of this phenomenon was also found by Raman himself. The effect was then named "Raman effect" after its discoverer and won him a Nobel prize in 1930 [35, 36].

Raman effect is the underlying principle of "Raman spectroscopy", which is commonly used in chemistry. Light scattered from sample molecules exhibits a unique frequency shift via spontaneous Raman scattering. Since the Raman frequency shift is very specific for the chemical bonds in molecules, it therefore provides a fingerprint by which the molecule can be identified [37].

In spite of the small Raman gain of silica glass compared to those of crystals or liquids, a long length of low loss optical fibre may permit a low threshold stimulated Raman scattering (SRS) process. In 1972, R.H. Stolen *et. al.* reported the observation of stimulated Raman emission in a single mode silica fibre [38]. They also suggested a potential in employing SRS in light amplification and fibre laser applications. Raman amplifiers were first demonstrated in 1973 [39] and have become a popular field of research since then. However, the lack of high power compact light sources at the time froze the development of Raman optical amplifiers. Much of the work has been overtaken by the development of EDFAs by the late 1980s [40].

Due to a high demand in deploying wider bandwidth for optical links, Raman amplification was resurrected and became a major field of interest as a breakthrough in optical amplification and laser technology in the mid- to late 1990s. By the early 2000s, almost every long haul (300 $\sim$ 800 km) and ultra long haul ($>$ 800 km) optical fibre communication system employ Raman amplification as a part or all of its amplification scheme [34].

To date, research on Raman amplifiers may be divided into two general categories, *i.e.* distributed Raman amplifier and discrete (or lumped) Raman amplifier. Distributed Raman amplifier provides a smooth loss compensation along the propagation of signals in an optical fibre. This thus helps to improve the noise figure and reduce the nonlinear penalty of the amplification allowing a longer amplifier span, higher bit rate and closer channel spacing. On the other hand, discrete Raman amplifier may be used to increase capacity of an optical link by extending the transmission bandwidth to the region in which other amplification techniques are not an option. In light source area, considerable attention has also been paid to the research and development of Raman fibre lasers (or converters) as novel light sources that are highly flexible to operate at any wavelength [41, 42, 43].

3.3 Spontaneous scattering of light in material media

In this section, we describe spontaneous light scattering in materials when an intense light beam is shone into a medium. Light scattering occurs as a result of optical property fluctuations in a material medium. That means, light scattering cannot occur in a completely homogeneous medium. In such a case, the incident light will just transmit through the medium. To clarify this statement, Figure 3.2 shows a diagram demonstrating a completely homogeneous medium illuminated by an incident plane wave. Suppose that an infinitesimal volume dV_1 scatters an incident light in θ direction. There will always be nearby volume dV_2, which scatters the light in such a way that the second scattered light interferes destructively with the first light. An only exception is that the light scattered into the forward direction ($\theta = 0$) does not experience this cancellation and will be transmitted through the medium. Since the same argument can be applied to any volume element in the medium, we may conclude that there can be no scattering in any direction except $\theta = 0$. The scattering in the forward direction is known as coherent forward scattering, and is the origin of the refractive index.

Note that the above argument requires that the medium be *completely* homogeneous. Light scattering can occur as a consequence of fluctuations in any of the optical properties. For instance, if the density of the medium is not entirely uniform, the total number of molecules in the volume elements dV_1 and dV_2 may not be identical. Thus, the destructive interference from between the lights scattered by these two volume elements may not be exact, resulting in a scattering in other direction than $\theta = 0$.

The above argument leads us to the fact that light scattering must be originated from fluctuations in the material's optical properties of some kind. Figure 3.3 depicts the spectrum of scattered light under the most general circumstances. The medium is assumed to be illuminated by a light beam with frequency ν_0. The spectrum has a number of features corresponding to the origin of their type of fluctuation.

Lying on the same frequency as the incident light is the scattering of light by

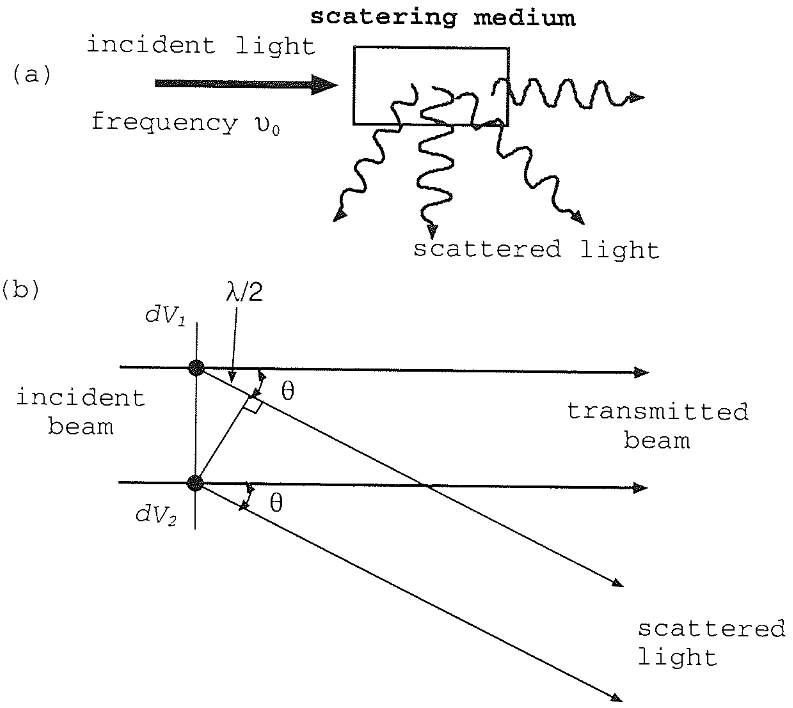

Figure 3.2: Light scattering. (a) Spontaneous scattering. (b) Cancellation of scattered lights in a completely homogeneous medium.

Rayleigh scattering process. The origin of this scattering are the medium density fluctuations. Rayleigh scattering may be considered as a quasielastic scattering because it induces no frequency shift and hence no energy loss in the scattering process.

Next, on both sides of the Rayleigh scattering see two spectral lines of Brillouin scattering. This is the scattering of light from the fluctuations induced by sound waves, that is, from the propagating pressure waves. The Brillouin scattered lights have their frequency shifted to both sides of the incident light frequency. By definition, the components that are shifted to lower frequency are called Stokes components, whereas those components shifted to higher frequencies are known as anti-Stokes components.

Further away from the Brillouin scattering spectral lines, we find light scattered by the Raman scattering process. Raman scattering results from the interaction of the incident light with vibrational modes of the molecules constituting the scattering medium. Equivalently, Raman scattering may be described as the light scattering from optical phonons. In a similar sense, Brillouin scattering can also be considered as the scattering of light from acoustic phonons.

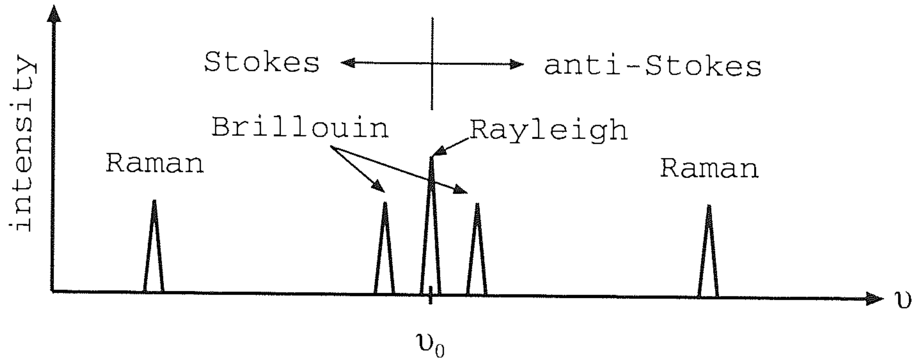

Figure 3.3: Spectrum of light scattering in a medium.

In the Raman scattering process, the incident light interacts with a vibrational mode of a molecule resulting in scattered light with either or both positive and negative frequency shifts. Figure 3.4 depicts the quantum picture of Raman scattering. When a photon is incident to a molecule, two cases of scattering may occur. The first case is that the photon loses its energy and is annihilated to emit a new photon with lower energy, and hence lower frequency. The rest of the energy is converted into a vibrational mode of the molecule or optical phonon (Ω). The emitted photon in this case is a Stokes photon. The opposite situation occurs if the photon gains energy from the optical phonon instead. The emitted photon will have a higher energy than its original and hence a higher frequency. In this case, the emitted photon is referred to as anti-Stokes photon. In the case of optical fibres, the anti-Stokes case is much weaker than the other as it requires molecules in the end state, which are generally much less than the molecules in the ground state.

3.4 Stimulated Raman scattering

So far, we have described the origin of spontaneous scattering of light, which is a rather weak process. Nevertheless, under an excitation by intense light beam, the spontaneous emission can grow stronger in such a way that it *stimulates* an

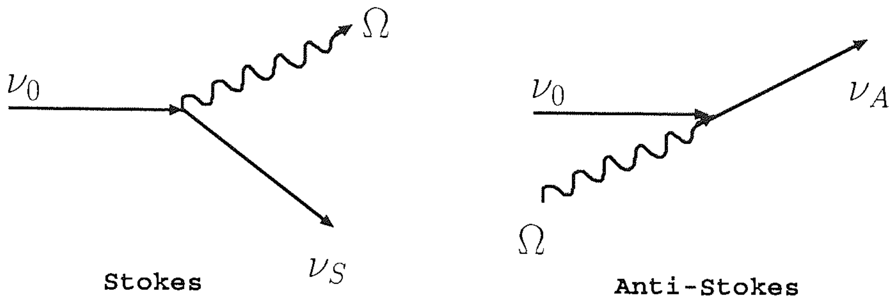

Figure 3.4: Quantum picture of Raman scattering.

emission of scattered light, resulting in a highly efficient scattering process. This version of scattering is referred to as stimulated scattering, and is typically a very strong process. This stimulated scattering can also occur when the light emission is stimulated by an external light beam, by which an amplification of the light beam can take place.

In this section, we aim to gain an understanding of the physical phenomenon behind the stimulated Raman scattering (SRS) by describing it through a simple classical model, and explain the features and applications of Raman gain in both frequency and time domain.

3.4.1 Classical model of stimulated Raman scattering

In the stimulated Raman scattering process, the optical radiation interacts with a vibrational mode of a molecule. In the simple classical model developed by E. Garmire *et. at.* [44] and presented in Ref. [45], the vibrational mode can be assumed to behave like a simple harmonic oscillator of resonance frequency ω_ν and a damping constant γ as shown in Figure 3.5. The internuclear distance is represented by $q_0 + q(t)$, where $q(t)$ is the deviation of the internuclear distance from its equilibrium q_0.

From Figure 3.5, the equation of motion governing the molecular vibration takes the form of

$$\frac{d^2q}{dt^2} + 2\gamma\frac{dq}{dt} + \omega_\nu^2 q = \frac{F(t)}{m}, \tag{3.1}$$

where F represents the force on the vibrational degree of freedom and m is the

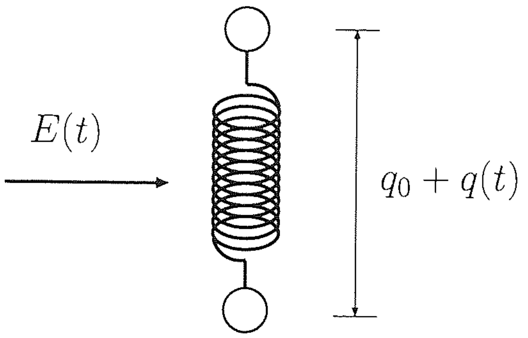

Figure 3.5: Molecular description of stimulated Raman scattering.

reduced nuclear mass.

Here, we make an assumption that the optical polarisability of the molecule depends on the internuclear distance as

$$\alpha(t) = \alpha_0 + \left(\frac{\partial \alpha}{\partial q}\right)_{q=0} q(t), \tag{3.2}$$

where α_0 is the polarisability of a molecule in which the internuclear distance is rested at its equilibrium. Eq. (3.2) implies that the polarisability will be modulated in time when the molecule is set into oscillation. A similar effect will occur to the refractive index via the relation

$$n(t) = \sqrt{\epsilon(t)} = \left[1 + 4\pi N \alpha(t)\right]^{1/2}, \tag{3.3}$$

where N is the number density of molecules. The modulation in time of the refractive index will affect the transmitted light beam in such a way that sidebands separated by $\pm\omega_\nu$ will be generated.

In the presence of an optical field $\boldsymbol{E}(z,t)$, each molecule will become polarised. The induced dipole moment of a molecule is thus given by

$$\boldsymbol{p}(z,t) = \alpha \boldsymbol{E}(z,t). \tag{3.4}$$

Now we may determine the energy required to establish this oscillating dipole moment

$$\mathscr{E} = \frac{1}{2}\langle \boldsymbol{p}(z,t) \cdot \boldsymbol{E}(z,t)\rangle = \frac{1}{2}\alpha\langle \boldsymbol{E}^2(z,t)\rangle, \tag{3.5}$$

where the angular brackets $\langle\cdot\rangle$ denote a time average over an optical period. Hence, one may work out the force on the vibrational degree of freedom exerted by the applied field and see that

$$F = \frac{d\mathscr{E}}{dq} = \frac{1}{2}\left(\frac{d\alpha}{dq}\right)_{q=0} \langle E^2(z,t)\rangle. \tag{3.6}$$

Note that if the applied fields contain two frequency components as it is the usual case for the SRS, Eq. (3.6) shows that the molecular coordinate will experience a time-varying force at the beat frequency between the two field components.

To elaborate the discussion on the influence of the fields over the molecular vibrations, let us assume that the total optical field can be represented as

$$E(z,t) = A_P e^{i(k_P z - \omega_P t)} + A_S e^{i(k_S z - \omega_S t)} + \text{c.c.} \tag{3.7}$$

From Eq. (3.6), the time-varying part of the applied force can be given by

$$F(z,t) = \left(\frac{\partial\alpha}{\partial q}\right)_{q=0} \left[A_P A_S^* e^{i(Kz-\Omega t)} + \text{c.c.}\right], \tag{3.8}$$

where

$$K = k_P - k_S \qquad \text{and} \qquad \Omega = \omega_P - \omega_S. \tag{3.9}$$

Now we are ready to find the solution of Eq. (3.1) with a force term from Eq. (3.8). The following trial solution is adopted:

$$q = q(\Omega)e^{i(Kz-\Omega t)} + \text{c.c.} \tag{3.10}$$

Substitute Eq. (3.8) and (3.10) into Eq. (3.1) and obtain

$$-\omega^2 q(\Omega) - 2i\omega\gamma q(\Omega) + \omega_\nu^2 q(\Omega) = \frac{1}{m}\left(\frac{\partial\alpha}{\partial q}\right)_{q=0} A_P A_S^*. \tag{3.11}$$

Hence one may find the amplitude of the molecular vibration

$$q(\Omega) = \frac{(1/m)\left[\partial\alpha/\partial q\right]_{q=0} A_P A_S^*}{\omega_\nu^2 - \Omega^2 - 2i\Omega\gamma}. \tag{3.12}$$

Since the polarisation of the medium is given according to Eq. (3.2) and (3.4) by

$$\begin{aligned} P(z,t) &= Np(z,t) = N\alpha(z,t)E(z,t) \\ &= N\left\{\alpha_0 + \left(\frac{\partial\alpha}{\partial q}\right)_{q=0} q(z,t)\right\} E(z,t). \end{aligned} \tag{3.13}$$

Here we are interested only in the nonlinear part of the polarisation. It is hence given by

$$\begin{aligned} P^{NL}(z,t) &= N\left(\frac{\partial\alpha}{\partial q}\right)_{q=0}[q(\omega)e^{i(Kz-\Omega t)}+\text{c.c.}] \\ &\times[A_P e^{i(k_P z-\omega_P t)}+A_S e^{i(K_S z-\omega_S t)}+\text{c.c.}]. \end{aligned} \tag{3.14}$$

The nonlinear polarisation in the above equation contains several different frequency components. The part of interest is the Stokes polarisation, which oscillates at frequency ω_S

$$P_S^{NL}(z,t) = P(\omega_S)e^{-i\omega_S t}+\text{c.c.}, \tag{3.15}$$

with the complex amplitude of the Stokes polarisation given by

$$P(\omega_S) = N\left(\frac{\partial\alpha}{\partial q}\right)_{q=0} q^*(\Omega)A_P e^{ik_S z}. \tag{3.16}$$

Substituting Eq. (3.12) into the above equation, one may find that the complex amplitude of the Stokes polarisation yields

$$P(\omega_S) = \frac{(N/m)(\partial\alpha/\partial q)^2_{q=0}|A_P|^2 A_S}{\omega_\nu^2-\Omega^2+2i\Omega\gamma}e^{ik_S z}. \tag{3.17}$$

Now we shall define the Raman susceptibility χ_R via the following expression [6]

$$P(\omega_S) = \frac{3}{4}\chi_R(\omega_S)|A_P|^2 A_S e^{ik_S z}. \tag{3.18}$$

Comparing Eqs. (3.17) and (3.18), we find that the Raman susceptibility is given by

$$\chi_R(\omega_S) = \frac{(4N/3m)(\partial\alpha/\partial q)^2_{q=0}}{\omega_\nu^2-(\omega_P-\omega_S)^2+2i(\omega_P-\omega_S)\gamma}. \tag{3.19}$$

In order to make a connection between the Raman susceptibility recently and the Raman gain coefficient generally used in the context of Raman amplification, we assume the following equation to describe the evolution of the slowly varying field amplitude A_S,

$$\frac{dA_S}{dz} = \frac{\Gamma_S}{2}A_S, \tag{3.20}$$

where

$$\Gamma_S = i\frac{\omega_S}{n_S c}\chi_R(\omega_S)|A_P|^2 \tag{3.21}$$

is the Stokes wave absorption coefficient, and $|A_j|^2 = I_j$ is the field intensity. Since we are interested only in the amplification or attenuation of the field, it is convenient to modify Eq. (3.21) such that

$$\Gamma_S = \frac{\omega_S}{n_S c}\mathrm{Im}\left\{\chi_R(\omega_S)\right\}|A_P|^2. \tag{3.22}$$

Multiplying Eq. (3.20) by A_S^* and making a summation with its complex conjugate, we arrive at

$$\frac{dI_S}{dz} = \Gamma_S I_S = \frac{\omega_S}{n_S c}\mathrm{Im}\left\{\chi_R(\omega_S)\right\} I_P I_S. \tag{3.23}$$

We may compare the above equation with a standard intensity equation governing the power transfer between the pump and Stokes waves [3]

$$\frac{dI_S}{dz} = g_R I_P I_S, \tag{3.24}$$

where g_R is the Raman gain coefficient. Hence we may relate the Raman gain coefficient to the Raman susceptibility as

$$g_R(\Delta\omega) = \frac{\omega_S}{n_S c}\mathrm{Im}\left\{\chi_R(\Delta\omega)\right\}, \tag{3.25}$$

where $\Delta\omega$ is the frequency shift defined as $\Delta\omega = \omega_P - \omega_S$.

By considering Eqs. (3.19) and (3.25), the Raman gain spectrum can be seen to be proportional to a Lorentzian

$$g_R(\Delta\omega) \propto \frac{2\Delta\omega\gamma}{(\Delta\omega^2 - \omega_\nu^2)^2 + (2\Delta\omega\gamma)^2}. \tag{3.26}$$

In the above equation, the extraneous constants have been removed to emphasise the functional form of the equation.

In practice, the Raman gain spectrum can be obtained experimentally. By fitting the Lorentzian profile to the actual Raman gain spectrum, the parameters ω_ν and γ are given in relation to parameters τ_1 and τ_2 measured from a bulk fused silica by

$$\begin{aligned} \tau_1 &= 1/\omega_\nu & \tau_1 &= 12.2 \text{ fs} \\ \tau_2 &= 1/\gamma & \tau_2 &= 32 \text{ fs}. \end{aligned} \tag{3.27}$$

Figure 3.6 illustrates the Raman gain spectrum calculated from Eq. (3.26). The calculated value has been scaled to match the peak of the measured Raman gain curve (dashed line).

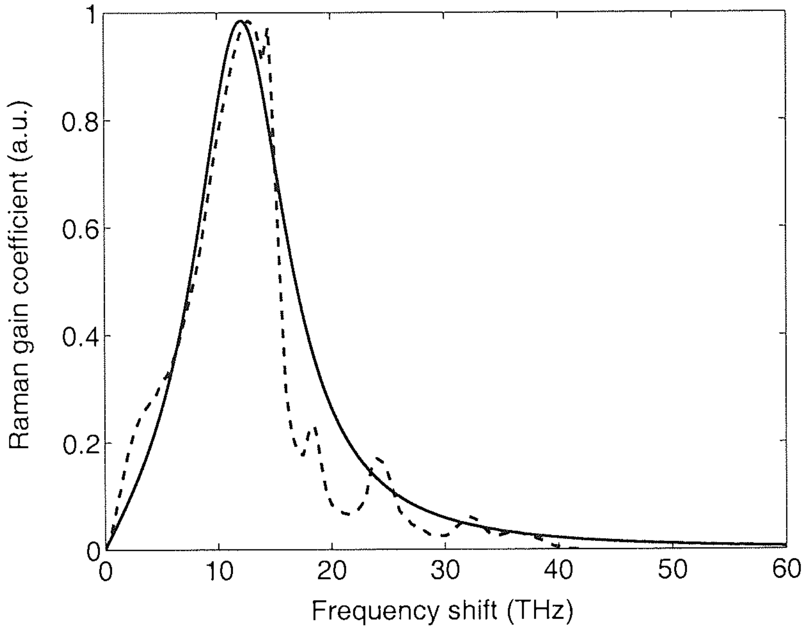

Figure 3.6: Raman gain spectrum obtained from the single-damped-oscillator model (solid curve) compared to a measured Raman gain (dashed curve)

Although, Raman gain calculated from the simple single-damped-oscillator model illustrates the overall gross structure of the Raman gain spectrum, all the fine structures are absent. This is because the glass material is not just a collection of independent silica molecules that all behave in the same manner. Rather, it is a random arrangement of silicon and oxygen atoms with an ensemble of different internal structures consistent with the vitreous nature of the material, which results in a finer structure of the gain spectrum.

It is, however, possible to incorporate the fine structure, in which case the multi-vibrational mode model is required. The Raman gain spectrum is assumed to be a result of superposition of numerous Gaussian profiles equivalent to multi-vibrational mode oscillators. Detailed treatment of this multi-vibrational mode model can be found in Ref. [46].

3.4.2 Power balance model for Raman amplification

In this section, we describe the set of equations governing the power transfer within the Raman amplification process. As developed in the previous section, Eq. (3.24) indicates the variation of Stokes intensity I_S which receives its power from the pump I_P through the SRS process. During the scattering process, an incident photon with energy $h\nu_P$ from the pump is annihilated to generate a lower frequency photon (with energy $h\nu_S$) at the Stokes frequency. SRS is an inelastic scattering process that does not conserve the energy during the conversion; however, the annihilated and created photon numbers are still conserved. Therefore, the change in pump and Stokes photon energy must satisfy the following relation:

$$d\mathscr{E}_P = \frac{\nu_P}{\nu_S} d\mathscr{E}_S, \qquad (3.28)$$

where $\mathscr{E}_j$ denotes the energy of a photon at frequency j. Hence, the interaction between the pump and Stokes waves is governed by

$$\begin{aligned} \frac{dI_S}{dz} &= -\alpha_S I_S + g_R I_P I_S, \\ \frac{dI_P}{dz} &= -\alpha_P I_P - \frac{\nu_P}{\nu_S} g_R I_S I_P, \end{aligned} \qquad (3.29)$$

where I_S and I_P represent the intensity of Stokes and pump wave, respectively. We have also included the material attenuation coefficients α_S and α_P to take into account the losses in the medium. g_R is a shortened form of $g_R(\Delta\nu)$, where $\Delta\nu$ is the frequency difference between the Stokes and pump frequencies.

In the context of optical amplification in optical fibres, it is more convenient to work with optical powers. The beam intensity and its optical power is related by

$$I = \frac{P}{A_{eff}}, \qquad (3.30)$$

where A_{eff} is the effective core area of the fibre. Thus one may write Eq. (3.29) in the power form as

$$\begin{aligned} \frac{dP_S}{dz} &= -\alpha_S P_S + \frac{g_R}{A_{eff}} P_P P_S, \\ \frac{dP_P}{dz} &= -\alpha_P P_P - \frac{\nu_P}{\nu_S} \frac{g_R}{A_{eff}} P_S P_P, \end{aligned} \qquad (3.31)$$

where P_S and P_P are the average power of the signal (Stokes) and pump waves.

To understand how the power transfer initiates, we shall consider a continuous wave (CW) pump beam propagating inside the fibre at the optical frequency ν_P. If a signal beam with frequency ν_S is copropagating inside the fibre, it will get amplified as long as their frequency difference $\Delta\nu = \nu_P - \nu_S$ lies within the bandwidth of the Raman gain spectrum. At the same time, the spontaneous Raman scattering may act as a weak signal and get amplified, too. This will result in the amplified spontaneous emission (ASE) noise. As the spontaneous scattering generates photons within the entire bandwidth of the Raman gain spectrum, all frequency components are amplified. However, the frequency component for which g_R is maximum builds up most rapidly. This fact provides a basic underlying principle of Raman fibre lasers.

Figure 3.7 shows the Raman gain spectrum for fused silica at a pump wavelength of 1 μm. For other pump wavelength the Raman gain can be scaled by using the relation

$$g_{Rj} = \frac{\lambda_0}{\lambda_j} g_{R0}, \tag{3.32}$$

where, g_{Rj} and g_{R0} are the scaled and original Raman gain coefficients with their corresponding pump wavelength λ_j and λ_0, respectively.

Care must be taken when using the Raman gain spectrum shown in Figure 3.7 in the analysis of Raman amplification in optical fibres. As the Raman gain spectrum is measured from a bulk glass sample, it may not be used instantly. In optical transmission, we always assume that the signal in optical fibres is linearly polarised whereas the scramble polarisation of Raman pump is commonly used to avoid gain fluctuation. Hence, the signal will effectively experience half of the possible gain achieved when both pump and signal are in the same polarisation. A factor of 0.5 must be multiplied to the Raman gain to take into account this effect. Note however that Raman lasers rely on the build-up of Stokes beam from spontaneous emission process, which generates light in a random polarisation. In this case, hence, there must be a pair of pump and Stokes photons that are in the same polarisation. The Raman gain spectrum can thus be adopted directly.

Under some circumstances, it is more convenient to measure Raman gain effi-

Aston University

Illustration removed for copyright restrictions

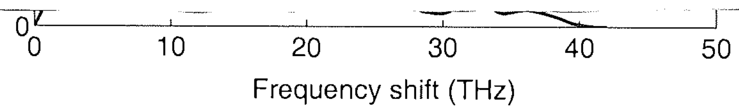

Figure 3.7: Measured Raman gain spectrum for fused silica at a pump wavelength $\lambda_P = 1\mu$m. (after Ref. [47] ©1980 IEEE)

ciency defined as g_R/A_{eff}. The measured parameters have taken into account the mode overlap of pump and signal fields and thus may provide a more accurate estimation of Raman gain in the model. Figure 3.8 shows the Raman gain efficiency for various modern transmission fibres.

One may be able to solve Eq. (3.31) analytically if the pump depletion is neglected. The case is only valid when P_S is small and the interaction length is short. Assuming a non-depleted pump, we can now find the solution for the pump equation as

$$P_P(z) = P_P(0)e^{-\alpha_P z}, \tag{3.33}$$

where $P_P(0)$ represents the injected pump power. Substituting Eq. (3.33) into the Stokes equation of Eq. (3.31), we then find that

$$\frac{1}{P_S}\frac{dP_S}{dz} = -\alpha_S + \frac{g_R}{A_{eff}} P_P(0)e^{-\alpha_P z}. \tag{3.34}$$

The solution of the above equation can be easily found and it takes the form of

$$P_S(z) = P_S(0)\exp\left(-\alpha_S z + \frac{g_R}{A_{eff}} L_{eff} P_P(0)\right), \tag{3.35}$$

Aston University

Illustration removed for copyright restrictions

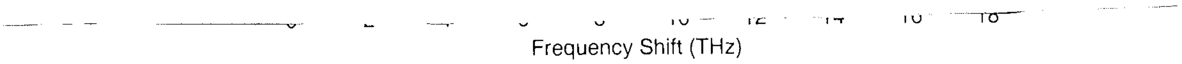

Figure 3.8: Raman gain efficiency spectra for some commercial transmission fibre. The spectra were measured with a reverse-pump at 1455 nm. (after Ref. [28] ©2003 Springer)

where

$$L_{eff} = \frac{1 - e^{-\alpha_P z}}{\alpha_P} \tag{3.36}$$

is the effective interaction length as a result of pump absorption.

3.4.3 Effective core area for stimulated Raman scattering

Due to the relatively wide gain bandwidth of the SRS, there is a range of wavelengths that may be guided by the optical fibre. These wavelengths have their own transverse modes resulting in a different field distribution and hence a different effective area (A_{eff}) for each wavelength. The power transfer thus takes place in the effective area in which the pump and Stokes fields are interacting. To achieve a good accuracy of the model described in Eq. (3.31), one may have to take into account the mode field overlapping of the pump and Stokes fields such that [48]

$$A_{eff} = \frac{\pi}{2}\left(w_P^2 + w_S^2\right), \tag{3.37}$$

where $2w_S$ and $2w_P$ are mode field diameters (MFDs) of the pump and Stokes field, respectively. Assuming that each field distribution has the Gaussian form

$$F_j(x,y) = \exp\left(-\frac{(x^2+y^2)}{w_j^2}\right), \tag{3.38}$$

the mode field radius can be calculated from an empirical formula as follow [29]

$$w_j = a\left(0.65 + 1.619V_j^{-3/2} + 2.879V_j^{-6}\right), \tag{3.39}$$

where the normalised frequency

$$V_j = \frac{2\pi}{\lambda_j} aNA, \tag{3.40}$$

where λ_j, a and NA are wavelength, fibre core radius and numerical aperture, respectively. Details of the optical fibre characteristics are given in Section 2.2.

3.4.4 Transient stimulated Raman scattering

The analysis so far has been focussing on Raman effect from the viewpoint of CW or quasi-monochromatic pulses (valid for longer pulses). The power analysis in frequency domain is sufficient to cover most interesting features of the effect. In recent years, however, the effects of the phenomenon on ultrashort high intensity pulses (width $\lesssim$ 100 fs) have attracted much interest. With such a short pulse, its spectral bandwidth is so large ($\gtrsim$ 1 THz) that Raman scattering can happen between the high and the low frequency components of the same pulse. This effect is referred to as intrapulse Raman scattering [6]. Moreover, as the spectral width of the pulse becomes comparable to the carrier frequency, the derivation of Eq. (2.40) becomes questionable. Therefore, a new version of nonlinear Schrödinger equation (NLS) is needed to take into account the Raman effect contribution.

For convenience, the Raman susceptibility described in Eq. (3.25) can be redefined as

$$g_R(\Delta\omega) = \frac{\omega_S}{n_S c} f_R \chi^{(3)} \mathrm{Im}\left\{\tilde{h}_R(\Delta\omega)\right\}, \tag{3.41}$$

where f_R is the fractional contribution of the delayed Raman response, which can be estimated from the known numerical value of Raman gain peak. The typical value of f_R is about 0.18 [49]. $\widetilde{h}_R(\Delta\omega)$ is the normalised Raman gain spectrum. Hence, we may introduce the corresponding Raman response function $h_R(t)$, which is the Fourier transform of the Raman gain spectrum $\widetilde{h}_R(\Delta\omega)$. From the consideration of the single-damped-oscillations described in Section 3.4.1, the response function is proportional to the Fourier transform of the Lorentzian Raman gain spectrum as such [49]

$$h_R(t) = \frac{\tau_1^2 + \tau_2^2}{\tau_1\tau_2^2} \exp(-t/\tau_2)\sin(t/\tau_1). \tag{3.42}$$

The values of τ_1 and τ_2 as well as their relation to the medium resonance frequency (ω_ν) and the damping constant (γ) have been given in Eq. (3.27). Figure 3.9 illustrates the comparison between the temporal variations of the Raman response function $h_R(t)$ given by Eq. (3.42) and obtained by using the actual Raman gain spectrum of silica glass as shown in Figure 3.7.

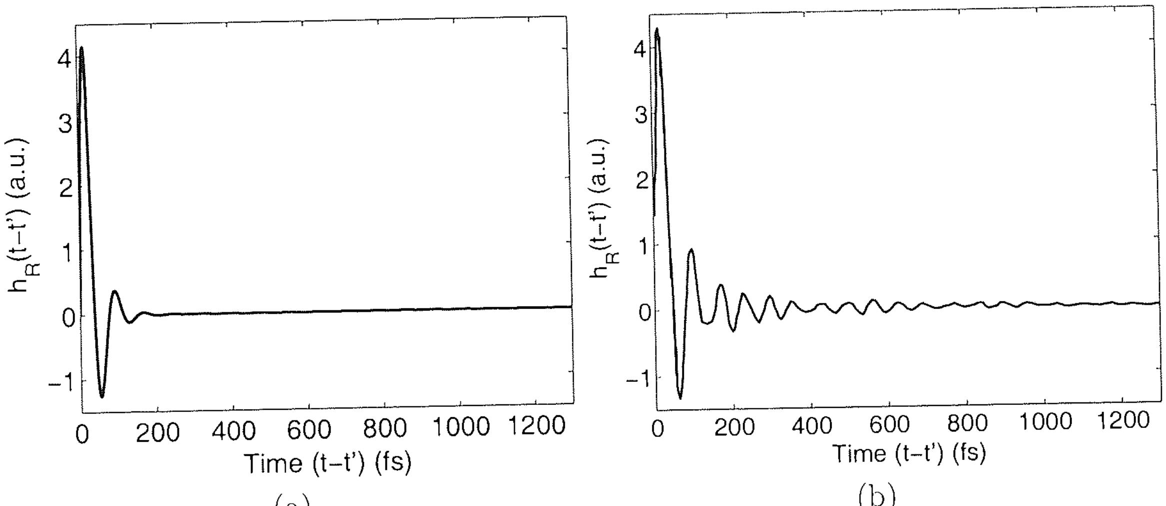

(a) (b)

Figure 3.9: Comparison between the temporal variations of the Raman response function $h_R(t)$ (a) given by the single-damped-oscillator model and (b) obtained by the actual Raman gain spectrum of silica glass.

Now the Raman effect may be included into the NLS equation by assuming the following functional form for the third order susceptibility [49]

$$\chi^{(3)}(t-t_1, t-t_2, t-t_3) = \chi^{(3)}R(t-t_1)\delta(t-t_2)\delta(t-t_3), \tag{3.43}$$

where $\delta(t)$ is the Dirac delta function, defined to be zero everywhere except at $t = 0$, and $R(t)$is the nonlinear response function normalised in a manner similar to the delta function such that $\int R(t)dt = 1$. The nonlinear response should include both the electronic and vibrational (Raman) contributions. By assuming that the electronic contribution is nearly instantaneous, the nonlinear response function $R(t)$ can be related to the Raman response function $h_R(t)$ through

$$R(t) = (1 - f_R)\delta(t) + f_R h_R(t). \tag{3.44}$$

Using the above assumption, the NLS equation described in Eq. (2.38) can be modified to include the Raman effect as

$$\begin{aligned} &i\left\{\frac{\partial Q}{\partial z} + k_0'\frac{\partial Q}{\partial t}\right\} - \frac{k_0''}{2}\frac{\partial^2 Q}{\partial t^2} - \frac{ik_0'''}{6}\frac{\partial^3 Q}{\partial t^3} = \\ &-\frac{i\alpha}{2}Q - \frac{\omega_0}{c}\frac{n_2}{A_{eff}}\left(1 + \frac{i}{\omega_0}\frac{\partial}{\partial t}\right)\left(Q(z,t)\int_0^\infty R(t')|Q(z,t-t')|^2 dt'\right). \end{aligned} \tag{3.45}$$

However, for a pulse larger than 50 fs, the above equation may be simplified considerably by using a perturbative approach. The NLS equation, which approximately includes the effect of a delayed Raman response thus takes the form

$$\begin{aligned} &i\left\{\frac{\partial Q}{\partial z} + k_0'\frac{\partial Q}{\partial t}\right\} - \frac{k_0''}{2}\frac{\partial^2 Q}{\partial t^2} - \frac{ik_0'''}{6}\frac{\partial^3 Q}{\partial t^3} = \\ &-\frac{i\alpha}{2}Q - \frac{\omega_0}{c}\frac{n_2}{A_{eff}}\left(|Q|^2 Q + \frac{i}{\omega_0}\frac{\partial}{\partial t}(|Q|^2 Q) - T_R Q\frac{\partial |Q|^2}{\partial t}\right), \end{aligned} \tag{3.46}$$

where T_R is related to the slope of the Raman gain assumed to vary linearly with frequency in the vicinity of the carrier frequency ω_0, and has a relation to the nonlinear response function by

$$T_R = \int_0^\infty t' R(t') dt'. \tag{3.47}$$

The estimate value of T_R is ~ 5 fs.

Till now, we have considered the effect of SRS within a pulse, which results in pulse distortion. In an optical Raman amplification system using pulsed pump with such a small pulse width that the monochromatic assumption becomes invalid, the NLS equation in Eq. (3.45) has to be modified to account for the interaction between the pump and signal pulses. The dynamics of pulses propagating in the fibre are described by the following coupled equations [6].

$$\begin{aligned}
& i\left\{\frac{\partial Q_P}{\partial z}+k'_P\frac{\partial Q_P}{\partial t}\right\}-\frac{k''_P}{2}\frac{\partial^2 Q_P}{\partial t^2}-\frac{ik'''_P}{6}\frac{\partial^3 Q_P}{\partial t^3}= \\
& -\frac{i\alpha_P}{2}Q_P-\frac{\omega_P}{c}\frac{n_2}{A_{eff,P}}(1-f_R)(|Q_P|^2+2|Q_S|^2)Q_P+R_P(z,t), \qquad (3.48) \\
& i\left\{\frac{\partial Q_S}{\partial z}+k'_S\frac{\partial Q_S}{\partial t}\right\}-\frac{k''_S}{2}\frac{\partial^2 Q_S}{\partial t^2}-\frac{ik'''_S}{6}\frac{\partial^3 Q_S}{\partial t^3}= \\
& -\frac{i\alpha_S}{2}Q_S-\frac{\omega_S}{c}\frac{n_2}{A_{eff,S}}(1-f_R)(|Q_S|^2+2|Q_P|^2)Q_S+R_S(z,t). \qquad (3.49)
\end{aligned}$$

The Raman contribution R_p and R_s are obtained from

$$\begin{aligned}
R_j(z,t) &= i\frac{\omega_j}{c}\frac{n_2}{A_{eff,j}}f_R Q_j\int_{-\infty}^{t}h_R(t-t')\left(|Q_j(z,t')|^2+|Q_k(z,t')|^2\right)dt'+i\gamma_j f_R Q_k \\
&\times\int_{-\infty}^{t}h_R(t-t')Q_j(z,t')Q_k^*(z,t')\exp\left(\pm i\Omega_R(t-t')\right)dt' \qquad (3.50)
\end{aligned}$$

where $j,k=P$ or S such that $j\neq k, \Omega_R=\omega_P-\omega_S$ is the Stokes shift, and f_R represents the fractional Raman contribution.

In the picosecond regime in which pulse widths exceed 1 ps, Eq. (3.48) and (3.49) can be simplified. This is due to the fact that the pulse envelopes vary a little over the time scale over which the Raman response function $h_R(t)$ changes. By treating Q_P and Q_S as constants, the integral in Eq. (3.50) can be performed analytically. As a result the Raman contributions yield the value

$$R_j=i\frac{\omega_j}{c}\frac{n_2}{A_{eff,j}}f_R\left((|Q_j|^2+2|Q_k|^2)Q_j+\tilde{h}_R(\pm\Omega_R)Q_jQ_k^*\right) \qquad (3.51)$$

where $\tilde{h}_R$ is the Fourier transform of the $h_R(t)$ and the negative sign is chosen for $j=S$. At the gain peak located at Ω_R, the real part of $\tilde{h}_R$ vanishes while the imaginary part is related to the Raman gain. By introducing the gain coefficients

$$g_P=2\frac{\omega_P}{c}\frac{n_2}{A_{eff,P}}f_R|\tilde{h}_R(\Omega_R)|, \qquad g_S=2\frac{\omega_S}{c}\frac{n_2}{A_{eff,S}}f_R|\tilde{h}_R(\Omega_R)| \qquad (3.52)$$

the couple amplitude equations become

$$\begin{aligned}
& i\left\{\frac{\partial Q_P}{\partial z}+k'_P\frac{\partial Q_P}{\partial t}\right\}-\frac{k''_P}{2}\frac{\partial^2 Q_P}{\partial t^2}-\frac{ik'''_P}{6}\frac{\partial^3 Q_P}{\partial t^3}= \\
& -\frac{i\alpha_P}{2}Q_P-\frac{\omega_P}{c}\frac{n_2}{A_{eff,P}}\left(|Q_P|^2+(2-f_R)|Q_S|^2\right)Q_P-\frac{g_P}{2}|Q_S|^2Q_P \qquad (3.53) \\
& i\left\{\frac{\partial Q_S}{\partial z}+k'_S\frac{\partial Q_S}{\partial t}\right\}-\frac{k''_S}{2}\frac{\partial^2 Q_S}{\partial t^2}-\frac{ik'''_S}{6}\frac{\partial^3 Q_S}{\partial t^3}= \\
& -\frac{i\alpha_S}{2}Q_S-\frac{\omega_S}{c}\frac{n_2}{A_{eff,S}}\left(|Q_S|^2+(2-f_R)|Q_P|^2\right)Q_S-\frac{g_S}{2}|Q_P|^2Q_S \qquad (3.54)
\end{aligned}$$

For the present Raman amplification technology in optical transmission systems, the simplified version should be sufficient to provide a good accuracy. However, the numerical procedure will be much more complicated when some random effects such as noise and backward Rayleigh scattering, which are important in the realistic system consideration, are taken into account. To ease the calculation, the generalised Raman-amplified gain model may be used. The details of this approach will be described in Chapter 5

3.5 Noise in Raman amplification

In the analysis of optical amplifiers, one of the most important characteristics is the noise, which has become an important limiting factor in high speed optical transmissions. As mentioned in Section 3.2, the distributed nature of Raman amplification helps to reduce the effect of noise significantly by improving the optical signal-to-noise (OSNR) of the signal along the transmission path. In the design and analysis of Raman amplifiers or Raman amplification systems, however, it is important to understand their noise characteristics in order to accurately predict or optimise the overall performance of the systems.

There are two important types of noises in Raman amplification. The first one is the amplified spontaneous emission (ASE) noise, which is a result of spontaneous emission photons getting amplified in the same direction as the signal. The second effect that is responsible for other type of noise is double Rayleigh scattering (DRS). This type of noise can be understood simply by considering the fact that some signal photons get scattered backwards by the Rayleigh scattering process. The scattered photon will get amplified by the pump and may be scattered back again into the signal direction resulting in an in-band noise or multipath interference (MPI).

Apart from those two major noise sources in Raman amplification, other phenomena may contribute to the noise, too. As the Raman process is almost instantaneous, slight pump power fluctuations may cause the individual bit of signal to experience a different gain. Consequently, this leads to the amplitude fluctuations or jitters. This effect is not significant in backward pumping scheme, as each bit will see the pump wave only for a short period of time, and will be averaged out in most cases. In addition, an external noise source such as the noise from the pump laser may also degrade the signal performance, especially when forward pumping scheme is used. Due to these several disadvantages of the forward pumping, the backward pumping scheme is more popular and desirable.

The ASE noise in optical amplifiers has its origin from the spontaneous emission. It has been shown in Ref. [50] that purely spontaneous scattering is approximately equivalent to the injection of a single Stokes photon per mode at the input. Hence, the equivalent noise power injected at the input is

$$P_N = 2N_{sp}h\nu\Delta\nu, \tag{3.55}$$

where $h = 6.6260755 \times 10^{-34}$ [J · s] is the Planck's constant. ν is the optical frequency. $\Delta\nu$ is the effective bandwidth of the signal in which the noise is considered. Note that N_{sp} is related to noise figure F via the relation $F = 2N_{sp}(G-1)/G \simeq 2N_{sp}$. In Raman amplifiers, the spontaneous emission factor N_{sp} is always determined by thermal equilibrium such that

$$N_{sp} = \frac{1}{1 - e^{-h\Delta\nu/kT}} = 1 + \frac{1}{e^{h\Delta\nu/kT} - 1}, \tag{3.56}$$

where $k = 1.380658 \times 10^{-23}$ [J/K] is the Boltzmann's constant. T is the ambient temperature. At room temperature (300 K), the spontaneous emission factor $N_{sp} \simeq 1.1$, which is equivalent to the noise figure of about 3.5 dB.

By incorporating the above ASE noise in the power balance model introduced in Eq. (3.31), we now have a new set of equations describing the power interaction between the signal and pump waves including the ASE noise as

$$\begin{aligned}
\frac{dP_S}{dz} &= -\alpha_S P_S + \frac{g_R}{A_{eff}} P_P P_S + 2h\nu_S\Delta\nu\frac{g_R}{A_{eff}}\left(1 + \frac{1}{e^{h\Delta\nu/kT} - 1}\right) P_P \\
\frac{dP_P}{dz} &= -\alpha_P P_P - \frac{\nu_P}{\nu_S}\frac{g_R}{A_{eff}} P_S P_P - 2h\nu_P\Delta\nu\frac{g_R}{A_{eff}}\left(1 + \frac{1}{e^{h\Delta\nu/kT} - 1}\right),
\end{aligned} \tag{3.57}$$

where $\Delta\nu$ is $\nu_P - \nu_S$.

It is also possible to incorporate the DRS into the above equation. In doing so, we need to consider the contributions of backward propagation too. By introducing the coupled equations for the backward propagation, Eq. (3.57) is modified to take the form of

$$\begin{aligned}\frac{dP_S^{\pm}}{dz} &= \mp\alpha_S P_S^{\pm} \pm \epsilon_S P_S^{\mp} \pm \frac{g_R}{A_{eff}}(P_P^{+} + P_P^{-})P_S \pm 2h\nu_S\Delta\nu\frac{g_R}{A_{eff}}\left(1 + \frac{1}{e^{h\Delta\nu/kT} - 1}\right)P_P^{\pm} \\ \frac{dP_P^{\pm}}{dz} &= \mp\alpha_P P_P^{\pm} \mp \epsilon_P P_P^{\pm} \mp \frac{\nu_P}{\nu_S}\frac{g_R}{A_{eff}}(P_S^{+} + P_S^{-})P_P \mp 4h\nu_P\Delta\nu\frac{g_R}{A_{eff}}\left(1 + \frac{1}{e^{h\Delta\nu/kT} - 1}\right),\end{aligned} \tag{3.58}$$

where $\Delta\nu = \nu_P - \nu_S$. The + and − superscripts and signs indicate the forward and backward propagating waves, respectively. ϵ_j is the Rayleigh scattering coefficient.

In order to analyse the OSNR from this power balance model, it is convenient to separate the signal and noise from each other. We once again modify Eq. (3.58) to consider the signal and noise separately. Thus we obtain

$$\begin{aligned}\frac{dP_S}{dz} &= -\alpha_S P_S + \frac{g_R}{A_{eff}}(P_P^{+} + P_P^{-})P_S \\ \frac{P_P^{\pm}}{dz} &= \mp\alpha_P P_P^{\pm} \mp \frac{\nu_P}{\nu_S}\frac{g_R}{A_{eff}}\left(P_S + n_S^{+} + n_S^{-} + 4h\nu_S\Delta\nu\left(1 + \frac{1}{e^{h\Delta\nu/kT} - 1}\right)\right)P_P^{\pm} \\ \frac{n_S^{+}}{dz} &= -\alpha_S n_S^{+} + \epsilon_S n_S^{-} + \frac{g_R}{A_{eff}}\left(n_S^{+} + 2h\nu_S\Delta\nu\left(1 + \frac{1}{e^{h\Delta\nu/kT} - 1}\right)P_P^{\pm}\right) \\ \frac{n_S^{-}}{dz} &= \alpha_S n_S^{-} - \epsilon_S(n_S^{+} + P_S) - \frac{g_R}{A_{eff}}\left(n_S^{-} + 2h\nu_S\Delta\nu\left(1 + \frac{1}{e^{h\Delta\nu/kT} - 1}\right)P_P^{\pm}\right),\end{aligned} \tag{3.59}$$

where n_S^{+} and n_S^{-} are the forward and backward propagating noise at the signal frequency ν_S, respectively. This model allows for the estimation of the OSNR of a single pump Raman amplifier. It can also be generalised to take into account multiple pumps and signals.

3.6 Conclusions

This chapter provides a theoretical background on Raman effect, which will be applied in various applications described in later discussions. Starting from the historical perspective when the spontaneous Raman scattering was first observed as a curious phenomenon in C.V. Raman's laboratory in 1928, the discussions have been elaborated to cover the stimulated version of the scattering which is the underlying principle of most Raman related applications in the context of optical communications.

The literature on stimulated Raman scattering (SRS) in optical fibres has been reviewed. The most interesting use of the SRS is its potential to turn an optical fibre into a gain medium providing a distributed gain to signals. Raman amplifiers have been proven to help improve the optical signal-to-noise ratio (OSNR) due to its low noise and distributed gain structure. Lumped Raman amplifiers have also drawn much attention as they represent a breakthrough in the area of ultra-wide band optical amplification.

In Section 3.4, we presented an overview of SRS theory to gain some understanding of the process. A simple single damped oscillator model has been presented to describe the fundamentals of the SRS. The model was successful in approximately predicting the Raman gain spectrum. We also developed a power balance model to describe the power interaction in a simple Raman amplifier. The model will be extended to characterise various Raman applications such as Raman fibre lasers and amplifiers in later chapters.

For ultra-high speed transmission (hence ultrashort pulse width), the SRS may become a detrimental effect. The intrapulse Raman scattering may cause the pulse breaking and hence signal distortion. To account for this effect, the standard nonlinear Schrödinger (NLS) equation must be modified. The transient Raman response, obtained from the Fourier transform of Raman gain spectrum, was included in the nonlinearity part of the NLS equation to incorporate the Raman transient effect. We also presented the transient model that governs amplification of short pulsed signals amplified by a pulsed pump.

Lastly, the noises in Raman amplification has been described. Two of the most important noises in Raman amplification are the amplified spontaneous emission (ASE) noise and double Rayleigh scattering (DRS) noise. The origin of ASE noise is the amplification of spontaneous Raman scattering whereas the DRS noise comes from the signal and ASE noise being scattered back and forth into the signal direction. A brief description of those two noises has been given in Section 3.5. We have also presented the incorporation of ASE and DRS noise into the power balance model to accurately predict the characteristics of Raman amplifiers and lasers.

Chapter 4

Raman fibre lasers

4.1 Introduction

At present, laser technology has played a vital role and taken part in various areas such as display technology, optical recording, high precision sensing, biomedical engineering and especially optical communication. The demand in new laser technology has grown rapidly as the technological world evolves. A higher power and better beam quality laser is always needed at every new step of those technological advancements.

In optical communications, the laser is an important part, used as the data signal sources in optical transmitters, and as the pump sources for optical amplifiers. Due to an abrupt surge in the demand of ultra-high capacity optical transmissions, a wide range of laser wavelengths are required to provide pumping for optical amplifiers to maximally utilise the entire transmission window of the optical fibre.

In addition, Raman amplifiers deliver a relatively wide bandwidth, and has recently gained much popularity in many high-speed long-haul optical transmission systems. Multiwavelength pumping has been proven to be a key technique to expand the gain bandwidth of distributed Raman amplification, which has become an attractive technology in ultralong long haul, high bit rate transmission systems. [51, 52]. To enable multiwavelength pumping technology, lasers with flexible output wavelengths are required.

Unfortunately, conventional lasers such as semiconductor lasers or rare-earth-doped fibre lasers failed to provide such a flexibility, because their lasing wavelengths are tied to the emission cross section of dopant ions [40].

The discussions in Chapter 3 pointed out that the Raman fibre laser (RFL), whose operating wavelength depends only on the wavelength of its pump, can be used as a pump source operating at the wavelength inaccessible by the others, and hence providing a coverage of the entire 1.5 μm transmission window of the optical fibre. Table 4.1 summarises the spectral band in the 1.5 μm window for a standard single mode fibre (SMF) [53].

Band	Wavelength range (nm)
S^+-band	1450 – 1490
S-band	1490 – 1530
M-band	1530 – 1570
L-band	1570 – 1610
L^+-band	1610 – 1650

Table 4.1: Spectral band under 0.3 dB/km loss in ordinary single mode optical fibre

Recently, a considerable attention has been focusing on the development of the RFLs as a breakthrough in laser pumping technology. Because of its flexibility to operate at almost every wavelength, the RFL can be used as a pump source for Raman or Erbium-doped fibre amplifiers. Moreover, its advantage of wider available wavelengths also shows a great potential to find an application in other areas such as biomedical engineering and sensing.

This chapter is devoted to the study and development of various types of Raman fibre lasers. The principle of the lasers, their designs, modelling and characteristics will be described.

4.2 Modelling of Raman fibre lasers

The principle of Raman fibre lasers (RFLs) relies on the wavelength conversion through stimulated Raman scattering (SRS) process, in which the pump light propagating down the gain medium fibre interacts with the medium molecules. This interaction results in a power transfer from the pump into a Stokes wave with a lower frequency. The frequency shift is always determined by the peak of the Raman gain spectrum of the medium. A cavity, used to confine and resonate the pump wave, will help to improve and maximise the conversion efficiency. The power transfer to a higher Stokes wave is possible by employing a nested cavity, in which each Stokes line is resonated, and transfers its power into a higher order one. In general, the reflectivity of each cavity mirror is high, except for the one at the output end of the cascade that has a moderate reflectivity to couple the light out of the cavity. The cavity is generally formed by pairs of fibre Bragg gratings (FBGs) due to its simplicity and compatibility to be spliced or connected directly to the gain medium fibre. Figure 4.1 depicts the schematic diagram of a generic cascade RFL.

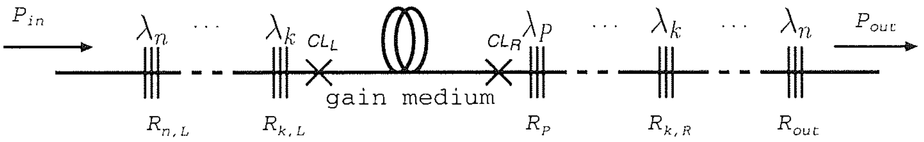

Figure 4.1: Schematic diagram of Raman fibre lasers.

In order to characterise a RFL, the power balance model described in Section 3.4.2 may be used. A modification of Eq. (3.31) is made to account for both forward and backward propagating waves and the cascade structure of the laser as illustrated in Figure 4.2, where L is the cavity length of the laser. Hence, the power balance model used to characterise a $(n+1)$-stage RFL is as follow:

$$\begin{aligned}
\frac{dP_P^{\pm}}{dz} &= \mp\alpha_P P_P^{\pm} \mp \frac{\nu_P}{\nu_1}\frac{g_R^{P1}}{A_{eff}^{P1}}(P_1^{+}+P_1^{-})P_P^{\pm} \\
\frac{dP_1^{\pm}}{dz} &= \mp\alpha_1 P_1^{\pm} \pm \frac{g_R^{P1}}{A_{eff}^{P1}}(P_P^{+}+P_P^{-})P_1^{\pm} \mp \frac{\nu_1}{\nu_2}\frac{g_R^{12}}{A_{eff}^{12}}(P_2^{+}+P_2^{-})P_1^{\pm} \\
&\;\vdots \\
\frac{dP_k^{\pm}}{dz} &= \mp\alpha_k P_k^{\pm} \pm \frac{g_R^{k-1,k}}{A_{eff}^{k-1,k}}(P_{k-1}^{+}+P_{k-1}^{-})P_k^{\pm} \mp \frac{\nu_k}{\nu_{k+1}}\frac{g_R^{k,k+1}}{A_{eff}^{k,k+1}}(P_{k+1}^{+}+P_{k+1}^{-})P_k^{\pm} \\
&\;\vdots \\
\frac{dP_n^{\pm}}{dz} &= \mp\alpha_n P_n^{\pm} \pm \frac{g_R^{n-1,n}}{A_{eff}^{n-1,n}}(P_{n-1}^{+}+P_{n-1}^{-})P_n^{\pm},
\end{aligned} \tag{4.1}$$

where the subscripts $P, \ldots, k, \ldots, n$ denote the pump wavelength and Stokes orders of frequency $\nu_P, \ldots, \nu_k, \ldots, \nu_n$, respectively. The forward and backward propagating waves are indicated by the $+$ and $-$ signs. The optical fibre used as the gain medium in this RFL has the attenuation coefficient α_j at wavelength j. The Raman gain coefficient g_R^{lm} and effective core area A_{eff}^{lm} are determined by considering the fact that the pump at wavelength l interacts with the Stokes wave at wavelength m causing the power to transfer from the pump wave at wavelength l to m through the SRS process.

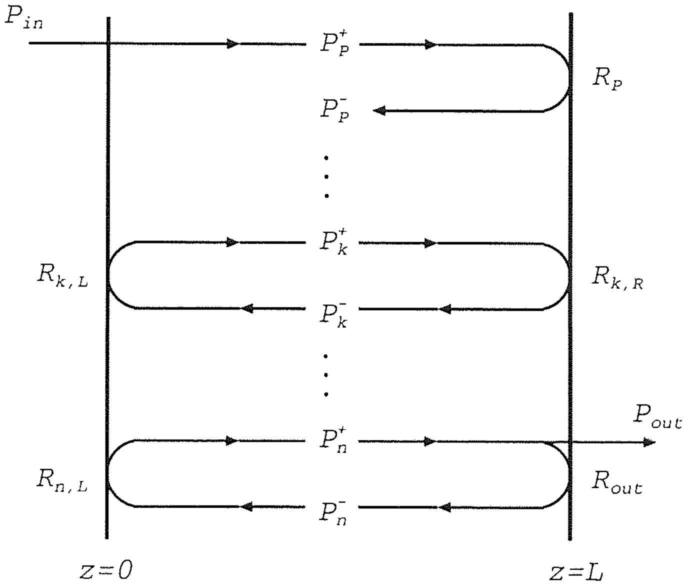

Figure 4.2: Problem definition for the Raman fibre laser power balance model.

The problem defined in Figure 4.2 is a boundary value problem (BVP), in which one may need a set of boundary conditions to solve. The boundary conditions are given by the injected pump power at the input end and the reflection at each FBG.

Thus, the boundary conditions yield

$$\begin{aligned}
P_P^+(0) &= P_{in} & P_P^-(L) &= P_P^+(L)\cdot R_P\cdot CL_R^2 \\
& \vdots & & \\
P_k^+(0) &= P_k^-(0)\cdot R_{k,L}\cdot CL_L^2 & P_k^-(L) &= P_k^+(L)\cdot R_{k,R}\cdot CL_R^2 \\
& \vdots & & \\
P_n^+(0) &= P_n^-(0)\cdot R_{n,L}\cdot CL_L^2 & P_n^-(L) &= P_n^+(L)\cdot R_{out}\cdot CL_R^2,
\end{aligned} \tag{4.2}$$

where CL_L and CL_R are the linear connector losses at the left and right ends of the cavity, respectively. The output power may be obtained as

$$P_{out} = P_n^+(L) - P_n^-(L) = P_n^+(L)(1 - R_{out}). \tag{4.3}$$

Any standard algorithm for solving BVPs may be used to integrate Eq. (4.1) given the above boundary conditions. Note that, neglecting the contribution given by spontaneous Raman scattering, the system does not have a unique solution. A possible solution is when the pump is depleted only by the linear loss without generating any Stokes wave at all. This trivial solution may be avoided by providing a good set of initial values and looking for the only stable solution. Throughout this thesis, we have adopted the shooting method [54] and the fixed step Runge-Kutta algorithms to integrate the BVP equations.

4.3 Single stage Raman fibre laser

In order to test the validity of the model described in the previous section, a single stage RFL has been modelled and compared to the experimental results. A low Germanium doped fibre is used as the gain medium. Details of the fibre parameters are summarised in Table 4.2. The laser is designed to lase at the output wavelength of 1150 nm with the pump wavelength at 1090 nm. The cavity is formed by a pair of FBGs. Each FBG except the output coupler has the reflectivity of 99%, which is the limit of the present technology. The output coupler terminating the cascade resonating cavity is a FBG with a reflectivity of 20%. It is important to include the connector losses appearing at the concatenation between the FBGs and the gain medium fibre. Both connector losses take the value of ~ 0.27 dB. The fairly high value of the connector losses are due to the mode field mismatch between two types of fibres used as the gain medium and FBGs and the imperfection of the optical connectors.

Parameters	Value
cut off wavelength	0.95 μm
index difference	0.06
core diameter	5.5 μm
GeO_2 concentration	4 mol%
attenuation at 1.09 μm	0.85 ± 0.05 dB/km
attenuation at 1.15 μm	0.70 ± 0.05 dB/km
g_R/A_{eff}	$1.3355 \times 10^{-3} \quad (\mathrm{Wm})^{-1}$

Table 4.2: Fibre parameters for the single stage RFL.

Two configurations of the laser have been tested namely the configuration with a cavity length of 500 m and 1000 m. Figures 4.3 and 4.4 show the comparison of the output power characteristics between the experiment and numerical results for $L = 500$ m- and 1000 m-cases, respectively. The results show a fairly good agreement between the numerical simulations and the experiments. This, thus, confirms the validity of the model.

As one may see from both cases, the laser output power varies almost linearly with the input power. For a convenience in comparing the laser performance, we shall define the conversion efficiency, which is a ratio between the output and input power as

$$\eta = \frac{P_{out}}{P_{in}}, \tag{4.4}$$

where η is the conversion efficiency. P_{out} and P_{in} are the output and input powers of the laser, respectively. For this RFL, the conversion efficiency is approximately 64% for $L = 500$ m and 72% for $L = 1000$ m. However, the cavity is clearly not optimised. A better performance is expected for the RFL with an optimal cavity length. In addition, the RFL exhibits a laser thresholds about 0.8 W and 0.5 W for the $L = 500$ m- and 1000 m-cases, respectively. A further detailed discussion on the laser threshold will be given in the next section.

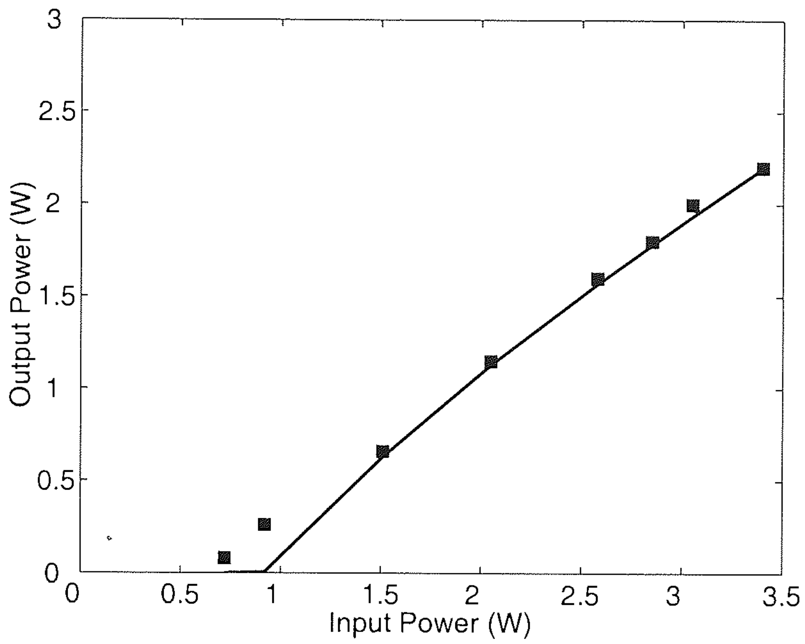

Figure 4.3: Output power characteristic comparison between the experiment (square dot) and values predicted by the power balance model for a single stage RFL with $L = 500$ m (solid line).

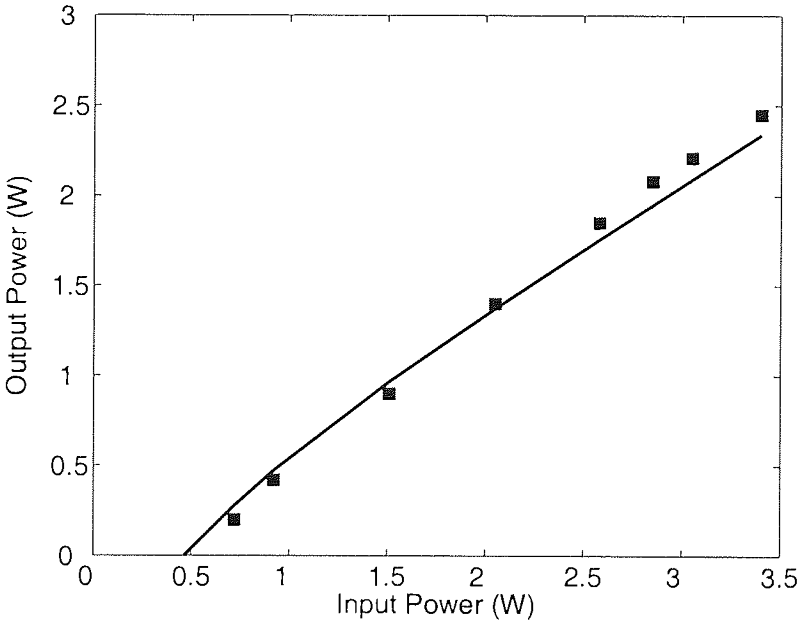

Figure 4.4: Output power characteristic comparison between the experiment (square dot) and values predicted by the power balance model for a single stage RFL with $L = 1000$ m (solid line).

4.4 Two stage Raman fibre laser based on Phosphosilicate core fibre

Multi-wavelength pumping is a key technique to expand a gain bandwidth of distributed Raman amplification that rapidly becomes an attractive technology in ultra-long, high-bit rate transmission. Recently, a considerable attention has been drawn to the development of the RFLs operating at 1480 nm region, which can be used as a pump source for Raman and Er-doped fibre amplifiers. However, the pump source for the laser itself must be widely available with an inexpensive price. More importantly for telecom applications, the whole device should require a minimum maintenance and has a long duration.

RFL pumped by a double-cladded Yb-doped fibre laser is an interesting candidate to fulfil such a demanding requirement. The Yb-laser is pumped by a laser diode array with emission wavelength of 978 nm. The cladding mode pumping of the Yb-laser allows an efficient coupling of the laser diode array's large spot size into the Yb-fibre. This way, a large array of laser diodes can be used, and consequently results in a high pump power. While propagating in the Yb-fibre, the cladding mode light stimulates the emission of a laser light in the fibre core with a scrambled polarisation instantly suitable for the RFL. The output wavelength is set by a pair of FBGs forming a resonating cavity. In our design, the output wavelength of the Yb-laser is set to 1061 nm.

Typically, many RFLs employ GeO_2 doped fibre as the active medium, which possesses a rather small Stokes shift of 440 cm^{-1}. [1] As a consequence, a large number of cascades in Raman frequency conversion to the long-wavelength are required, leading to a complicated and expensive optical scheme and decreased efficiency. An alternative way to avoid this complication is the use of P_2O_5 doped silica fibres, due to the large Raman shift (1330 cm^{-1}) in the Phosphosilicate fibre, the number of required cascades can be significantly reduced [55]. Figure 4.5 depicts the comparison of the Raman gain spectrum between the Phophosilicate and Germanosilicate fibres.

---

[1] The frequency in the unit of "wave number per m" may be used in some parts of the thesis to maintain the consistency with the literature, and is simply defined as $\nu|_{m^{-1}} = 1/\lambda$. It is related to the frequency is Hz by $\nu|_{Hz} = c \cdot \nu|_{m^{-1}}$, where c is the speed of light.

In this section, we discuss the characteristics and parameter optimisation of a two-stage RFL based on Phophosilicate fibre and investigate the tolerance of a found optimal regime against variations of the laser characteristics.

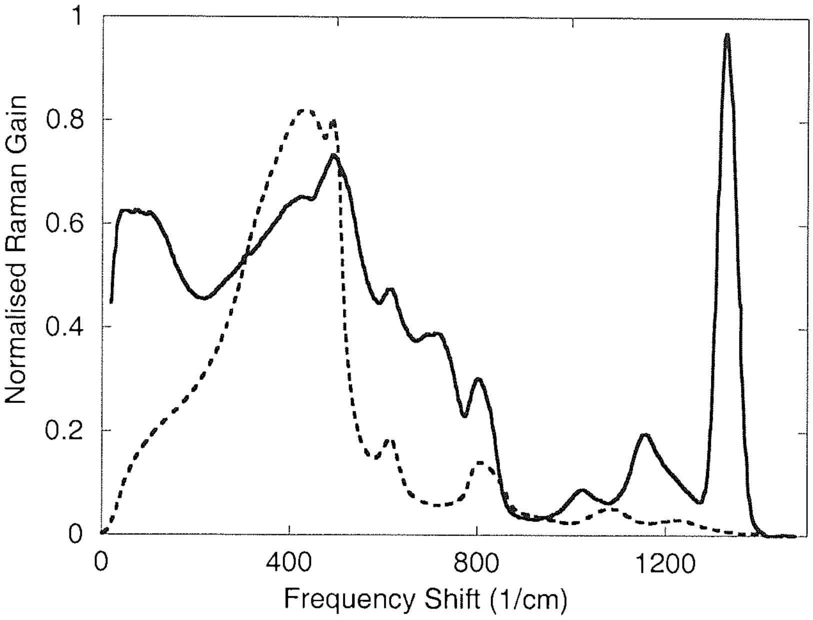

Figure 4.5: Raman gain spectrum comparison between the P-doped (solid curve) and Ge-doped (dash curve) fibres.

4.4.1 Laser characteristics

In the simulations, the model described in Section 4.2 is employed. We numerically solve Eq. (4.1) for both forward and backward propagating waves using two-point boundary conditions given by the reflections at the Bragg gratings. The model includes realistic parameters for both distributed and lumped (splicing) losses.

Since the Raman shift in Phosphosilicate is around 1330 cm^{-1}, conversions from 1061 to 1480 nm occurs through cascaded Raman scattering involving intermediate wavelength of 1240 nm. The laser presents the Phosphosilicate-core single-mode fibre with 13 mol.% P_2O_5 doping level. This corresponds to the Raman gain coefficients and fibre losses as summarised in Table 4.3. Bragg reflectors with 99% reflectivities except for the output reflector are considered.

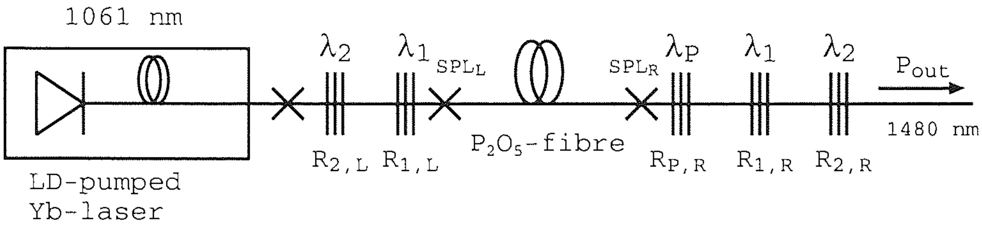

Figure 4.6: Schematic diagram of the two-stage RFL based on P-doped fibre.

The sum of one-path splicing loss and background loss of Bragg gratings in this scheme was equal to 2×4%=8% (0.36 dB).

Wavelength(nm)	α (dB/km)	G_R/A_{eff} (Wm^{-1})
$\lambda_1 = 1061$	1.55	1.29×10^{-3}
$\lambda_2 = 1240$	0.92	0.94×10^{-3}
$\lambda_3 = 1480$	1.75	

Table 4.3: Simulation parameters

Figure 4.7 shows the pump and Stokes power evolutions inside the cavity when R_{out} is either (a) 15%, (b) 1% or (c) 50%, respectively. The cavity length L and input power P_{in} are fixed to 500 m and 2 W in all cases. In case (a) the output reflectivity is close to optimal for the given L. One may see the differences when comparing (a) to other two cases. In the case of (b) R_{out} = 1%, the output reflectivity is too low resulting in a very low power transfer rate from the intermediate into the output wavelength. The intermediate wavelength power grows considerably high but stimulates only a small amount of power transfer into the output wavelength. In case (c) the R_{out} is too low. Although, the power of the forward propagating wave at the output wavelength is rather high inside the cavity as a result of high stimulation due to the high output reflectivity, only a little of the output wavelength light can be coupled out of the cavity. Therefore, it is essential to optimise the output coupler reflectivity to achieve as high laser performance as possible.

Another key parameter that affects the laser performance is the cavity length. Too long cavity length will incur an unnecessary fibre loss whereas a too short cavity does not provide enough gain to stabilise and achieve full laser performance.

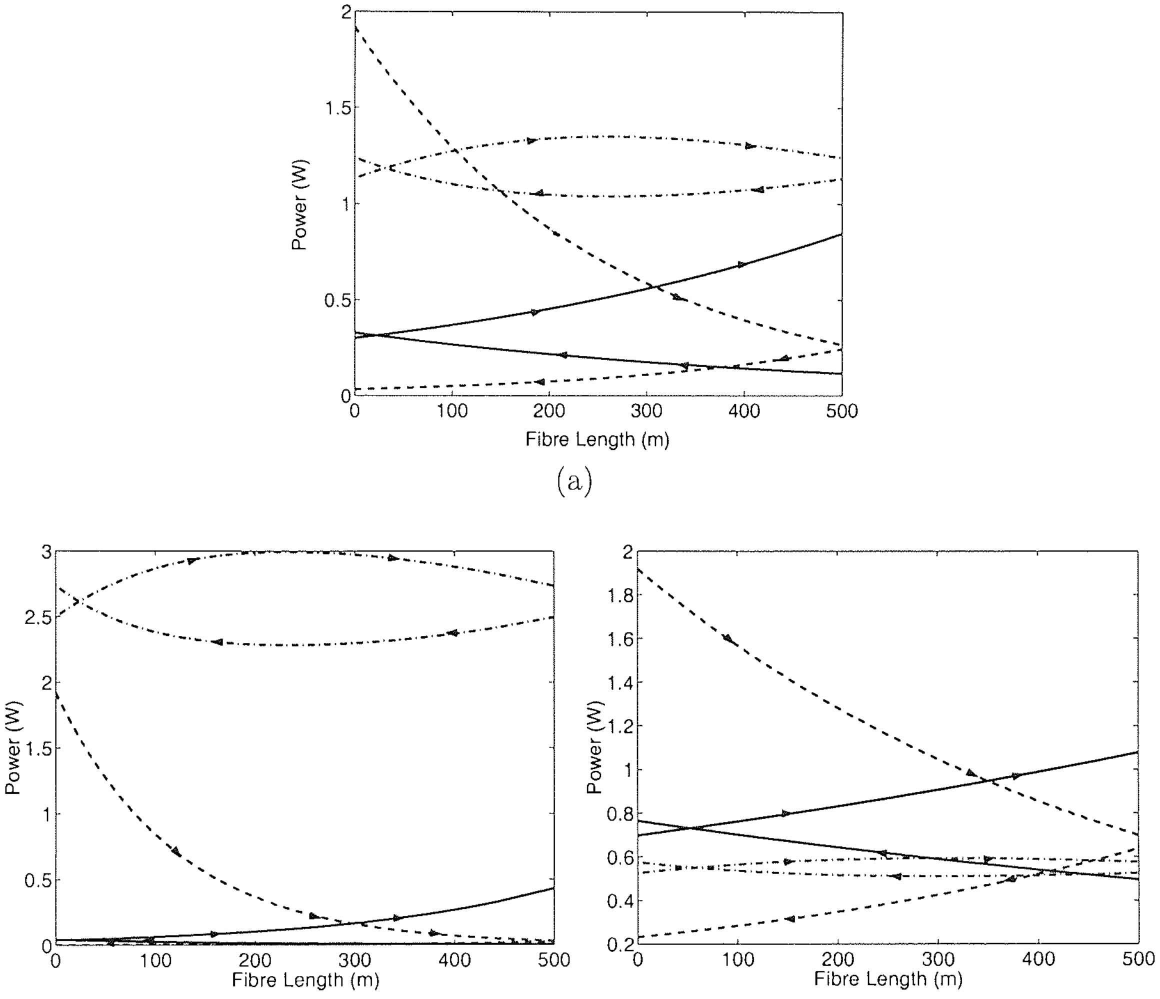

(a)

(b)

(c)

Figure 4.7: Power evolution of forward (right arrow) and backward (left arrow) pump and Stokes waves. Dashed, dash-dotted, and solid lines represent the pump, 1st- and 2nd-order Stokes powers, respectively. (a) $R_{out} = 15\%$ (b) $R_{out} = 1\%$ (c) $R_{out} = 50\%$.

4.4.2 Cavity optimisation

To optimise the laser parameters we evaluate performance of the RFL considering as a figure of merit the conversion efficiency η defined in Eq. (4.4). Performance of RFLs depends on several parameters, first of all: reflectivity of the output coupler R_{out}, cavity length L and input power P_{in}. First, we performed numerical optimisation of the laser performance varying these three main parameters. Figure 4.8 illustrates the optimal reflectivities at different P_{in} for a number of fixed cavity lengths. Both the optimal R_{out} and cavity length L decreases exponentially when P_{in} increases. Note that shorter cavity lengths require higher reflectivity for the same input power.

Under the optimal output reflectivities the conversion efficiencies at each L have been calculated for a range of P_{in}. Figure 4.9 depicts a plot of those characteristics.

By considering both graphs in Figure 4.8 and Figure 4.9 one may be able to deduce from the graphs approximately the optimal parameters of the RFL for a given P_{in} ranged from 2–15 W [56]. For example, for an RFL operating at P_{in} = 2 to 4 W the cavity length should be approximately 500 m for the best conversion efficiency according to Figure 4.9. This corresponds to the optimal reflectivity of the output coupler of 15 to 7.5%. Note that in the experiment presented later, it was convenient to choose 15% reflectivity.

Obviously, for simple RFL configurations the full-scale optimisation in the space (R_{out}, L, P_{in}) is possible. However, due to high tolerance of the optimal regime against deviations of the key parameters (as it will be shown in Section 4.4.4) the approximate optimisation approach that we used here gives a relatively good estimate of optimal parameters and is very effective for practical system design.

4.4.3 Full scale optimisation

To confirm the validity of the approximate optimisation approach, the full scale optimisation has been performed [57]. Figure 4.10 illustrates the contour plots of η over the variations of R_{out} and L for a few P_{in}. According to the plots, an optimal regime is found for each P_{in} yielding the highest performance. The conversion efficiency, however, increases as the input power is increased because the higher input power enhances the conversion rate from the lower Stokes wave into the higher one. It is interesting to note that both optimal cavity length and optimal output coupler reflectivity move towards the lower values as the input power increases. This can be explained as follows. First as discussed, the higher input power enhances the conversion rate. The cavity for a laser operating at a high power input needs not to be long, which otherwise will suffer from the fibre attenuation. Similarly, the output coupler reflects some power back. This backward light again helps to enhance the conversion rate, which is especially important for low input power. However, too strong output coupler limits the laser performance and should be weaker for higher

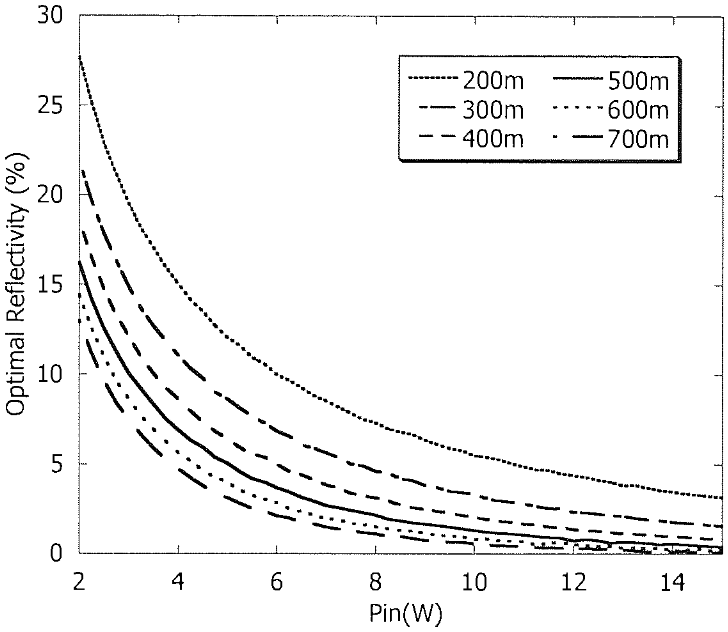

Figure 4.8: Optimal reflectivity versus input power

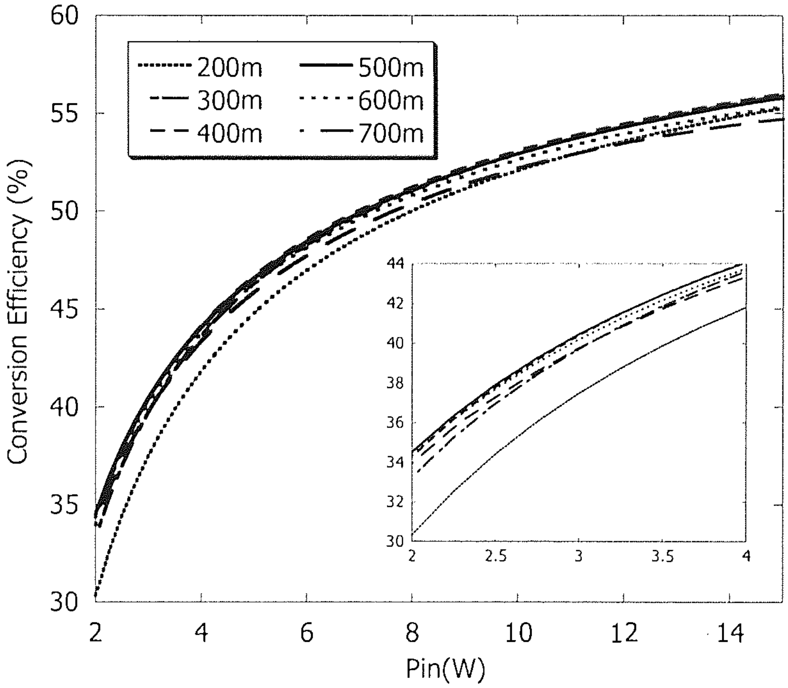

Figure 4.9: Conversion efficiency versus input power

input power.

Therefore, there is a different optimal regime for each input power. Fortunately, due to the high tolerance of the optimal regime against deviations of the key parameters (as discussed in the previous section), the RFL parameters optimised at a chosen P_{in} is good enough for a practical design without loosing too much performance.

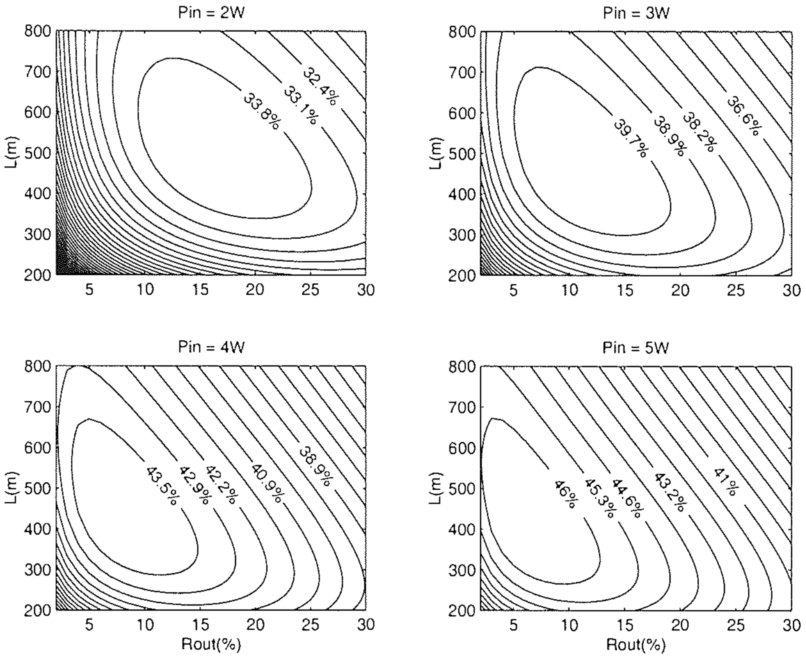

Figure 4.10: Contour plots of the conversion efficiency at several P_{in}

4.4.4 Tolerance of the optimal regime

Next we investigate the tolerance of laser performance to the deviations in a reflectivity of the output coupler and cavity length. Figure 4.11 (a) and (b) show the conversion efficiencies of the RFL under the deviations from the optimum of R_{out} (L=500 m) and L (R_{out}=15%), respectively. One may see that the laser performance degrades by less than 1% for ±5% R_{out} deviated from its optimal value. So does the laser performance with L deviation of ±100 m from its optimum. We also notice that overestimate of those two parameters does less harm to the laser performance and the conversion efficiency in this case degrades only a little bit beyond the optimal values.

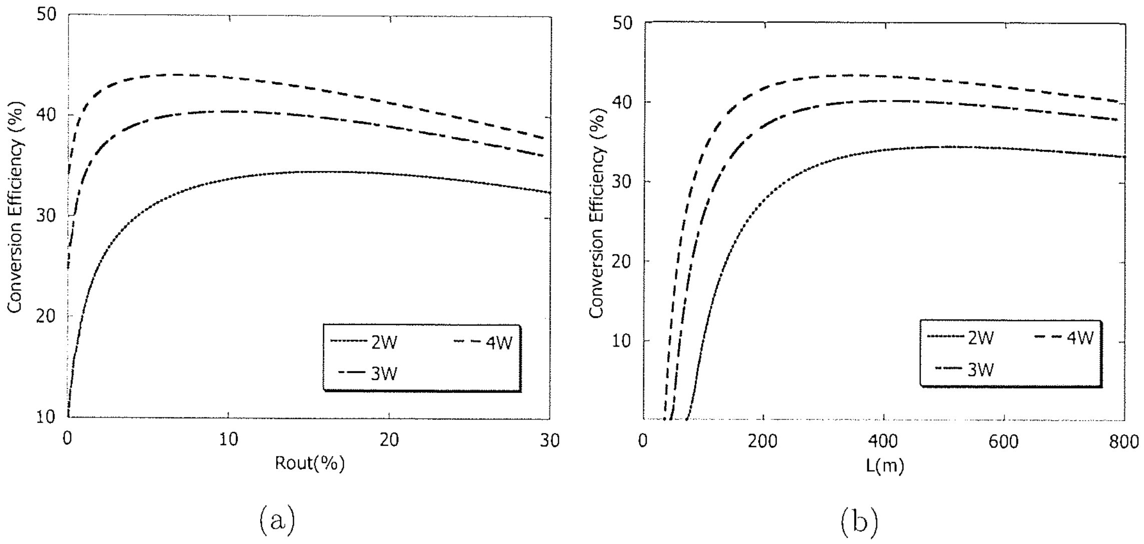

(a)

(b)

Figure 4.11: Tolerance of the RFL performance to the deviation in (a) the reflectivity of output coupler (L = 500 m) (b) the cavity length (R_{out} = 15%)

4.4.5 Laser threshold

Threshold power is an important characteristic of lasers. Threshold indicates the minimum input pump power that the laser can operate stably. In this section, we aim to investigate how the laser threshold is affected by variations of key parameters that will lead to a suitable design of the RFL in terms of its performance and flexibility. Figure 4.12 illustrates the variation of the RFL power threshold as a function of various parameters. First of all, Figure 4.12 (a) shows the plot of power threshold versus the cavity length. The laser threshold decreases exponentially with a longer cavity length and rolls off to the value about 0.65 W when the cavity length exceeds 700 m. This effect can be explained easily by considering the fact that the longer cavity length, the longer gain that the lights experience and hence a lower threshold power. One may thus allow a longer cavity length in the design to lower the threshold power. This can be done without sacrificing too much conversion efficiency due to a high tolerance of the optimal regime discussed in Section 4.4.4. The power threshold also decreases exponentially when the output reflectivity is increased as illustrated in Figure 4.12 (b). Similarly, this is because the output wavelength light reflected into the cavity by a high reflectivity output coupler stimulate the power transfer rate from the light at the intermediate wavelength into the output wavelength.

Lastly, we investigated the behaviour of the threshold power when the cavity is optimised for various input powers. We found that the threshold power is increased when the laser is optimised for a higher input power. For example, the threshold power is approximately 0.65 W when the cavity is optimised for P_{in} = 2 W but is increased to 1 W for the 5 W-optimised laser. This effect can be described by referring to the contour plots of the conversion efficiency at several input powers shown in Figure 4.10. For a cavity optimised for a higher input power, the shorter cavity length and lower output reflectivity are required resulting in a higher threshold power.

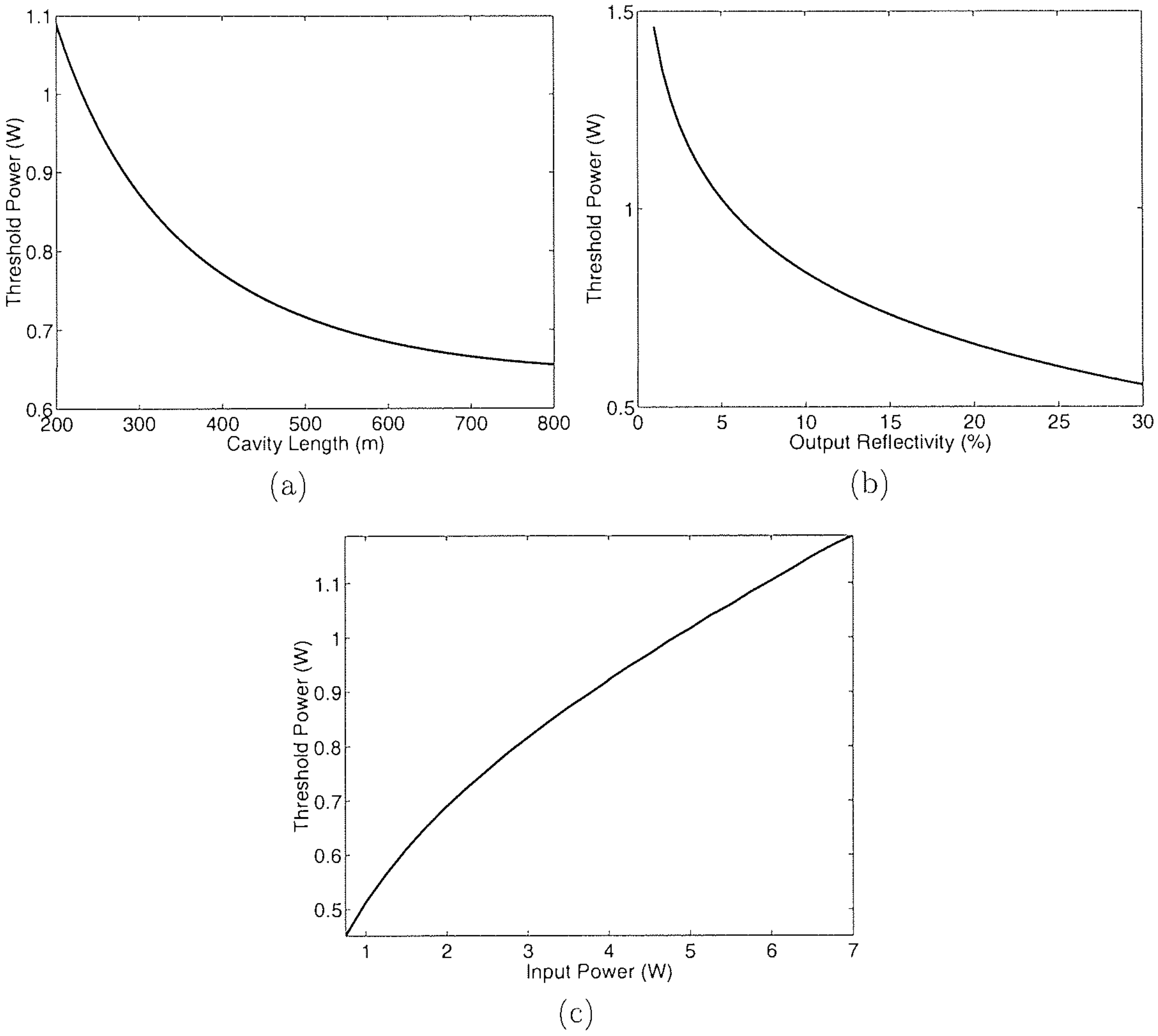

(a)

(b)

(c)

Figure 4.12: Laser threshold variation as a function of (a) cavity length (b) output reflectivity and (c) optimal laser configuration for various input power.

4.4.6 Comparison with experimental results

In this section, we shall compare our predicted characteristics with the experimental results [56]. In the experiment, The fibre length was 500 m. The converter was pumped by Yb-doped double-clad fibre laser having a maximum output power of 3.8 W at 1061 nm. This power was achieved for a power of semiconductor source at 978 nm equal to 5.8 W. The dependence of the output power at 1480 nm versus the input power of the pumping Yb laser and results of the simulation are shown in the Figure 4.13. Using the results of the modelling and optimisation, there is a good agreement between theoretical predictions and the experimental results.

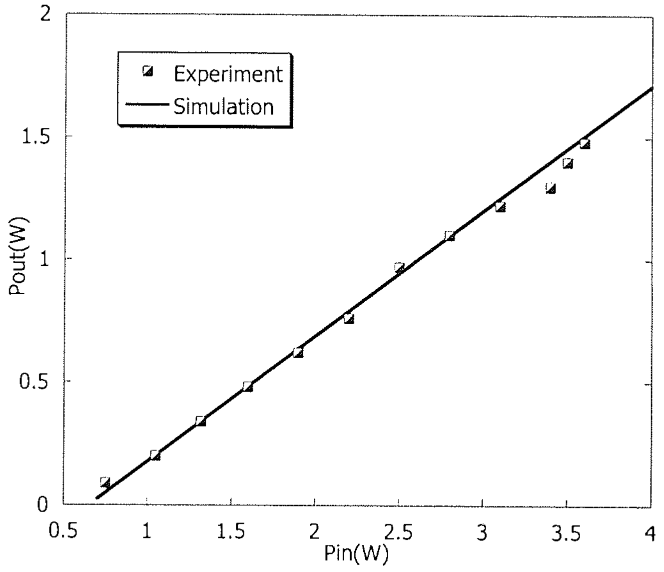

Figure 4.13: Comparison of the experimental results and simulations ($R_{out} = 15\%, L = 500$ m)

4.5 Efficiency spectrum comparison between Ge- and P-doped Raman fibre laser

WDM signal bandwidth expansion is very important to achieve high capacity in transmission systems. Multi-wavelength pumping is a promising technique to expand the gain bandwidth of distributed Raman amplification that rapidly becomes an attractive solution for high bit rate transmission systems. One of the major advantages of the Raman technique is the freedom it allows in a design of gain spectrum by detuning pumping wavelengths and powers. However, a distributed Raman amplifier requires high power pump source. Raman fibre laser (RFL) pumped by a high power double-clad Yb-doped fibre laser is an interesting candidate to be used as a pump source for such amplifier.

For multi-wavelength pumping, it would be important to know the spectral dependence of RFL's performance. In this section, applying numerical modelling, we investigate the total efficiency of RFLs pumped by an Yb-doped fibre laser with two types of active gain media, namely GeO_2 doped and Phosphorus doped silica fibres.

In order to design a RFL operating at a range of output wavelengths for multi-pumping applications, it is necessary to take into consideration the spectral dependence of the efficiency of both Yb-doped fibre laser and the RFL. Here, we shall define a slope efficiency, which is used as a figure of merit to indicate the laser performance. The slope efficiency is defined as a slope of the linear variation between the output and input power of the lasers such that

$$\eta_{slope} = \frac{\Delta P_{out}}{\Delta P_{in}}. \tag{4.5}$$

Unlike the conversion efficiency defined by Eq. (4.4), the slope efficiency eliminates the contribution of threshold power.

Figure 4.14(a) presents the measured slope efficiency spectrum of the Yb-doped fibre laser. To ensure the highest efficiency at each emission wavelength, the slope efficiency of the Yb-laser has been measured under the optimal condition of its parameters [58]. High efficiency of Yb-doped laser (70 − 80%) is achieved over a relatively wide range of wavelengths, namely 1060 − 1130 nm. The efficiency decreases at the short and long wavelength are due to the reabsorption of the emitted light by Yb-ions and the decrease of the Yb-ion emission cross section, respectively.

We then perform numerical simulations to evaluate the slope efficiency spectrum of the RFLs over a range of emitting wavelength from 1400−1600 nm. Figure 4.14(b) illustrates the simulation results. Two active gain media, namely Ge-doped (5-stage converter) and P-doped (2-stage converter), are used for comparison. The parame-

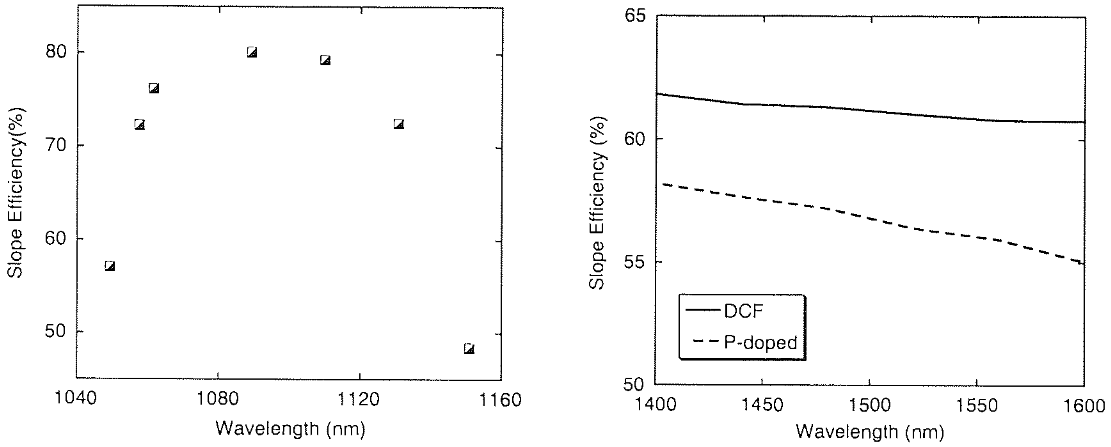

(a) (b)

Figure 4.14: Slope efficiency spectrum of (a) Yb-doped fibre laser (b) Ge-doped (DCF) and P-doped RFLs

ters of the Ge-doped fibre are similar to those of a standard dispersion compensating fibre (DCF)[2] and the parameters of the P-doped fibre are identical to the previous section. The slope efficiency at each wavelength is again evaluated under the optimal condition of the key parameters. Unlike the Yb-doped fibre laser, we can see that the slope efficiencies of both types of active gain media do no vary much over the range of emitting wavelengths. Therefore, the spectrum of the total slope efficiency is dominated by the property of Yb-doped fibre laser.

In Figure 4.15 the total slope efficiency of the 5-stage Ge-doped, the 6-stage Ge-doped and the 2-stage P-doped RFLs pumped by the Yb-doped double-clad fibre laser are illustrated.

Emitting wavelength ranged from 1400 nm to 1600 nm can be covered by using the 5-stage Ge-doped RFL for the shorter wavelength window, and either the 6-stage Ge-doped or the 2-stage P-doped RFL for the longer wavelength window. The 6-stage Ge-doped RFL shows lower performance than the 5-stage one due to an excess cavity loss in the extra stages required. Its performance is almost similar to that of the 2-stage P-doped RFL with slightly lower slope efficiency. In practical applications, however, the P-doped RFL may be more preferable for this longer wavelength window due to its simpler structure that will lead to the more reliable operation and possibly reduce the total cost of the systems.

---

[2] The detailed specification of the DCF and other fibres can be found in Appendix A.

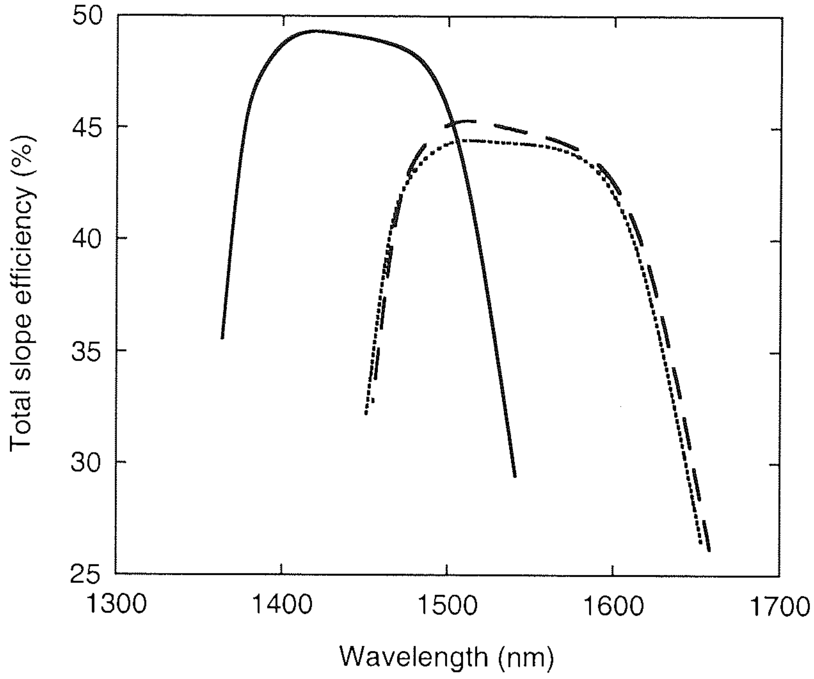

Figure 4.15: Total slope efficiency of the RFLs pumped by the Yb-doped double clad fibre laser (solid line ≡ 5-stage Ge-doped, dotted line ≡ 6-stage Ge-doped, dashed line ≡ P-doped RFLs)

4.6 Composite Raman fibre laser for 1.6 μm spectral window

A main advantage of exploiting the Raman wavelength conversion technique is the freedom it allows to design a laser operating at any desired wavelength, since the wavelength conversion by using stimulated Raman scattering (SRS) process depends only on the pump wavelength and Raman frequency shift. A variety of Raman fibre lasers (RFLs) emitting a laser beam in a range of $1.1 - 1.6$ μm have been demonstrated [57, 59]. Theses devices can be used as pump sources for Raman fibre amplifiers in various telecommunication windows. Moreover, the possibility to operate at any wavelength within $1.1 - 1.6$ μm potentially makes the RFLs possible to be employed in other applications such as spectroscopy, medicine, etc.

However, it is possible to extend the emitting wavelength of the RFLs to L- and L$^+$-bands to provide a laser source operating in the wavelength within $1.6 - 1.75$ μm spectral region. The L- and L$^+$-band laser source can potentially find a number of applications in the areas of eye-safe Lidars, gas spectroscopy, medicine and other practical applications [60]. Note that the emission wavelength of the rare-earth doped fibre lasers do not cover this spectral range. For example, the common Er- and Er:Yb-doped fibre lasers only operate within a range of 1.53 – 1.6 μm whereas the Tm-doped lasers operate in the 1.8 – 2 μm spectral region. Therefore, the RFLs has provided a reasonable solution to develop a light source for the 1.6 – 1.75 μm spectral region.

In this section, we present a practical realisation of a RFL source operating at 1.65 μm. The modelling technique described in Section 4.4 is extended to characterise the laser characteristics. The validity and accuracy of the model is to confirm with experimental results. Finally, we suggest the optimal design to maximise the performance of the RFL.

4.6.1 Laser design

As discussed in the previous section, Yb-doped fibre laser pumped by a high power laser diode array is the most suitable pump source for RFLs due to its long durability and simplicity to connect to the RFLs.

In general, utilisation of a gain medium fibre with an appropriate choice of Yb-laser emission wavelength allows one to design a RFL that operates within the infrared (IR) region. The upper limit of the emission wavelengths is determined by the growth of optical losses in the longer wavelengths. In practice, such a limit is about 1.8 μm. However, to design a RFL to operate at 1.65 μm requires 6–7 stages of conversions if a Germanosilicate fibre (with a typical Raman shift of 440 cm^{-1}) is used as a gain medium. This solution does not provide an efficient wavelength conversion because there will be an extra loss in every new stage added. Furthermore, more complicated optical scheme may lead to a less stable system.

A Phosphosilicate core fibre, on the other hand, possesses a larger Raman shift (1330 cm^{-1}) and may be used to reduce the number of stages required. For example, the conversion of the Yb-laser radiation wavelength to the output within a range of 1.47 – 1.6 μm requires merely two stages (see Section 4.5 for more details). Unfortunately, the use of P-doped fibre Raman shift alone does not provide the output in the range of $1.65 - 1.75$ μm as another conversion corresponding to the Raman shift of SiO_2 or SiO_2/GeO_2 glass is required. One of the possible solution is to employ the silica Raman shift of the same Phosphosilicate core fibre. However, the considerably high optical losses of the Phosphosilicate core fibre in the desired operating region may limit the performance of the RFL. Therefore, a composite scheme combining both Germanosilicate and Phosphosilicate cavities is proposed. The schematic diagram of the composite RFL is illustrated in Figure 4.16. The scheme is comprised with a two stage P-doped RFL and a single stage Ge-doped RFL.

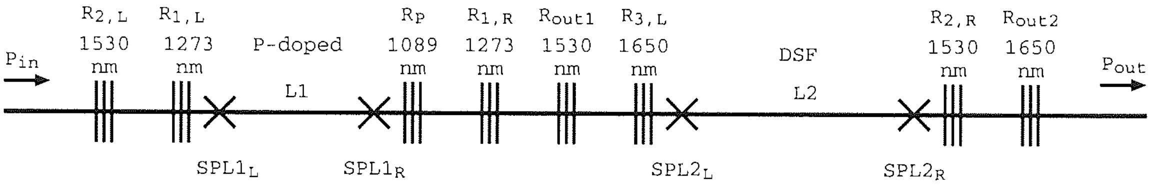

Figure 4.16: Schematic diagram of the composite Raman fibre laser.

4.6.2 Cavity modelling and laser characteristics

To characterise the composite RFL, the model described in Section 4.2, which accounts for both forward and backward propagations of the pump and Stokes waves within the cavity, can be used to model each stage of the composite RFL. In this case, the RFL is comprised with a cascade of two cavities. The first cavity is a two stage P-doped RFL that converts the light from 1089 nm to 1530 nm. The output light is then coupled into the second cavity made of a standard telecom dispersion shifted fibre (DSF). The second cavity is responsible for providing the last 440 cm^{-1} shift yielding the output at 1650 nm wavelength. To accurately predict the characteristics of the RFL, we should account for the residual light reflected backward from the second into the first cavities, too. The problem is defined in Figure 4.17.

To include the effect of the residual light reflected back into the first cavity, we

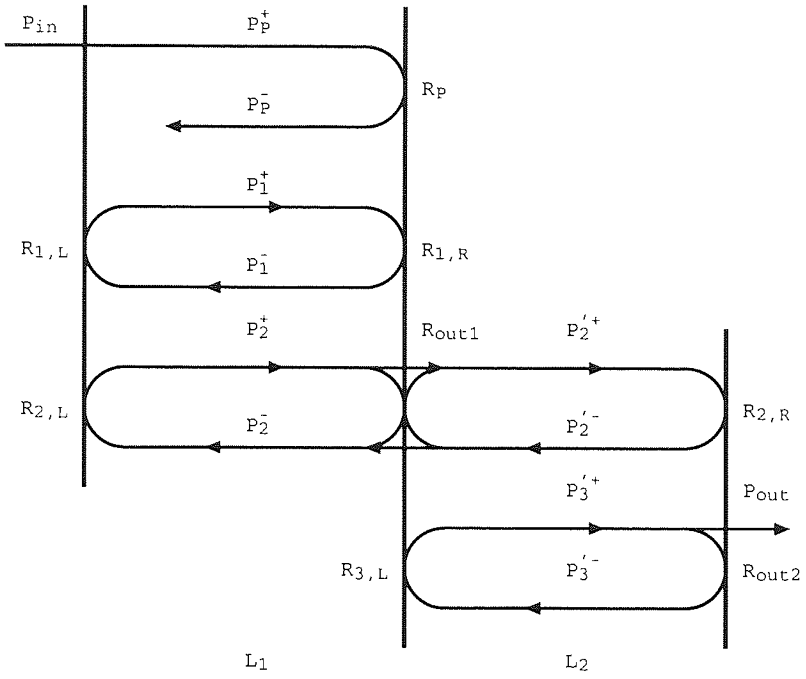

Figure 4.17: Problem definition of the composite Raman fibre laser.

must satisfy the following boundary conditions:

$$P_P^+(0) = P_{in}, \qquad P_2'^-(L_1 + L_2) = P_2'^+(L_1 + L_2) \cdot R_{2,R},$$

$$P_1^+(0) = P_1^-(0) \cdot R_{1,L}, \qquad P_3'^-(L_1 + L_2) = P_3'^+(L_1 + L_2) \cdot R_{out2},$$

$$P_2^+(0) = P_2^-(0), \cdot R_{2,L}$$

$$\begin{aligned}
P_P^-(L_1) &= P_P^+(L_1) \cdot R_P, \\
P_1^-(L_1) &= P_1^+(L_1) \cdot R_{1,R}, \\
P_2^-(L_1) &= P_2^+(L_1) \cdot R_{out1} + P_2'^-(L_1)[1 - R_{out1}], \\
P_2'^+(L_1) &= P_2'^-(L_1) \cdot R_{out1} + P_2^+(L_1)[1 - R_{out1}], \\
P_3'^+(L_1) &= P_3'^-(L_1) \cdot R_6,
\end{aligned} \tag{4.6}$$

where P_k is an average power of the optical wave at wavelength k-th. R_j is the reflectivity of the fibre Bragg grating used to form the cavities. In our simulation, all FBGs except the output couplers (R_{out1} and R_{out2}) have the reflectivity of 99%.

To solve this model, we use the shooting to a fixed middle point (*i.e.* where $z = L_1$) algorithm with the boundary conditions given in Eq. (4.6). The parameters of the Phosphosilicate core fibre and the DSF used as the gain media for the first and second cavity are given in Table 4.4 and 4.5, respectively.

Wavelength(nm)	α (dB/km)	g_R/A_{eff} $(\mathrm{Wm})^{-1}$
$\lambda_1 = 1089$	1.41	1.21×10^{-3}
$\lambda_2 = 1273$	0.84	0.74×10^{-3}
$\lambda_3 = 1530$	0.81	

Table 4.4: Simulation parameters of the first stage (P-doped fibre).

Wavelength(nm)	α (dB/km)	g_R/A_{eff} $(\mathrm{Wm})^{-1}$
$\lambda_1 = 1530$	0.20	0.51×10^{-3}
$\lambda_2 = 1650$	0.25	

Table 4.5: Simulation parameters of the second stage (DSF).

By solving the boundary value problems (BVP), we obtained the power evolution of each pump and Stokes waves in both cavities of a composite RFL as shown in Figure 4.18. The first and second cavities of the composite RFL have the lengths of 540 m and 1560 m, respectively. The reflectivity of the output couplers in this case are 6% and 15% for the first cavity and the second cavity.

4.6.3 Comparison with the experimental results

Next step is to verify the simulation with the experimental results. The proposed composite RFL was fabricated at the Russian Academy of Science [61]. As for the initial pump source, a laser diode array with a maximum power of 8 W at 978 nm has been used to pump the Yb-doped double clad laser, which provides the input to the composite RFL at 1089 nm. The achieved maximum power of the Yb-laser is 5.1 W. As mentioned in Section 4.3, the realistic splicing or connection losses have to be included to ensure the accuracy of the model. The connection losses can be incorporated into Eq. (4.6) in the same manner as in Eq. (4.2). The value of the connection losses including the spot size mismatch losses was found to be close to 0.25 dB.

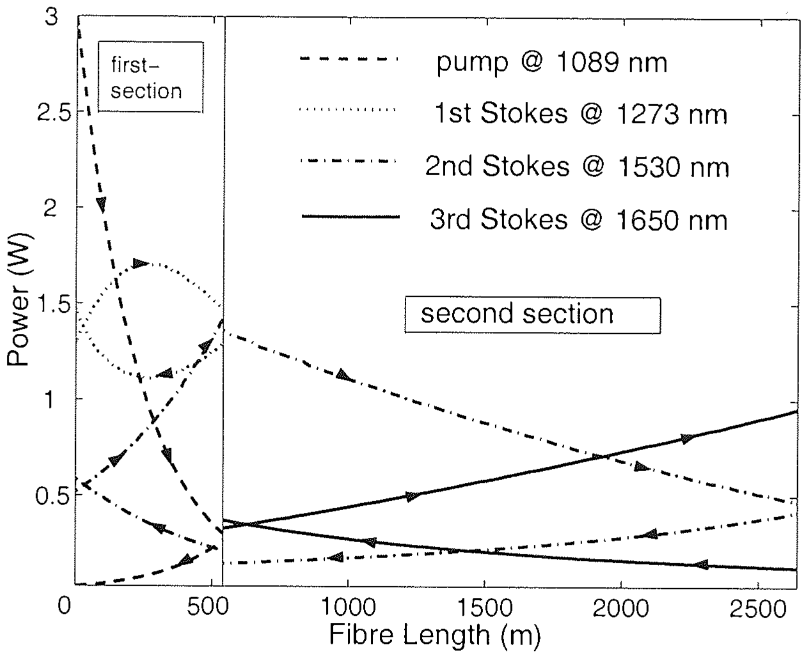

Figure 4.18: Power evolution of forward (right arrow) and backward (left arrow) pump and Stokes waves with in the cavity of composite Raman fibre laser.

Figure 4.19 depicts the output power at 1650 nm as a function of the input power at 1089 nm. A good agreement between the experiment and numerical simulation has been obtained.

4.6.4 Optimisation of the composite Raman fibre laser

We follow the procedure described in Section 4.4 to optimise for performance of the composite RFL. The power conversion efficiency defined in Eq. (4.4) is used as the figure of merit. For the case of double cavity composite RFL, the degree of freedom include the output coupler reflectivities (R_{out1} and R_{out2}) and both cavity lengths (L_1 and L_2). Simple down hill simplex algorithm was applied to search for the optimal setting for a number of given input powers. Table 4.6 summarises the optimal configurations at some given input powers compared to the configuration used in the experiment. As the conversion efficiency also depends on the input power, the parameters shown in Table 4.6 is for the best conversion efficiency achieved when the laser is operating at each input power.

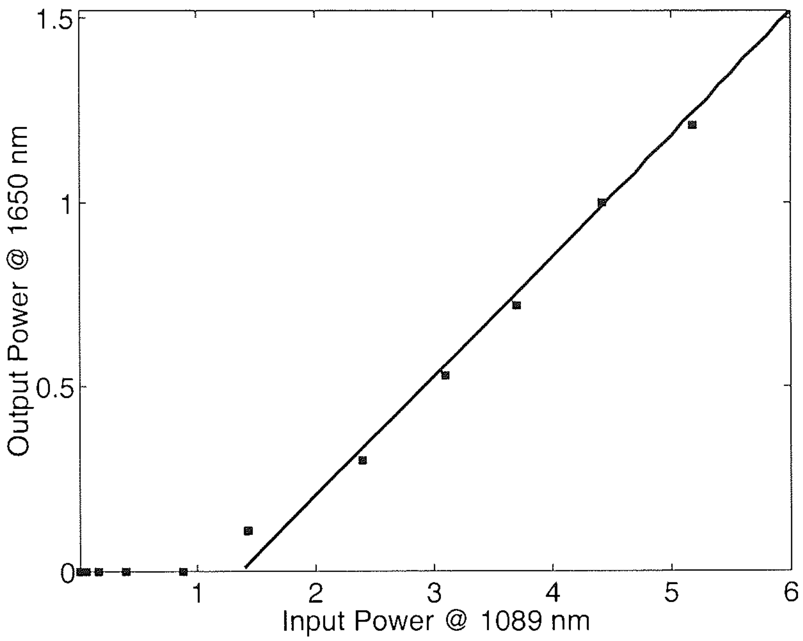

Figure 4.19: Output power of the composite RFL versus the output power of Yb-laser. Square dots represent the experimental results and the solid line is numerical prediction.

P_{in}(W)	R_{out1}(%)	R_{out2}(%)	L_1(m)	L_2(m)	η(%)
experiment	20	40	250	1000	24.00
5.0	3.9	6.5	509	1875	27.50
4.0	4.8	9.5	520	1993	24.50
3.0	5.6	15.0	538	2120	20.45
2.0	6.5	26.8	572	2260	14.27

Table 4.6: Optimal parameters of the composite RFL optimised for some input powers

Figure 4.20 illustrates the plot of output power characteristics of the composite RFLs optimised for a number of input powers. One may see that by optimising the cavity parameters, the performance of the laser can be improved. For instance, for the input power of 5 W, the output power of this laser is about 1.2 W that corresponds to the conversion efficiency of 24%, with the cavity parameters used in the experiment. However, the efficiency can be increased up to 27.5% by using an appropriate choice of the fibre lengths and coupler reflectivities.

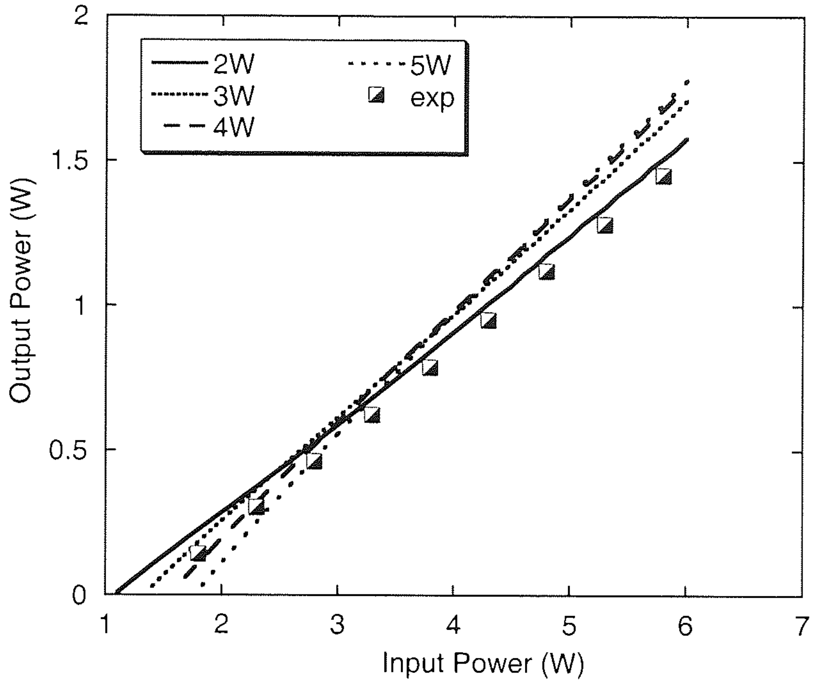

Figure 4.20: Output power characteristics of the composite RFL optimised at various input powers.

4.7 Multiple output wavelength Raman fibre laser

Multi-wavelength-pumped silica-fibre discrete Raman amplifier has become a key technology to widen the overall gain-bandwidth while simultaneously reducing its spectral non-uniformity in telecom applications. One of the major advantages comes from the fact that it can accommodate signals over a large bandwidth providing simultaneous amplification to a large number of channels in wavelength division multiplexing (WDM) systems.

Broadband Raman amplifiers exploiting 12 pump sources have been reported to achieve a gain flatness as good as 0.1 dB over the C+L bands [33]. In order to design a broadband Raman amplifier, however, one must consider a tradeoff between its advanced characteristics and its overall costs. In many applications, it is reasonable to choose moderate gain flatness over a wide spectral range using, instead, a minimal number of pump sources. Such device, obviously, would be easier to maintain and be a cost-effective solution compared to the many-pump configuration. In Ref. [62], a simple direct approach to design a flat gain Raman amplifier with a bandwidth ranged from 1520 – 1595 nm and suppressed gain ripples has been reported. Figure 4.21 illustrates the realisation of the flat-gain Raman discrete Raman amplifier backward-pumped by three wavelengths. The optimal amplifier configuration requires only three pumps at 1420 nm, 1437.2 nm and 1480 nm with the powers of 339 mW, 333 mW, and 328 mW, respectively. The gain spectrum of the discrete Raman amplifier is shown in Figure 4.22.

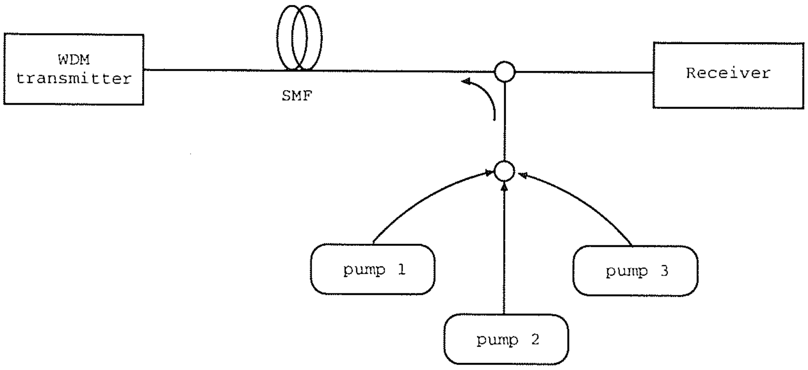

Figure 4.21: Gain-flattened three pump Raman amplifier schematic diagram.

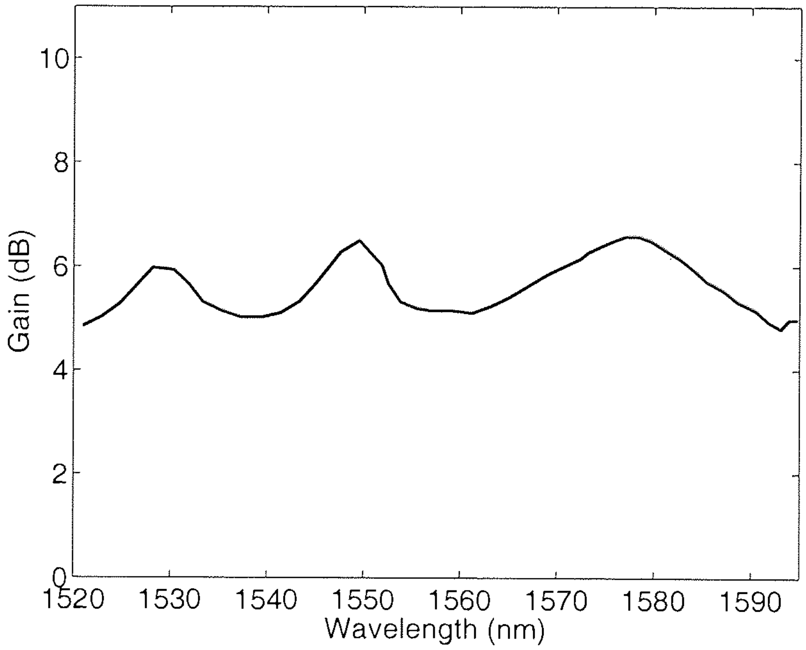

Figure 4.22: Gain spectrum of the three pump Raman amplifier.

As well as the simplicity and flexibility in operation of the broadband Raman amplifiers, a compact and efficient pump source is required. Due to its simple structure and potentially low cost, multiple output wavelength RFL pumped by the semiconductor laser is an interesting choice [63, 64].

In this section, a novel design and performance analysis of a multiple output wavelength composite RFL [65, 66] aimed to use as a pump source for the above amplifier is presented. The composite RFL is comprised with two sections. The first section employs a Phosphosilicate core fibre as its gain medium to minimise the number of stages required to reach the output wavelength that may result in a lower cost and less expensive optical scheme [57]. The second section is a RFL based on Ge-doped fibre with multiple output wavelengths. The laser performance is to be analysed by using numerical modelling techniques.

4.7.1 Laser design

Figure 4.23 illustrates the schematic diagram of the laser setup. A double cladded Yb-doped fibre laser pumped by a laser diode array at 978 nm is used as a pump source for the composite RFL. The Yb-laser provides the emission wavelength of 1080 nm. The composite RFL is comprised with two main sections. The first section converts the wavelength from 1080 nm (λ_P) to 1263 nm (λ_1). Note that the choice of the pump wavelength at 1080 nm is because it delivers the highest slope efficiency of the double-clad Yb-doped fibre laser [58]. A Phosphosilicate core fibre has been chosen to be used as a gain medium in this section because of its larger Raman shift (1330 cm^{-1} compared to 440 cm^{-1} of the Ge Raman shift) that makes a simple single stage wavelength conversion possible. The second section is a multiple output RFL based on Ge-doped fibre to provide efficient wavelength conversions from 1263 nm to 1420 nm (λ_3), 1437.2 nm (λ_4), and 1480 nm (λ_5). The nested cavities are formed by pairs of FBGs with high reflectivities except for each output coupler (R_{out1} and R_{out2}), each of which has a moderate reflectivity to couple the light out of the cavity. For the sake of simplicity, in numerical modelling works, we analyse and perform parameters optimisations for each section separately.

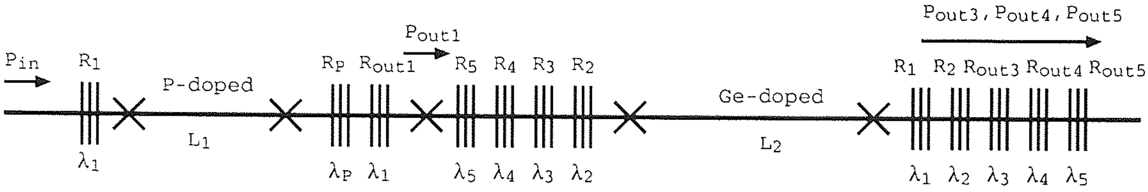

Figure 4.23: Schematic diagram of the multiple output wavelength composite Raman fibre laser.

4.7.2 Analysis and optimisation of Phosphosilicate section

In our analysis of the first section of the composite multiple output wavelength RFL, the model described in Section 4.2 has been adopted. The model must be modified to account for all interactions among the forward and backward travelling waves. The problem definition to aid the model development is shown in Figure 4.24.

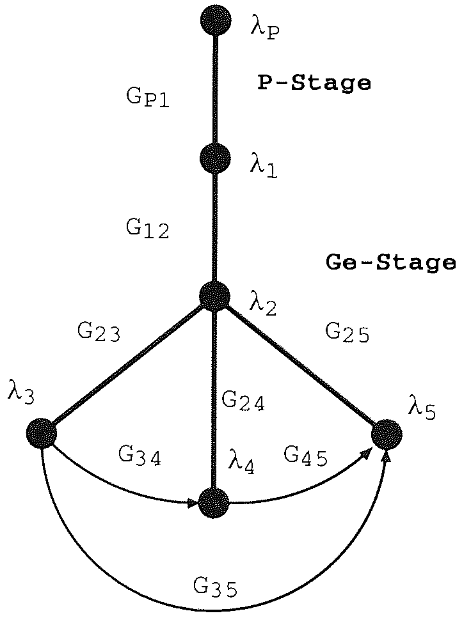

Figure 4.24: Problem definition of the multiple output wavelength composite Raman fibre laser.

The performance of a RFL depends on several parameters: reflectivity of the output coupler, cavity length and input power. The optimal output reflectivity and cavity length can be estimated by using full-scale optimisation in the parameter space for a given input power. We followed the procedure described in Section 4.3 to obtain the optimal parameters for this section. The parameters used in the simulations are summarised in Table 4.7, where G_{P1} is the abbreviated form of g_R^{P1}/A_{eff}^{P1}.

Wavelength(nm)	α (dB/km)	G_{P1} $(\mathrm{Wm})^{-1}$
$\lambda_P = 1080$	1.44	1.242×10^{-3}
$\lambda_1 = 1263$	0.87	

Table 4.7: Simulation parameters for the first section (P-doped fibre) of the multiple output wavelength composite Raman fibre laser.

Figure 4.25 depicts the contour plot of the conversion efficiency varying with the output reflectivity R_{out1} and the cavity length L_1 for some given input powers. One may see that the optimal regime exhibits a high tolerance as such the freedom in choosing the appropriate cavity parameters well away from the exact optimal values is allowed without sacrificing too much performance.

The exact optimisation results for some chosen input powers as well as the predicted conversion efficiency are given the Table 4.8. We have achieved a fairly high conversion efficiency ranged from 57.8 – 69.9% for P_{in} = 2 – 5 W. The important reason for such a high conversion efficiency is the smaller cavity loss as only one stage is required to achieve a desire converted wavelength when using the Phophosilicate gain medium.

P_{in} (W)	R_{out1} (%)	L_1 (m)	η (%)
2	31.8	490	57.8
3	22.5	437	63.9
4	16.8	399	67.5
5	13.0	373	69.9

Table 4.8: Simulation parameters for the first section (P-doped fibre) of the multiple output wavelength composite Raman fibre laser.

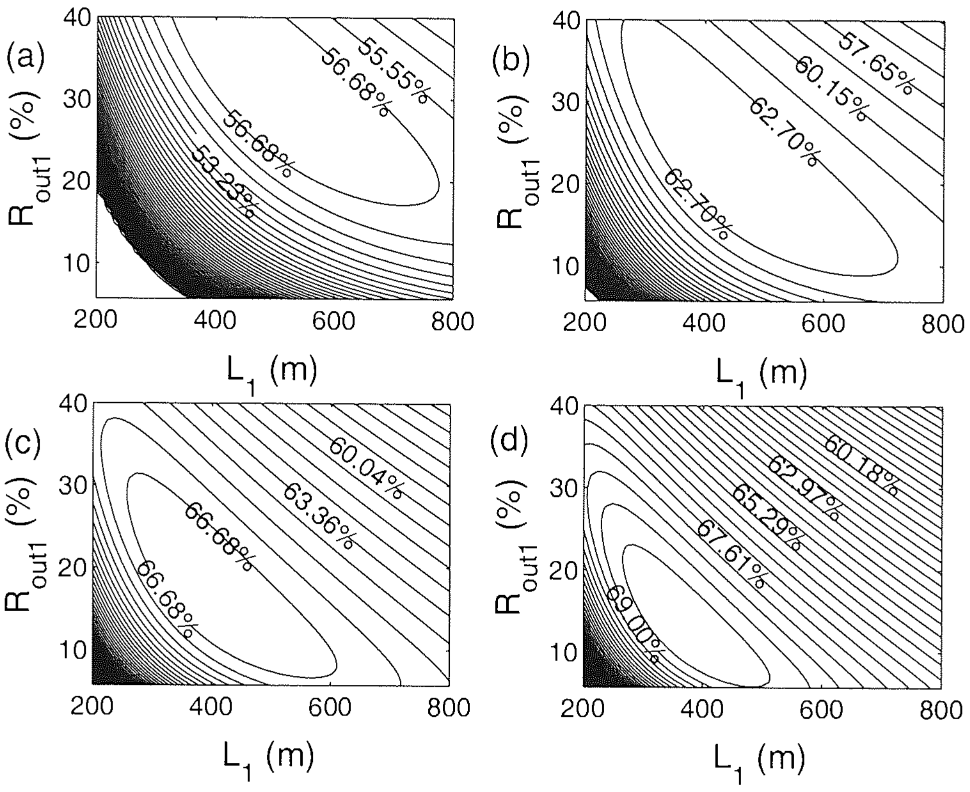

Figure 4.25: Conversion efficiency contour of the P-doped stage for a number of input powers. (a) $P_{in} = 2$ W, (b) $P_{in} = 3$ W, (c) $P_{in} = 4$ W and (d) $P_{in} = 5$ W.

4.7.3 Multiple output wavelength section: cavity modelling

In the analysis of the multiple output wavelength section, we need to account for all possible power transfers among the Stokes waves in the cavity as illustrated in Figure 4.24. The model used in the previous section is modified to suit the problem. We assume that the total power of non-zero linewidth Stokes waves is concentrated at only one wavelength. This thus leads to a simple discrete model. Under steady state conditions, the power exchange in the laser cavity can be described by the following set of ordinary differential equations (ODEs).

$$\begin{aligned}
\frac{dP_1^{\pm}}{dz} &= \mp\alpha_1 P_1^{\pm} \mp \frac{\nu_1}{\nu_2} G_{12}\left(P_2^{+} + P_2^{-} + 2n_{12}\right) P_1^{\pm}, \\
\frac{dP_2^{\pm}}{dz} &= \mp\alpha_2 P_2^{\pm} \pm G_{12}\left(P_1^{+} + P_1^{-}\right)\left(P_2^{\pm} + n_{12}\right) \mp \frac{\nu_2}{\nu_3} G_{23}\left(P_3^{+} + P_3^{-} + 2n_{23}\right) P_2^{\pm} \\
&\quad \mp \frac{\nu_2}{\nu_4} G_{24}\left(P_4^{+} + P_4^{-} + 2n_{24}\right) P_2^{\pm} \mp \frac{\nu_2}{\nu_5} G_{25}\left(P_5^{+} + P_5^{-} + 2n_{25}\right) P_2^{\pm}, \\
\frac{dP_3^{\pm}}{dz} &= \mp\alpha_3 P_3^{\pm} \pm G_{23}\left(P_2^{+} + P_2^{-}\right)\left(P_3^{\pm} + n_{23}\right) \mp \frac{\nu_3}{\nu_4} G_{34}\left(P_4^{+} + P_4^{-} + 2n_{34}\right) P_3^{\pm} \\
&\quad \mp \frac{\nu_3}{\nu_5} G_{35}\left(P_5^{+} + P_5^{-} + 2n_{35}\right) P_3^{\pm}, \\
\frac{dP_4^{\pm}}{dz} &= \mp\alpha_4 P_4^{\pm} \pm G_{24}\left(P_2^{+} + P_2^{-}\right)\left(P_4^{\pm} + n_{24}\right) \pm G_{34}\left(P_3^{+} + P_3^{-}\right)\left(P_4^{\pm} + n_{34}\right) \\
&\quad \mp \frac{\nu_4}{\nu_5} G_{45}\left(P_5^{+} + P_5^{-} + 2n_{45}\right) P_4^{\pm}, \\
\frac{dP_5^{\pm}}{dz} &= \mp\alpha_5 P_5^{\pm} \pm G_{25}\left(P_2^{+} + P_2^{-}\right)\left(P_5^{\pm} + n_{25}\right) \pm G_{35}\left(P_3^{+} + P_3^{-}\right)\left(P_5^{\pm} + n_{35}\right) \\
&\quad \pm G_{45}\left(P_4^{+} + P_4^{-}\right)\left(P_5^{\pm} + n_{45}\right),
\end{aligned} \tag{4.7}$$

where

$$n_{ab} = 2h\nu\Delta\nu\left(1 + \frac{1}{e^{h(\nu_a - \nu_b)/kT} - 1}\right). \tag{4.8}$$

P_j^{+} and P_j^{-} are the powers of forward and backward propagating waves at wavelength j-th, respectively. α_j and ν_j are the attenuation and frequency at wavelength j-th. G_{jk} is the gain coefficient for stimulated Raman scattering from the j-th to k-th lines. n_{ab} is a spontaneous Raman scattering noise term, where h and k are Plank's and Boltzmann's constants, respectively. T is the ambient temperature.

The main purpose of incorporating the spontaneous noise term is to ensure the stability of the numerical scheme and avoid the trivial solution in which the pump is depleted only by the linear absorption without generating any Stokes power. The parameters used in the simulation are summarised in Table 4.9 and 4.10.

To solve the above system of ODEs, a set of boundary conditions is required. As usual, the boundary conditions are given by the reflection at each FBG and the

Wavelength (nm)	α (dB/km)
$\lambda_1 = 1263$	1.44
$\lambda_2 = 1337$	1.52
$\lambda_3 = 1420$	2.09
$\lambda_4 = 1437$	1.60
$\lambda_5 = 1480$	0.76

Table 4.9: Attenuation parameters used in the simulation of the second section (Ge-doped fibre) of the multiple output wavelength composite Raman fibre laser.

Parameters	Gain coefficient ($\times 10^{-3}$ (Wm)$^{-1}$)
G_{12}	4.190
G_{23}	3.789
G_{24}	2.144
G_{25}	0.354
G_{34}	0.813
G_{35}	1.763
G_{45}	2.144

Table 4.10: Raman gain coefficients used in the simulation of the second section (Ge-doped fibre) of the multiple output wavelength composite Raman fibre laser.

injected pump power, thus

$$\begin{aligned}
P_1^+(L_1) &= P_{in2} = P_{out1}, \\
P_j^+(L_1) &= P_j^-(L_1) \cdot R_j, \qquad j = 2, \ldots, 5 \\
P_j^-(L_2) &= P_j^+(L_2) \cdot R_j, \qquad j = 1, 2 \\
P_j^-(L_1) &= P_j^+(L_2) \cdot R_{out,j}, \qquad j = 3, 4, 5
\end{aligned} \tag{4.9}$$

where R_j and $R_{out,j}$ denote the reflectivities of the FBGs forming the cavity and the output couplers, respectively. The output power at wavelength j-th can be obtained by

$$P_{out,j} = P_j^+(L_2) - P_j^-(L_2) = P_j^+(L_2)(1 - R_{out,j}). \tag{4.10}$$

In our simulations, Bragg reflectors with 99% reflectivities except for the output couplers are considered.

The characteristics of the multiple output RFL can be studied by solving the above model. We used a simple and straight forward shooting algorithm to solve the BVPs. However, to achieve a desired power partitioning of all outputs, one may need to adjust the output coupler reflectivities (R_{out3}, R_{out4} and R_{out5}) and the power launched into the section (P_{out1}). The adjustment, nonetheless, is not straightforward due to the nonlinear nature of the process. A simple down hill simplex algorithm can be used to find an appropriate combination of output reflectivities and input power yielding a desired power partition.

4.7.4 Cavity optimisation

To achieve the highest performance of the laser, one may wish to optimise the cavity parameters. As mentioned in the previous section, however, that the output reflectivities and the power launched into the cavity must be fixed to a correct combination to yield a desired power partition. Only degree of freedom, in which we are able to optimise, is the cavity length. We performed a search for an optimal cavity length, which gives the highest conversion efficiency. In this case, the cavity is optimised for the power partition of 339 mW, 333 mW and 328 mW at 1420 nm, 1437.2 nm and 1480 nm, respectively. This is the optimal power partition required for the flat gain 3-wavelength pumped Raman amplifier with 70 nm bandwidth demonstrated in Ref. [62] explained earlier. Figure 4.26 shows a variation of the conversion efficiency with the cavity length. The degradation of the conversion efficiency when the cavity is too short is due to the fact that there is not enough cavity length to allow an efficient power transfer among the Stokes wave. For a too long cavity, the cavity loss will play a critical role to degrade the conversion performance. The highest conversion efficiency of 41.9% is achieved at $L_2 = 380$ m with the appropriate combination of R_{out3}, R_{out4} and R_{out5} are 51%, 35% and 28%, respectively. This leads to the multiple wavelength composite RFL total conversion efficiency of approximately 28%. One may also find in Figure 4.26 that the laser exhibits a rather high tolerance against the deviation of the cavity length. The conversion efficiency is degraded by less than 1.5% when the cavity length deviates from the optimal value for ±100 m. This evidently shows a high tolerance of the optimal regime. Again, overestimate of the cavity length does less harm to the laser performance and the conversion efficiency, which in this case degrades only a little beyond the optimal value.

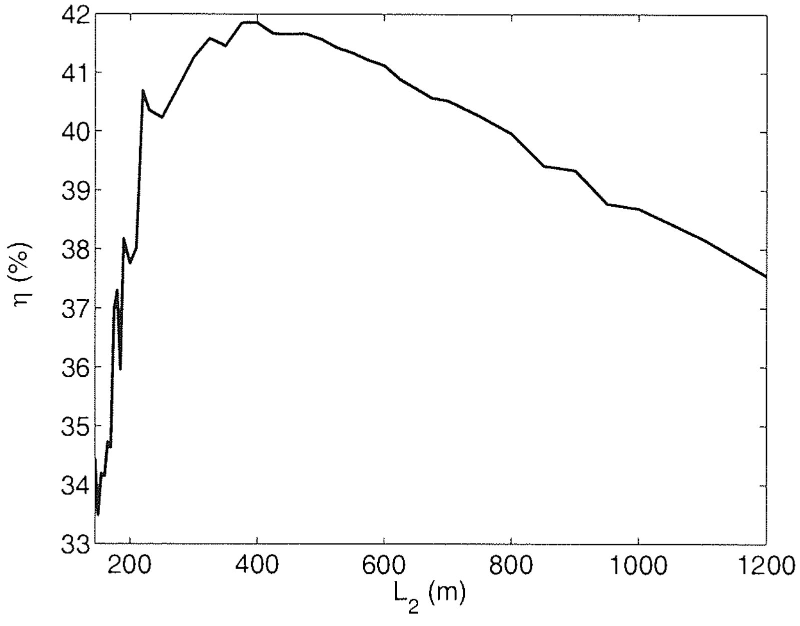

Figure 4.26: Conversion efficiency of the multiple output wavelength stage as a function of its cavity length.

4.7.5 Characteristics of the optimal regime

In a practical use of the laser, the partition setting may be required to change. One may be interested to know how the conversion efficiency varies with the partition setting. We thus investigated the variation of the conversion efficiency at various power partition settings.

Figure 4.27(a) illustrates the variation of the conversion efficiency when fixing P_{out5} to its optimal value and varying P_{out3} and P_{out4}. Note that the total output power (P_{out3}+P_{out4}+P_{out5}) is maintained to 1 W constant in all cases. The conversion efficiency varies almost monotonically with the adjustment of P_{out3} and is in the range of 38 – 48%. Similarly, Figure 4.27(b) depicts the variation of the conversion efficiency when fixing P_{out4} and varying the rest but still maintaining the total output power of 1 W. The conversion efficiency still varies in the range of 35 – 47%. Last, we fixed P_{out3} and varied the rest. The result is shown in Figure 4.27(c). In this case,

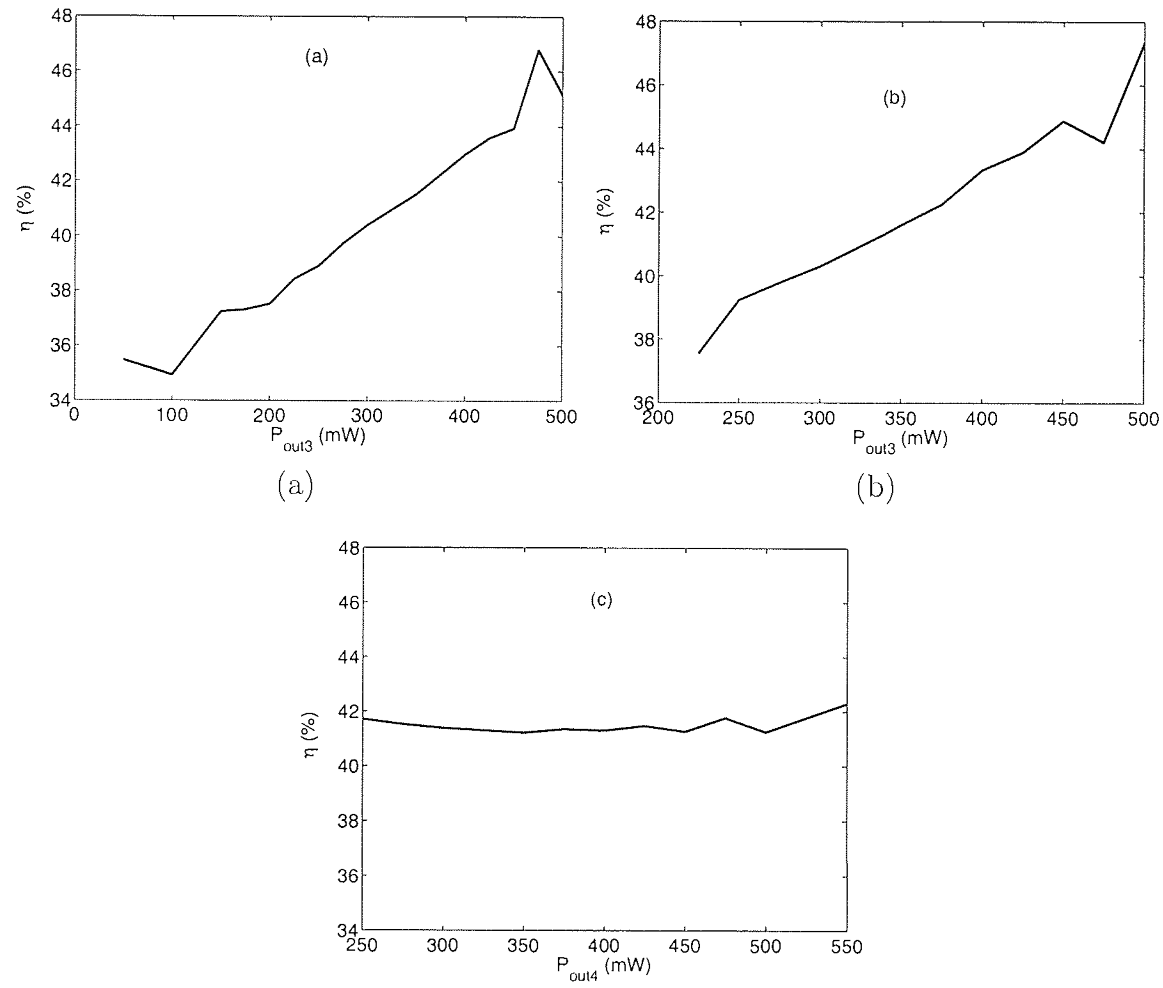

(a) (b)

(c)

Figure 4.27: Variation of conversion efficiency against the deviation of output powers from their optimal settings. (a) Fixed P_{out5} (b) Fixed P_{out4} (c) Fixed P_{out3}.

the conversion efficiency is nearly constant and takes the value of approximately 42%. This observation can be described easily by considering the fact that the longer wavelength outputs rely partly on the power transfer from P_{out3}, and thus is sensitive to the variation of P_{out3}. Nonetheless, Figure 4.27(c) still confirms the high tolerance of the optimal regime if P_{out3} is fixed. This fact is beneficial from the engineering point of view, where a freedom and convenience in designing the laser is of importance.

To emphasise on the tolerance of the optimal regime, we performed a number of cavity optimisations for various power partition settings. By fixing P_{out3} and the total output power, we define ΔP as a power adjustment variable such that

$$P'_{out3} = P_{out3,opt} \qquad P'_{out4} = P_{out4,opt} + \Delta P \qquad P'_{out5} = P_{out5,opt} - \Delta P, \tag{4.11}$$

where $P_{out3,opt}$, $P_{out4,opt}$ and $P_{out5,opt}$ are the power partition setting used in the optimisation described earlier. Figure 4.28 shows that the optimal cavity length varies in the range of 25 m. Considering this fact, an optimal design for a typical power partition setting should warrant a good performance at other partition setting as well.

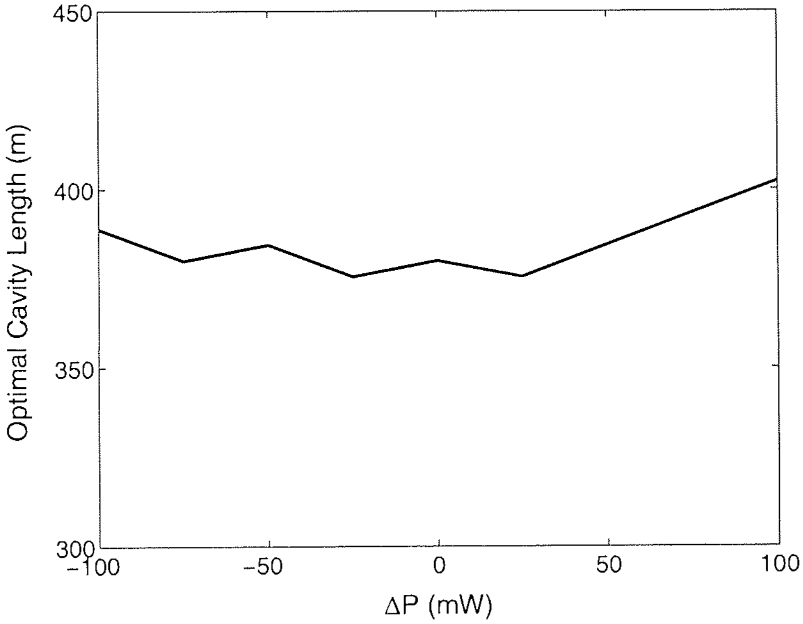

Figure 4.28: Optimal cavity length for various power partition settings.

4.8 Conclusions

Raman fibre lasers (RFLs) have drawn a considerable attention not only in the areas of optical communication, but also in other areas such as medicine, biomedical engineering, environmental science, etc. The main advantage of exploiting stimulated Raman scattering (SRS) process in the fibre laser technology is the freedom it offers in operating at an extremely wide range of wavelengths. A cascade of wavelength conversion in combination with the employment of both Ge- and P-Raman shifts allows one to design a RFL to operate at any wavelength in the range of $1.1-1.7$ μm, in which some part of the spectral region may not be accessible by other types of fibre lasers.

This chapter has provided a discussion on the principle, design, analysis and optimisation of various types of RFLs, specifically focussing on the type that the resonated cavities are built from fibre Bragg gratings (FBGs). A numerical model developed in Chapter 3 has been applied to analyse the characteristics of the RFLs using realistic parameters. The model has been verified by comparing the numerical prediction with the experimental results. Good agreements have been observed.

In Section 4.4, a two stage RFL was presented. The laser cavity is based on a Phosphosilicate core fibre, which makes possible a wavelength conversion from 1061 nm to 1480 nm by using only two stages of conversion. The key technology is the use of P_2O_5-Raman shift of $\sim$ 1330 cm^{-1} that is nearly three times larger than that of the SiO_2/GeO_2 Raman shift. The cavity of the RFL has been optimised to ensure the highest performance. Using the conversion efficiency as a figure of merit, the cavity parameters namely the output coupler reflectivity R_{out} and the cavity length (L) were optimised for a number of input powers. Apart from a full scale optimisation in the key parameter space, the optimal parameters can also be deduced from a graphical methods presented in the section, which offers a convenient and reliable way to design a cavity. The high tolerance of the optimal regime has been presented. This also allows more freedom and easy way in designing the laser.

We also investigated the slope efficiency spectra of various RFLs pumped by a double-cladded Yb-doped fibre laser. The result shows that the total efficiency spectrum depends mainly on the efficiency spectrum of the Yb-laser. Thus taking into account the Yb-laser efficiency spectrum, we showed that the emitting wavelength ranged from $1.4-1.6$ μm can be covered by using both Germanosilicate and Phophosilicate core fibre as the gain media.

The radiation wavelength at or beyond 1.6 μm is, however, possible by exploiting a composite RFL that includes a concatenation of P- and Ge-doped based RFL sections. The composite RFL may be configured to provide the radiation spectrum in the range of $1.6-1.75$ μm, which is not possible for typical rare-earth doped fibre lasers. The detailed analysis and design have been given in Section 4.6.

Finally, we extended our study towards a design and analysis of multiple output wavelength composite RFL. The novel design may be used to pump a flat gain Raman amplifiers in telecom applications. The multiple output wavelength composite RFL is comprised with two sections *i.e.* a single stage P-doped RFL and a multiple output wavelength RFL based on Ge-doped fibre. The use of Phosphosilicate core fibre offers a reduction in the number of stages needed, and hence results in a more stable and potentially lower cost. The cavity optimisation has been presented to ensure the high performance of the laser. The overall conversion efficiency of 28% was predicted for this device. We also investigated the characteristics of the optimal regime. We found that the laser conversion efficiency is more sensitive to the power adjustment of the shortest output wavelength due to cascading effect. However, the optimal regime is rather tolerant to the deviation of parameters from their optimal values.

Chapter 5

Modelling of Raman amplification in optical transmission systems

5.1 Introduction

Dramatic growth of demands in higher quality and endless capacity in communications has stimulated research and development of optical communication systems with continuously increasing data rate every year. Many new technologies have been adopted to keep pace with the exponentially growing demand. Raman amplification is one of the most interesting solutions that provides a break through in the development of optical communication systems. There are three main schemes of Raman amplifiers widely used nowadays. The first one is a discrete or lumped Raman amplifier pumped by a multiple wavelength laser sources. This solution offers a large gain bandwidth with minimal gain ripples [32] as well as the low noise characteristic of Raman amplifiers. The use of Raman effect also provides an extension of the gain spectrum into a new band inaccessible by other means of amplification such as the low loss S and S^+ bands [34].

The second potential solution is the distributed Raman amplifier (DRA). In this scheme, the pump power is extended into the transmission line fibre providing a gain to compensate for the fibre loss. As discussed in Chapter 3, the distributed nature of the amplifier helps to improve the optical signal to noise ratio (OSNR). Using this scheme, the nonlinearity is also reduced as a result of the fact that a lower signal power is required to maintain a desired OSNR. However, the long effective length of the DRA imposes itself to a higher double Rayleigh back scattering (DRS) noise. This trade-off thus inspires the third scheme in which the DRA is used as a low noise preamplifier. Part of the loss is compensated for by a high gain EDFA. Using a combination of both DRA and EDFA, the scheme is thus referred to as hybrid amplification scheme.

In the research and development of the above schemes involving an optimisation of a large number of parameters, the old-fashioned experimental-based approach may end up with a huge amount of time consumption and more importantly an extremely expensive cost. However, the systems are too complex and can no longer be analysed or evaluated adequately by an analytical approach. Therefore, the numerical modelling approach seems to be an appropriate choice to aid the design and analysis of the systems.

In the development of high cost optical communication systems, a highly accurate model is essential to provide a reliable and trustable results before the expensive experiments or implementations are to be carried out. Nevertheless, the trade-off between the accuracy and computation time has to be taken into account. In this chapter, we describe an effective approach to model the Raman amplified optical transmission systems. The approach consists of a combination of deterministic signal power analysis in the frequency domain to determine the signal evolution under the effect of Raman amplification and the transient model simulation including the random signal to account for other linear and nonlinear dynamics. This approach provides a realistic and practical solution in terms of CPU times and resources to simulate the Raman amplified transmission systems.

5.2 Generalised Raman amplified gain model

In this section, the power balance model described in Chapter 3 will be extended to analyse the deterministic power signals in a considered frequency window, which in practice, must be wide enough to cover all pumps and signal channels. The window is to be divided into a series of small signal and noise bins whose width is carefully chosen. In our approach, we assume that each signal channel should be confined within a signal bin making each deterministic power signal represent an average power of the signal in each channel. As a rule of thumb, the width of the bin $\Delta\nu$ may be set to the same value as the channel spacing of the signals in wavelength division multiplexing (WDM) systems. For example, the bin width $\Delta\nu$ may be set to 100 GHz when considering a typical 40 Gb/s WDM system with 100 GHz channel spacing. As a result, the analysis of pump and signal interactions by using a full frequency power balance model will give a hint on noise and signal evolution within the Raman amplified transmission fibre. Figure 5.1 depicts a deterministic representation of pumps, signals and noises component within a considered frequency window.

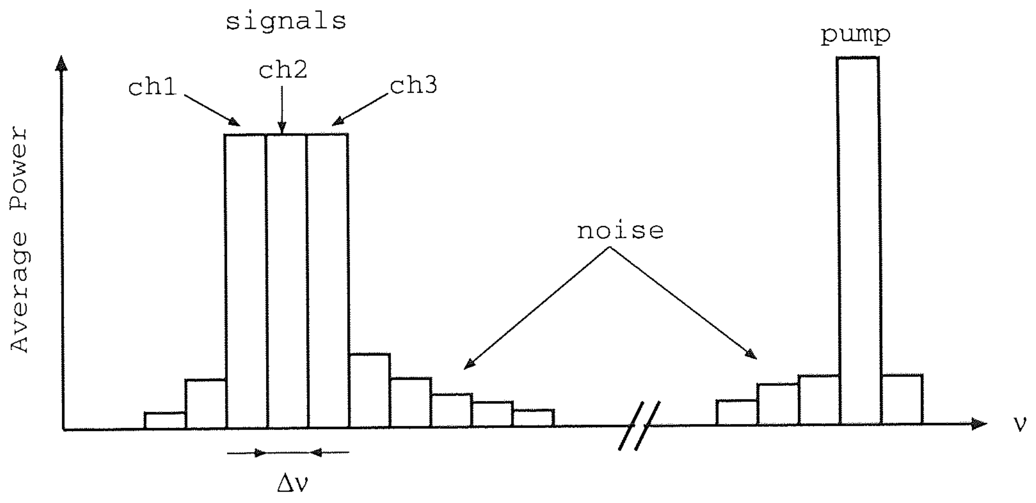

Figure 5.1: Deterministic power signals and pumps in a considered frequency window.

To ensure the accuracy of the model, all important physical effects must be included. In Raman amplification, the following known effects are of importance:

- amplified spontaneous noise due to the spontaneous Raman scattering and its temperature dependence;
- double Rayleigh back scattering (DRS);

- the energy transfer via stimulated Raman scattering (SRS);
- arbitrary interaction between pump–signal, pump–pump, signal–signal including noises;
- higher order Stokes generation;
- effect of other discontinuity such as splicing and spot size mismatch losses within the span.

5.2.1 Full frequency power balance model

Having taken into account all of the effects in the previous section, the power transfer between different spectral components can be described through a modified power balance model as

$$\begin{aligned}\frac{dP_\nu^\pm}{dz} &= \mp\alpha_\nu P_\nu^\pm \pm \epsilon_\nu P_\nu^\mp \pm \sum_{\mu>\nu} \frac{g_{\mu\nu}}{A_{\mu\nu}} \left(P_\mu^+ + P_\mu^-\right) P_\nu^\pm \\ &\mp \sum_{\mu<\nu} \frac{\nu}{\mu}\frac{g_{\nu\mu}}{A_{\nu\mu}} \left(P_\mu^+ + P_\mu^-\right) P_\nu^\pm \\ &\mp 4h\nu \sum_{\mu<\nu} \frac{g_{\nu\mu}}{A_{\nu\mu}} \left(1 + \frac{1}{e^{h(\nu-\mu)/kT} - 1}\right) \Delta\mu P_\nu^\pm \\ &\pm 2h\nu\Delta\nu \sum_{\mu>\nu} \frac{g_{\mu\nu}}{A_{\mu\nu}} \left(P_\mu^+ + P_\mu^-\right) \left(1 + \frac{1}{e^{h(\mu-\nu)/kT} - 1}\right), \qquad (5.1)\end{aligned}$$

where $P_\nu^\pm$ represents the forward propagating (+) and backward propagating (−) average power signals within the frequency interval $\Delta\nu$ centred at frequency ν. α_ν and ϵ_ν are corresponding fibre attenuation and Rayleigh scattering coefficients. The Raman gain coefficient governing the power transfer from the signal at frequency μ to ν is denoted by $g_{\mu\nu}$ in connection with its corresponding effective area $A_{\mu\nu}$.

In this representation of signals in the form of the average powers, there is no distinction between the signals and noises. It is, however, possible to artificially isolate the contribution of the noises by following the procedure similar to the one described in Section 3.5 for the purpose of analysing the OSNR.

In order to solve Eq. (5.1), one needs to know the initial value of all signals and noises at the launch position. Each noise component in the forward direction may be assumed to have a zero initial value. However, this is not always the case for the backward propagating noise, especially in the case of backward pumping, in which the backward propagating noise is continuously amplified by the pump.

To alleviate this problem, an iterative approach may be used to find the right initial value of each backward propagating noise. The procedure begins by propagating the signals and noises with known initial conditions from the begin ($z = 0$) to the end ($z = L$) of the fibre, and neglecting all counter-propagating noises and DRS contributions. The initial values at $z = 0$ of the co-propagating noises should be set to zero. Once the propagation is done, we should have the amplified signals and values for the co-propagating noises in the absence of its counter-propagating counterparts at the end ($z = L$) of the fibre. The values can now be used as the guessed initials for the reversed pass. The counter-propagating noises should be enabled when propagating this pass (from $z = L$ to $z = 0$). Another forward propagation from $z = 0$ to $z = L$ with all noise contributions enabled is subsequently needed to complete the procedure. This procedure may be repeated several times to improve the accuracy. Figure 5.2 illustrates the forward propagating power signal evolution of the backward pumped DRA system with 100 km pumping span. The signals consist of 4 channels with 100 GHz spacing. The correct backward pump power has been found by using the shooting algorithm aiming to fully recover the power of the middle channel (channel 3). The details of the signals in each direction at both ends of the fibre are shown in Figure 5.3.

5.2.2 Effective attenuation

From Eq. (5.1), it is possible to separate the factor governing power evolution and noise contributions such that [67]

$$\frac{dP_\nu^+}{dz} = -\alpha_\nu^{eff} P_\nu^+ + \Pi_\nu^R + \Pi_\nu^S, \tag{5.2}$$

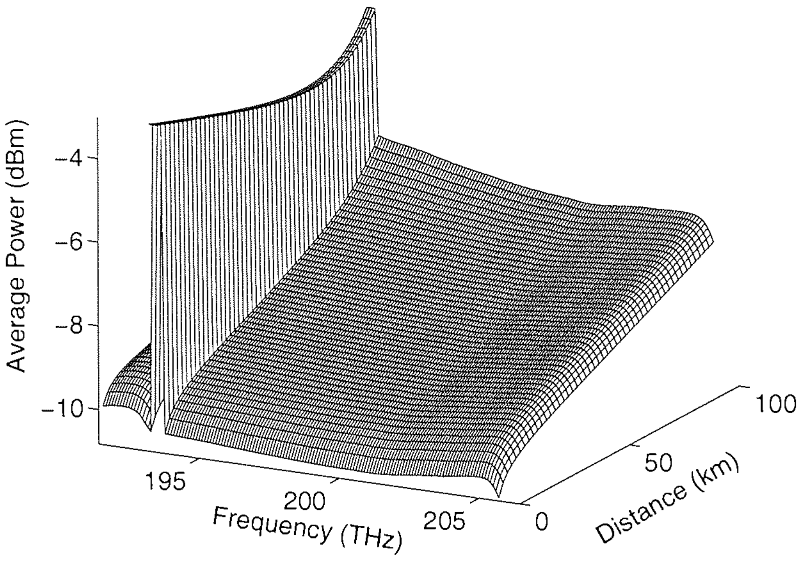

Figure 5.2: Forward propagating power signal evolution of a Raman amplified 4–ch WDM system with a backward pump.

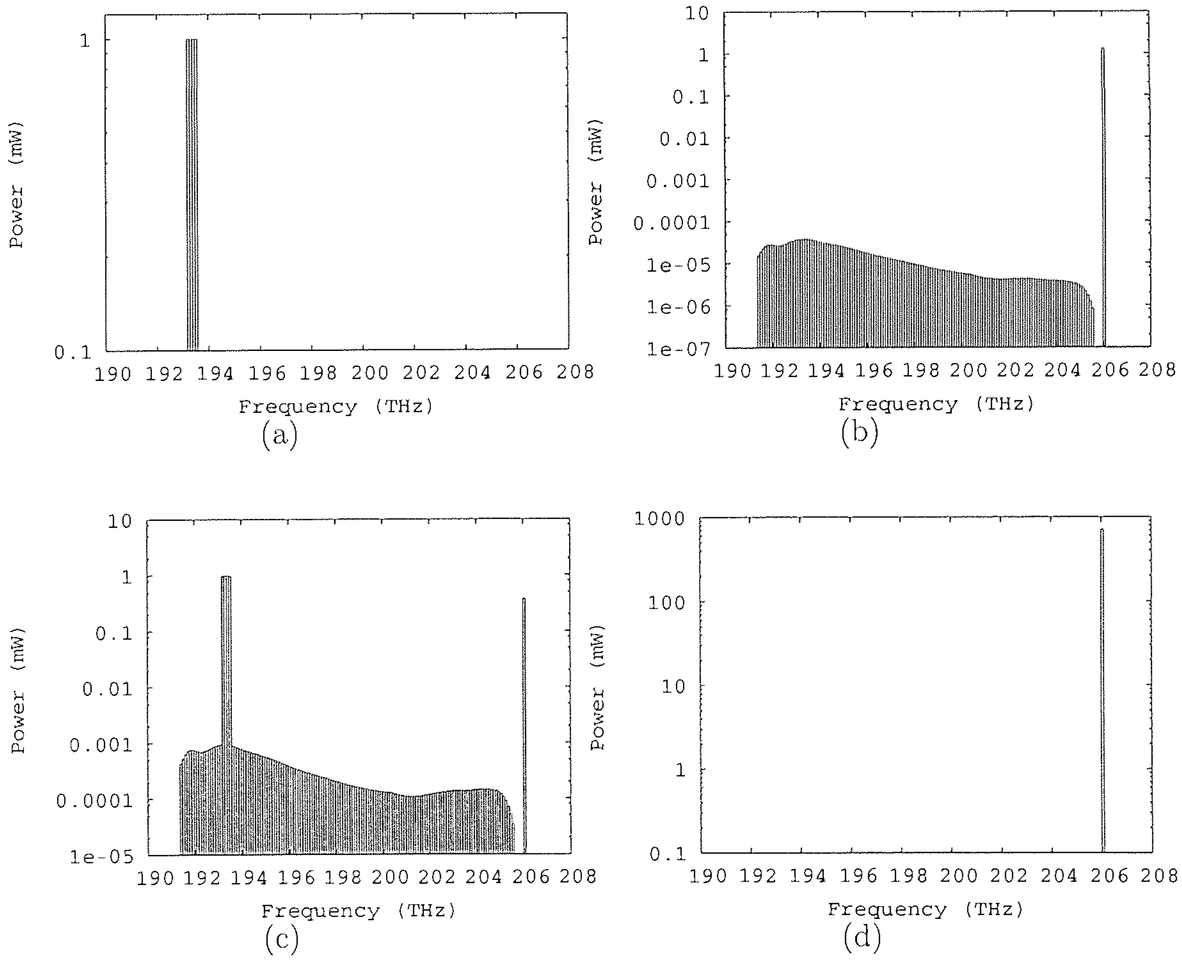

(a) (b) (c) (d)

Figure 5.3: Power spectra (a) forward propagation at $z = 0$ km (b) backward propagation at $z = 0$ km (c) forward propagation at $z = 100$ km (d) backward propagation at $z = 100$ km.

where

$$
\begin{aligned}
\alpha_\nu^{eff} &= \alpha_\nu - \sum_{\mu>\nu} \frac{g_{\mu\nu}}{A_{\mu\nu}} \left(P_\mu^+ + P_\mu^-\right) + \sum_{\mu<\nu} \frac{\nu}{\mu} \frac{g_{\nu\mu}}{A_{\nu\mu}} \left(P_\mu^+ + P_\mu^-\right) \\
&\quad +4h\nu \sum_{\mu<\nu} \frac{g_{\nu\mu}}{A_{\nu\mu}} \left(1 + \frac{1}{e^{h(\nu-\mu)/kT} - 1}\right) \Delta\mu, \qquad (5.3) \\
\Pi_\nu^R &= \epsilon_\nu P_\nu^-, \qquad (5.4) \\
\Pi_\nu^S &= 2h\nu\Delta\nu \sum_{\mu>\nu} \frac{g_{\mu\nu}}{A_{\mu\nu}} \left(P_\mu^+ + P_\mu^-\right) \left(1 + \frac{1}{e^{h(\mu-\nu)/kT} - 1}\right). \qquad (5.5)
\end{aligned}
$$

For later incorporation of the results into a full propagation simulation, we are interested only in the forward propagating components. The effective attenuation α_ν^{eff} is the factor governing the power evolution of the spectral component at frequency ν under the Raman amplification process. Π_ν^R and Π_ν^S are the contributions from the DRS and amplified spontaneous emission (ASE) noises, respectively. P_ν^+ represents the average power at frequency ν over the bandwidth $\Delta\nu$. The forward and backward directions are indicated by the $+$ and $-$ signs, respectively. ϵ_ν and α_ν are the Rayleigh scattering coefficient and fibre attenuation at frequency ν, where h and k are Planck's and Boltzmann's constants.

By numerically solving Eq. (5.1), the effective attenuation α_ν^{eff}, DRS contribution Π_ν^R and ASE noise Π_ν^S, can be obtained. The parameters provide a description of the signal power evolution as well as the noise characteristics of the Raman amplified systems. They can then be incorporated into the full propagation model to simulate the transmission systems taking into account other linear and nonlinear effects. Figure 5.4 shows an example plot of the effective attenuation obtained by solving Eq. (5.1) for a backward pumped DRA with a span of 100 km. We can see from the figure that the effective attenuation includes both gain (negative attenuation) and loss (positive attenuation) of the Raman amplified transmission line in a range of considered frequency window.

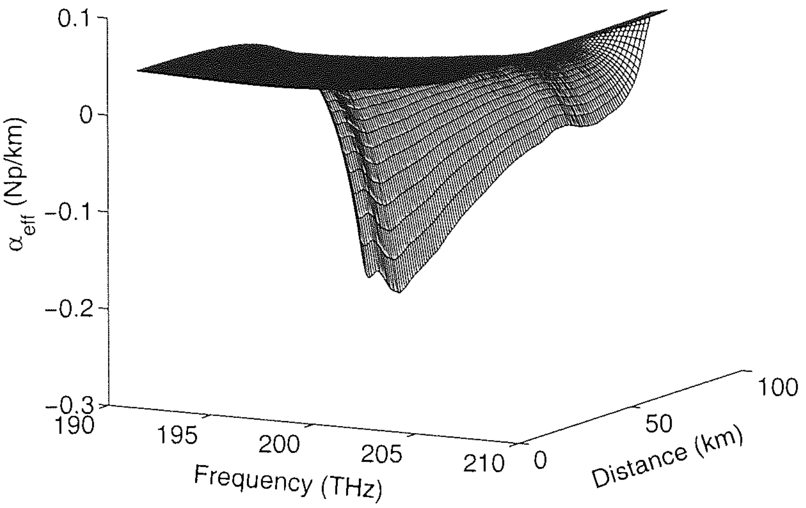

Figure 5.4: Example of the effective attenuation.

5.3 Direct numerical simulation model of the Raman amplified transmission system

The deterministic signal analysis described in the previous section provides the information about signal and noise evolutions considering only the contributions from solely Raman effect. In the high speed optical transmission systems, other effects such as group velocity dispersion (GVD), higher order dispersion and nonlinearity must be considered to enhance the accuracy and validity of the simulation approach. This section describes a direct numerical approach to predict the signal dynamic by incorporating the signal and noise power evolution information preliminarily obtained from the generalised Raman amplified gain model and other important effects.

The full direct numerical model is based on the nonlinear Schrödinger equation described in Section 2.3 and Appendix B. The incorporation of the information from the generalised Raman amplified gain model will be described.

5.3.1 Incorporation of the generalised Raman gain into the nonlinear Schrödinger equation

In the representation of Raman effect in the generalised Raman amplified gain model, the interchannel Raman amplified gain is described through the effective attenuation $\alpha_{eff}(\nu, z)$ at each frequency bin ν and position z obtained by solving the full frequency power balance model described in Section 5.2.1. The effective attenuation contains the information of signal evolutions at each frequency on the account of Raman amplification among the pumps and signals. Therefore, the Raman amplified gain can be included into the nonlinear Schrödinger (NLS) equation by replacing the regular attenuation coefficient α in Eq. (2.40) with the effective attenuation α_{eff}. The NLS equation with effective attenuation thus takes the form

$$i\frac{\partial Q}{\partial z} - \frac{k_0''}{2}\frac{\partial^2 Q}{\partial \tau^2} - i\frac{k_0'''}{6}\frac{\partial^3 Q}{\partial \tau^3} + \frac{2\pi}{\lambda_0}\frac{n_2}{A_{eff}}|Q|^2 Q = -i\frac{\alpha_{eff}}{2}Q, \tag{5.6}$$

where $Q(z, \tau)$ is the slowly varying envelope of the signal. k_0'' and k_0''' are the GVD and higher order dispersion at the signal wavelength λ_0, respectively. n_2 is the nonlinear refractive index presented in connection with the effective core area A_{eff}.

5.3.2 Normalisation of the nonlinear Schrödinger equation

In order to maintain a high computational accuracy, the NLS equation should be presented in a normalised form. We hence introduce the normalised quantities

$$q = \frac{Q}{\sqrt{P_{norm}}}, \qquad Z = \frac{z}{z_{norm}}, \qquad T = \frac{\tau}{t_{norm}}, \tag{5.7}$$

where P_{norm}, z_{norm} and t_{norm} are normalising parameters for the power, distance and time, respectively. Thus Eq. (5.6) takes the normalised form as

$$i\frac{\partial q}{\partial Z} - \frac{1}{2}\frac{k''}{|k_0''|}\frac{\partial^2 q}{\partial T^2} - \frac{i}{6}\frac{k'''}{|k_0'''|}\frac{\partial^3 q}{\partial T^3} + \frac{2\pi}{\lambda_0}\frac{n_2}{A_{eff}}P_{norm}z_{norm}|q|^2 q = -i\frac{\alpha_{eff}}{2}z_{norm}q, \tag{5.8}$$

where

$$|k_0''| = \frac{t_{norm}^2}{z_{norm}} \quad \text{and} \quad |k_0'''| = \frac{t_{norm}^3}{z_{norm}}. \tag{5.9}$$

For the sake of simplicity, we define a normalised local dispersion parameter

$$d(Z) = -\frac{k''}{|k_0''|}, \tag{5.10}$$

and the local normalised higher order dispersion parameter

$$d_3(Z) = -\frac{k'''}{|k_0'''|}. \tag{5.11}$$

It is common in the context of optical fibre engineering to use the dispersion parameter D in place of k''. Using Eq. (2.10), $d(Z)$ is related to the dispersion parameter by

$$d(Z) = \frac{D[s/m^2]\lambda^2[m^2]z_{norm}[m]}{2\pi c[m/s]\ t_{norm}^2[s^2]}. \tag{5.12}$$

Similarly, by using Eq. (2.55), the relation between the normalised higher order dispersion and the dispersion slope in the real world unit is as follow:

$$d_3(Z) = -\frac{\left(D_\lambda[s/m^3]\lambda[m] + 2D[s/m^3]\right)\lambda^3[m^3]z_{norm}[m]}{(2\pi c)^2[m^2/s^2]t_{norm}^3[s^3]}. \tag{5.13}$$

Therefore Eq. (5.8) will take a compact form as

$$i\frac{\partial q}{\partial Z} + \frac{d(Z)}{2}\frac{\partial^2 q}{\partial T^2} + i\frac{d_3(Z)}{6}\frac{\partial^3 q}{\partial T^3} + s(Z)|q|^2 q = -i\frac{\Gamma^{eff}}{2}q, \tag{5.14}$$

where

$$s(Z) = \frac{2\pi}{\lambda_0}\frac{n_2}{A_{eff}}P_{norm}z_{norm} \quad \text{and} \quad \Gamma_{eff} = \alpha_{eff}z_{norm}. \tag{5.15}$$

Eq. (5.14) is now in a ready form to be solved by using the split-step Fourier method, the details of which is described in Appendix B.

5.3.3 Noises in Raman amplified transmission line

For the correct analysis of the Raman amplified transmission systems, the noises in the amplification process must be taken into account. As previously discussed in Section 3.5, the noises in Raman amplification process are originated from two important sources: amplified spontaneous emission (ASE) and double Rayleigh scattering (DRS). It is a common practice to assume that the ASE noise can be represented by a random variable with Gaussian deviate. In other words, the ASE noise can be modelled by using the additive Gaussian white noise (AGWN). Unfortunately, less is known about the statistical property of the noise originated from the DRS. Taking into account the random Rayleigh scattering of photons, we assume that the DRS noise also follows the Gaussian statistics and can be represented by the AGWN.

Refer to Eq. (5.2), the additive noise power of each type of noise for each distance increment in the distributed Raman amplified transmission systems can be described as

$$\delta P_\nu = \Pi_\nu \; \delta z, \tag{5.16}$$

where δP_ν is the additive noise power with in the frequency bin ν for a distance increment of δz. Π_ν is the noise contribution described in Eq. (5.2). Thus the spectral density increment is

$$\delta S(\nu) = \frac{\delta P_\nu}{\Delta\nu} = \frac{\Pi_\nu}{\Delta\nu}\delta z, \tag{5.17}$$

where $\Delta\nu$ is the frequency bin spectral width.

An attempt has to be made to relate the additive noise power to the random noise property to be implemented in direct numerical simulation. We now define a complex random variable $U(\Omega)$ to represent random noise in frequency domain. Note that a random noise is characterised by its probability distribution function (PDF) and its autocorrelation property. As mentioned earlier, our noise is assumed to have the Gaussian PDF with zero mean. In accordance with our statistical assumption, the noise spectrum satisfies the following relations [68]:

$$\begin{aligned} < U(\Omega) > &= 0, & (5.18)\\ < U(\Omega)\; U(\Omega') > &= 0, & (5.19)\\ < U(\Omega)\; U^*(\Omega') > &= \delta S\; \delta(\Omega - \Omega'), & (5.20) \end{aligned}$$

where $< \cdot >$ denotes an ensemble average and $\delta(\Omega - \Omega')$ is Dirac's delta function. Eq. (5.20) indicates that the autocorrelation of a random noise should be equal to a delta function, which suggests the infinitesimal size of signal samples, or in other words, a continuous signal. However, this is not possible in the practical representation of signals by their samples in the numerical simulations that we generally regard $U(\Omega)$ for the noise field as a piecewise function of Ω as depicted in Figure 5.5.

Note that the values of different pieces must be uncorrelated to satisfy Eq. (5.20). Suppose that the variance of each piece is σ^2, the autocorrelation of the piecewise noise field thus becomes a triangular shaped function as shown in Figure 5.6, with

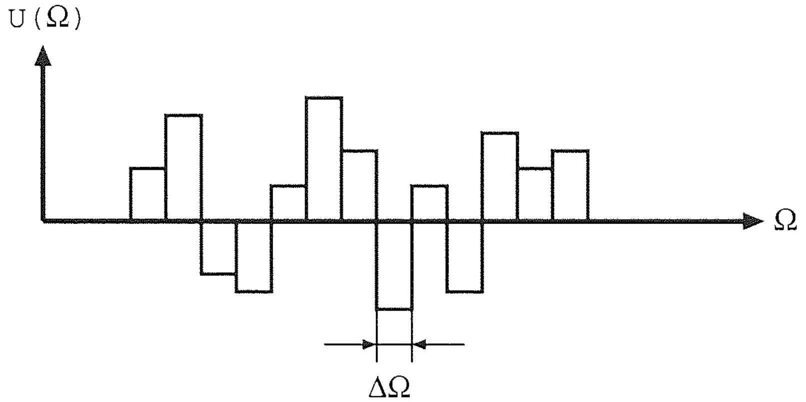

Figure 5.5: Representation of noise field in the numerical simulations.

the peak value of σ^2, and with the area under the triangular function of $\sigma^2\Delta\Omega$. Considering this fact, this function becomes $\sigma^2\Delta\Omega\delta(\Omega-\Omega')$ as $\Delta\Omega$ approaches zero.

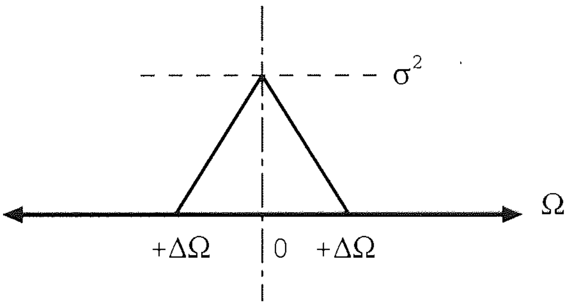

Figure 5.6: Autocorrelation of the piecewise noise field $< U(\Omega)\ U^*(\Omega') >$.

One can equate the triangular function under the condition that $\Delta\Omega \rightarrow 0$ to Eq. (5.20). We thus obtain the relation between the noise variance and the power spectral density as

$$\sigma^2 = \frac{\delta S}{\Delta\Omega} \tag{5.21}$$

Hence, we can now derive the relationship between the noise variance and the noise contribution in Eq. (5.17) as

$$\sigma_\nu^2 = \frac{\Pi_\nu\ \delta z}{\Delta\nu\ \Delta\Omega}. \tag{5.22}$$

Alternatively, the relation in Eq. (5.22) can also be derived by considering a periodogram representation of signal shown in Figure 5.7.

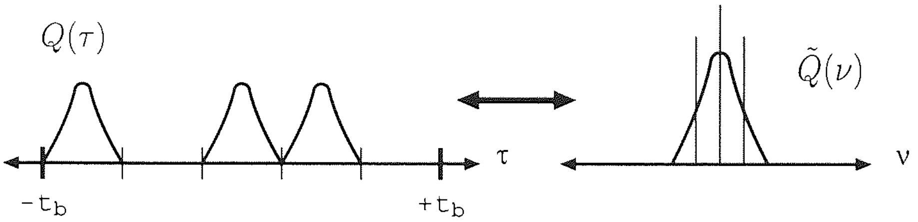

Figure 5.7: Signal representation in time and frequency domain.

We begin by considering the average power of the samples which represent the random signal. The average power of the random signal in the periodogram is

$$P_{av} = \lim_{T\to\infty} \frac{1}{T} \int_{-t_b}^{t_b} |Q|^2 dt = \lim_{T\to\infty} \frac{1}{T} \int_{-\infty}^{\infty} |\tilde{Q}|^2 d\nu, \tag{5.23}$$

where $T = 2\ t_b$. Here the power spectral density is defined as

$$S(\nu) = \lim_{T\to\infty} \frac{|\tilde{Q}|^2}{T}, \tag{5.24}$$

which may be approximated by

$$S(\nu) \simeq \frac{|\tilde{Q}|^2}{T} \tag{5.25}$$

for a sufficiently large T. Now one may work out the additive power in terms of the power spectral density increment. By substituting Eq. (5.17) into the additive power equation, we arrive at

$$\delta|Q|^2 = T\ \delta S(\nu) = \frac{\Pi_\nu\ \delta z\ T}{\Delta\nu}. \tag{5.26}$$

The term $\delta|Q|^2$ may be interpreted as the variance of the AGWN. Thus

$$\sigma_\nu^2 = \frac{\Pi_\nu\ \delta z\ T}{\Delta\nu}. \tag{5.27}$$

Because $\Delta\Omega = 1/T = (2\ t_b)^{-1}$, Eq. (5.27) is identical to the noise variance in Eq. (5.22) that we have derived earlier.

In the simulations, we need to use a normalised noise variance. By using the definition given in Eq. (5.7), the normalised noise variance yields

$$\begin{aligned} \sigma_{\nu,norm}^2 &= \frac{\delta S}{P_{norm}\ t_{norm}}\ 2T_b \\ &= \frac{z_{norm}}{P_{norm}\ t_{norm}} \frac{\Pi_\nu}{\Delta\nu}\ \delta Z\ 2T_b. \end{aligned} \tag{5.28}$$

In the implementation of a random noise in the simulations, we will generate two Gaussian deviate random numbers with zero mean and a variance of $\sigma_{\nu}^2/2$ for each frequency ν. A complex random noise is constructed from the two random numbers each for the real and imaginary parts. The reduction of the variance by a factor of two is required so that the complex noise field has the correct variance of σ^2. The additive noise will be added at every step of the split-step Fourier method for the distributed Raman amplified transmission line.

5.4 Conclusions

In the design and development of high cost Raman amplified transmission systems, a highly accurate numerical simulation model is essential to provide reliable and trustable results before expensive experiments or implementations are to be carried out. The nonlinear Schrödinger (NLS) equation with Raman response described in Section 3.4.4 may be used. However, the model is rather complicated and may require a considerable amount of CPU time, which is crucial especially for the system optimisation tasks.

This chapter has described an effective approach, called generalised Raman amplified gain model approach, to simulate Raman amplified optical transmission systems. The approach consists of a combination of deterministic signal analysis in frequency domain and the transient full direct numerical NLS simulation. The simulation of a Raman amplified transmission line will be divided into two steps. First, the full frequency power balance model is solved to obtain the effective attenuation and noise information. In this step the signals are represented in their deterministic form. The effective attenuation governs the signal power evolution due to Raman amplified gain. In the second step, the information obtained from the deterministic approach is fed into the direct numerical simulation model to solve for other linear and nonlinear effect.

Last, the modelling of noises in the Raman amplified transmission line has been described. The noises in Raman amplification process are from two origins namely the amplified spontaneous Raman scattering and double Rayleigh scattering. The incorporation of noise information obtained from the deterministic approach into the full direct numerical model has been described.

Chapter 6

Upgrade of a standard fibre network to 40 Gb/s per channel using a hybrid amplification scheme

6.1 Introduction

New trends in modern telecommunication such as Internet and mass media broadcasting services have pressed a challenge against the development of data transmission capabilities. Within a few years, this high demanding capacity of data transmission will be supported only by optical systems. However, many of recently developed optical technologies, for instance optical amplifiers, have been brought to their limit leaving a challenge to the technologists to keep up with the dramatic growth in the demand of bandwidth.

Moreover, the worldwide economic downturn forces network engineers to focus on an attempt to minimise the cost of strategies for increasing the network capacity. Upgrade of the existing networks is therefore the most interesting and challenging task for the technologists and engineers in this decade.

Bandwidth increasing can be either done by providing more channels in a wavelength division multiplexing (WDM) system or by enhancing the bit rate of already existing channels using time division multiplexing (TDM) or by a combination of both. From the view of economy, the capacity upgrade by using the TDM technique is more preferable because there are less affords needed to replace the already existing network components such as Erbium doped fibre amplifiers (EDFAs) as required by the latest WDM systems. In recent years, the development of high bit rate long haul transmission systems has been focussed on 40 Gb/s technology in both single channel and WDM systems [69, 70, 71, 72].

However, to operate 40 Gb/s systems requires us to find the solution to a number of technological challenges. One of the most detrimental problems is an increase in nonlinear effect due to the fact that a higher launch power is required to maintain the level of optical signal-to-noise (OSNR) ratio. For example, in order to achieve the same OSNR relative to 10 Gb/s channels, the 40 Gb/s channel launch power has to be increased by 6 dB to make up for the four times larger signal bandwidth. Other technological challenges include the increased sensitivity to accumulated chromatic dispersion due to a larger signal bandwidth, dispersion slope, noise accumulation and polarisation-mode dispersion (PMD).

The primary approach to 40 Gb/s long-haul transmission is to reduce and tolerate system nonlinear effects. The approach is referred to as "quasi-linear transmission" in which the signal power is maintained to be high enough to achieve an acceptable OSNR, but sufficiently low to avoid the detrimental nonlinear effects. As discussed in Chapter 3, Raman amplification helps to minimise the signal power variation and thus becomes a key approach to achieve the 40 Gb/s long-haul transmission with Tb/s capacity [73].

This chapter aims to focus on the study and development of techniques to enhance and optimise the 40 Gb/s based quasi-linear transmission systems. The research is mainly focused on the terrestrial standard fibre systems with no active signal regeneration. A technique, so called "nonlinearity management" to find a compromise between the OSNR and nonlinear effects via the use of hybrid amplification, will be numerically investigated. The transmission performance will be further studied by comparing the impact of dispersion maps and fibre types. Last, the enhancement of the performance is attempted by optimising the average dispersion of the dispersion maps.

6.2 Nonlinearity management

In 40 Gb/s systems, the transmission is limited by a number of detrimental effects. Despite the pulse broadening due to group velocity dispersion (GVD) can be compensated for by a dispersion management scheme, the short pulse width required in the 40 Gb/s system makes the pulse spread so quickly that the transmissible distance is limited to less than 4 km without dispersion compensation in a standard single mode fibre (SMF). Moreover, the wide bandwidth, as a result of shorter pulse, amplifies the effect of higher order dispersion, which is to be compensated for carefully at this bit rate. One more detrimental effect comes from fibre nonlinearity as a result of the high launch power required to maintain the optical signal-to-noise ratio (OSNR). The transmission distance with a too high launch power is limited by the nonlinear effects such as self phase modulation (SPM) whereas the system becomes noise limited when a too low launch power is used.

Modern transmission fibre offers a solution to this dilemma, in which the pulse suffers from the nonlinearity when its power is too high and has its OSNR degraded when the power is too low, by presenting a very low dispersion slope and large effective core area to reduce nonlinearity [73]. However, the investment in a new transmission cable with modern fibre raises a number of issues concerning economy. In terrestrial systems, in which the maximum distance is always in the order of 1000 km, an upgrade of the existing SMF-based system is more preferable.

In a quasi-linear transmission scheme, the signal level must be well maintained in the region, in which the signal suffers least nonlinearity and noise. In conventional lumped amplification based on Erbium doped fibre amplifiers (EDFAs), the loss is exactly compensated for by the gain of the EDFAs. As such, the amplifier spacing must be short enough to maintain signal power level within such a safety region that the OSNR does not degrade too much. This amplifier spacing can be extended by using the distributed amplification scheme such as distributed Raman amplification

(DRA). As shown in Chapter 2, the distributed nature of DRA effectively helps to maintain the signal level, and hence allows a longer amplifier spacing. Moreover, the DRA presents a better noise performance. However, most commonly used backward pumped DRA suffer from additional double Rayleigh scattering (DRS) noise, especially near the output end of the Raman amplified fibre where the high signal and high amplification gain boost the amount of DRS noise. The DRS is much more effective in a smaller core fibre such as dispersion compensating fibre (DCF) as the light intensity is higher. Therefore, the use of hybrid amplification scheme may help to alleviate this problem by keeping the output signal power of the Raman amplified transmission line low enough to avoid the DRS. The rest of the loss is compensated for by means of EDFAs. Figure 6.1 shows the schematic diagram of the hybrid amplification scheme with standard fibre transmission system.

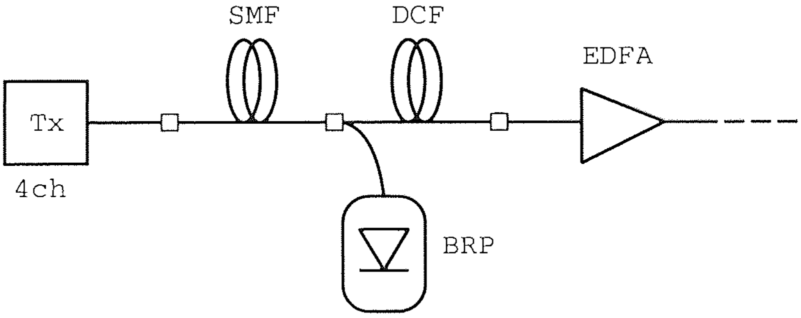

Figure 6.1: Hybrid amplification system schematic.

6.2.1 Optimisation of the system configuration using the average power approach

Considering the upper limit on the signal level imposed by nonlinearity and the lower limit by the required OSNR, the best performance of a fibre transmission system corresponds to the optimal compromise between the requirements of high OSNR and minimal nonlinear impairments [74]. The use of hybrid amplification scheme allows for a further control over the signal power level and thus the nonlinearity.

Under the assumption that nonlinearity always leads to a degradation of the system performance, the nonlinear phase shift (NPS) given by

$$NPS = \frac{2\pi}{\lambda} \int_0^L \frac{n_2}{A_{eff}} P(z) dz, \tag{6.1}$$

can be considered as a measure of nonlinear impairments. In such case, it is possible to find the optimal system configuration by performing a conditional minimisation of the NPS under a fixed OSNR, or vice versa, maximising the OSNR for a fixed NPS. The power balance model described in Chapter 3 can be used to obtain the necessary information to calculate the NPS and OSNR. In Refs. [74] and [75], the optimisation of the system configuration has been presented. We define the parameter η to reflect the system configuration. η is a ratio between the gain provided by DRA (in dB) and the overall gain required to fully compensate for the transmission loss. Figure 6.2 shows the superposition of the contour plots of OSNR and NPS in the (input signal, η) plane, and can be seen as a geometrical representation of the conditional minimisation of NPS under a fixed OSNR.

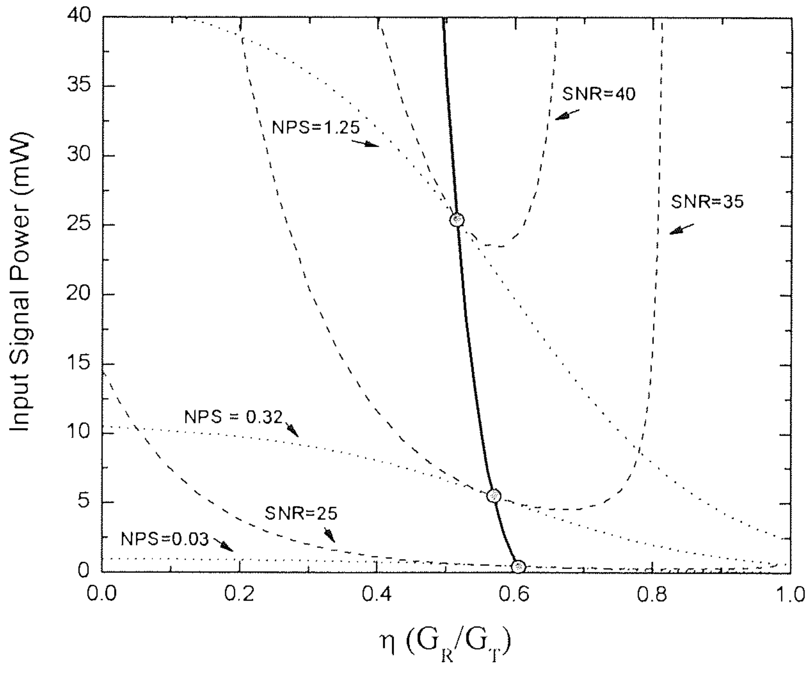

Figure 6.2: Superimposed contour plots for the OSNR and the NPS versus input signal and η. The think line follows the optimal input signal for each η.

The system under consideration is a 4 channel WDM system with 100 GHz channel spacing centred at 1.55 μm. The SMF is 100 km long. The length of DCF is chosen such that the average span dispersion is zero. The hybrid amplification system consists of a backward pumped DRA and EDFA with a noise figure of 4.5 dB (*see* Figure 6.1). The fibre parameters may be found in Appendix A.

In Figure 6.2, the points of tangency between the curves of fixed NPS and the curves of fixed OSNR represent the points that minimise the NPS under a fixed OSNR, and thus the ones that optimise the system. The curve that follows these points gives the dependency of the optimal signal power for each η ratio or vice versa. Note that the variation of the gain ratio is small and falls in the range between 0.5 and 0.6.

6.2.2 Direct numerical analysis

To confirm this analysis, we have performed a direct numerical simulation using the generalised Raman amplified gain model approach described in Chapter 5. The direct numerical simulation procedure is comprised with two important steps. First, the effective attenuation and noise contributions (both amplified spontaneous emission (ASE) and DRA noises) are obtained by means of solving full frequency power balance model. The information is then fed into the nonlinear Schrödinger (NLS) equation solver to solve for signal dynamic including the interplay between various nonlinear effects and dispersions in the fibre.

The signal are represented by a pseudo-random bit sequence (PRBS) of $2^9 - 1$ bit length per channel. The pulse format is return-to-zero (RZ) Gaussian with 12.5 ps full-width at half-maximum (FWHM) pulse width (corresponding to 50% duty cycle).

Figure 6.3 shows the energy evolution of the signal in the transmission line. Note that the last stage of amplification is carried out by EDFA to avoid the DRS problem.

The full optimisation of the system configuration is done by calculating the maximum error-free propagation distance varying the launch peak power and amplification ratio η. The error-free propagation distance is defined as the distance at which the BER is less than 10^{-9}. In our case, we assume that all noises follow Gaussian

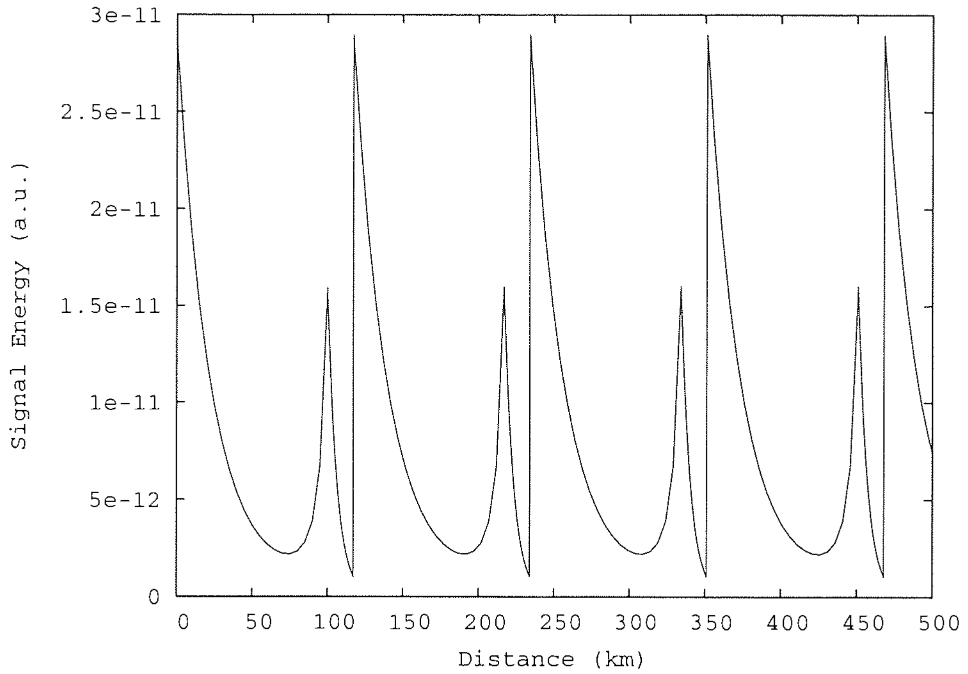

Figure 6.3: Signal energy evolution in the transmission path with hybrid amplification. $\eta = 0.55$.

statistics; therefore, the criterion of a Q-factor greater than 6 is used to define the error-free propagation.

Figure 6.4 depicts the contour plot showing the maximum propagation distance against the amplification ratio η and input peak power. The optimal configuration of this particular case corresponds to $\eta = 0.55$ and the launch peak power of 3 dBm, which is in a good agreement with the results obtained from the average power study described earlier.

Figure 6.5 illustrates the Q-factor evolution of each transmission channel. The optical WDM signal is demultiplxed by a super Gaussian optical filter with a bandwidth of 80 GHz, and detected by a square law detector. The detected electrical signal is then filtered by a low pass 5^{th} order Bessel filter with the bandwidth of 42 GHz. The maximum distance of this configuration is about 1400 km, which is sufficient for most terrestrial networks.

By examining the eye diagram of the signal at the maximum error-free distance, one may find that the transmission is limited by both nonlinearity (resulting in

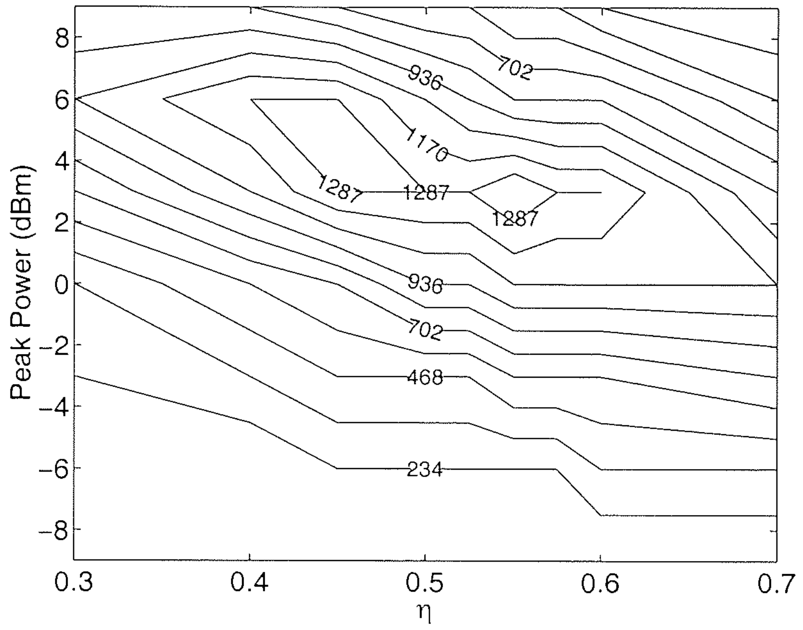

Figure 6.4: Contour plot showing the maximum propagation distance (in km) versus η and input peak power. Note that the maximum distance is determined from the worst channel.

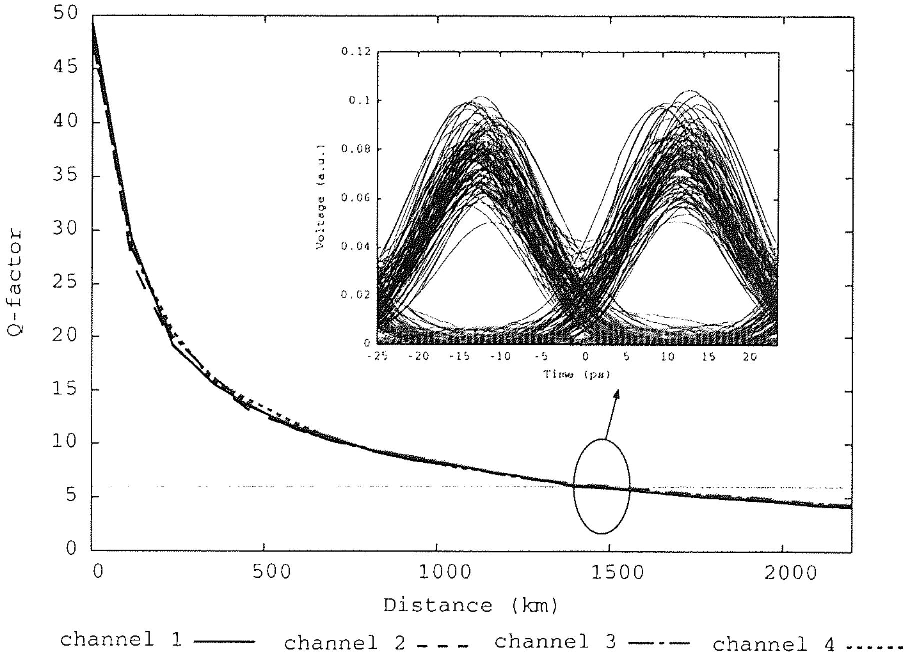

Figure 6.5: Q-factor evolution of each channel. The inset figure shows the eye diagram of channel 2 at 1400 km.

timing jitter) and noise (amplitude jitter).

In this section, we have proposed a hybrid amplification scheme to enhance the transmission performance of a 40 Gb/s system. The use of DRA allows a control of nonlinearity through the signal power level whereas the EDFA helps to avoid the DRS problem. The optimal amplification gain ratio (η) found by using the average power is necessary to ensure the maximum performance.

6.3 Impact of the dispersion maps on the transmission performance

In a high bit rate optical transmission such as the 40 Gb/s system, the transmission performance is highly sensitive to the nonlinear effects, which the signal experiences during transmission. Due to a high local dispersion of the SMF, the pulse is extremely broaden during its propagation. The pulse spreading may help to reduce the nonlinear effects as the pulse peak power is considerably decreased at the broadest point. In general, the pulse is broadest at the end of the SMF in a conventional SMF+DCF map, and begins to be re-compressed in the DCF section. A careful design of dispersion map by using a prechirping strategy allows one to manage the pulse broadening characteristic within a propagation map. Taking into account the loss and amplification characteristics, this strategy may help to minimise the nonlinear effects, and hence enhance the transmission performance.

In this section, we investigate an impact of dispersion maps on performance of some 40 Gb/s transmission systems. Three types of maps are to be considered: (1) a symmetric map, (2) a typical asymmetric map and (3) an asymmetric map with large span average dispersion. Figure 6.6 illustrates those three dispersion maps.

In Map 1, the pulse is launched with a very large pulse width as a result of prechirping. The pulse is re-compressed within the SMF reaching the chirp free point at around the middle of the SMF section and then begins to broaden again. In the DCF section, the pulse is re-compressed and reaches its broadest point at the end of the DCF section. The main feature of this map is the fact that the pulse

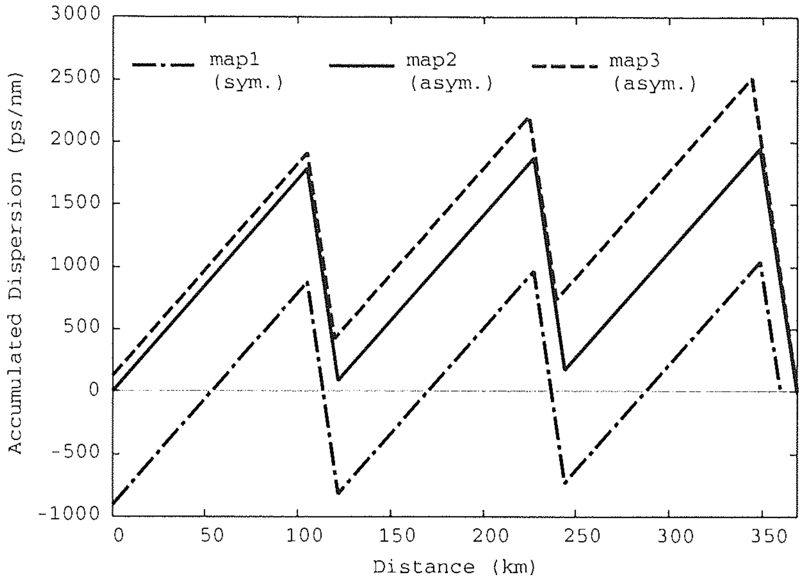

Figure 6.6: Dispersion map.

is broadest at the end of the DCF where the EDFA restores the pulse power. As the pulse is broadest where its energy is highest, the relatively low peak power thus helps to suppress the nonlinear effects.

On the other hand, Map 2 and Map 3 present a very large accumulated dispersion to minimise the nonlinear effects. The idea is to tackle the inter-channel nonlinear effects such as cross phase modulation (XPM) and four-wave mixing (FWM) by maintaining a high local dispersion to average out the nonlinearity and avoid the phase matching condition.

6.3.1 Comparison of the dispersion map performance

To compare the performance of each map, direct numerical simulations of the transmission systems for all maps have been performed. We consider 16 channels 40 Gb/s systems with those three dispersion maps. The pulse format used in the simulation is Gaussian RZ with 12.5 ps FWHM pulse width. The bit pattern is $2^9 - 1$ PRBS per channel with 100 GHz channel spacing. Each span of SMF fibre used in all dispersion maps is 105 km long. In Map 1 and Map 2, the length of the DCF has been chosen to provide the span average dispersion of 0.7 ps/nm/km whereas the span average dispersion is 2.5 ps/nm/km for Map 3. A DCF is used as a prechirp fibre in Map 1 and Map 3 to achieve the desired prechirp. The parameters of the fibres used in the simulations can be found in Appendix A.

We evaluate the transmission performance of each map by monitoring the BER (as calculated from the Q-factor assuming that the system follows the Gaussian statistics) after three map periods. The reason for choosing this way of investigating the map performance is due to the requirement for comparing the simulation results with experiments conducted by *France Telecom* under a collaboration between them and the University. Note, however, that the experimental results obtained by the company are not to be presented in this thesis. The schematic diagram of the simulation setup is illustrated in Figure 6.7.

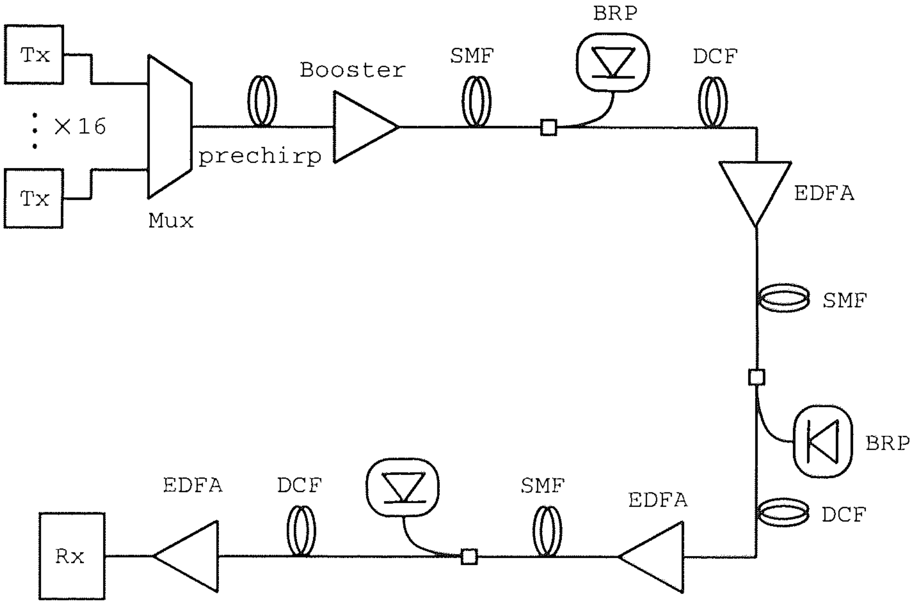

Figure 6.7: Schematic diagram of the 3-map transmission.

In the simulation, 16 channels of modulated signals with the peak power of 0 dBm are multiplexed by a WDM multiplexer (MUX) and launched into a prechirp fibre if necessary. The EDFA booster is used to adjust the power launched into the first section of the SMF. We consider the peak power of the signal at this point the launch power. The loss in the transmission span is compensated for by a hybrid amplification scheme comprised with a backward pumped DRA and an EDFA. Note that each EDFA in this simulation exhibits a noise figure (NF) of 6 dB. In all cases, the on/off DRA gain is a total of 18.5 dB, which corresponds to an amplification gain ratio η of around 0.6.

The simulation results are shown in Figure 6.8. The BER of the transmission for each map has been plotted against the launch peak power.

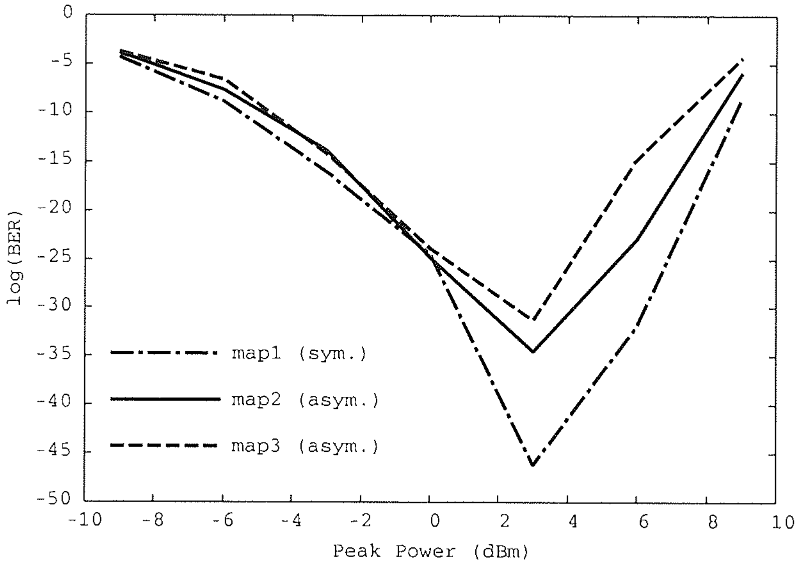

Figure 6.8: Plot of log(BER) against launch peak power for different dispersion map after three map periods.

As expected, the symmetric map (Map 1) delivers the best performance for the whole range of peak power following by asymmetric Map 2 and Map 3, respectively. The peak power around 3 dBm for all maps delivers the best performance. After that, the BER increases because the nonlinearity becomes dominant as a performance limiting factor. The results suggest that a well designed dispersion map importantly helps to enhance the performance of the transmission systems at this bit rate. We confirm this conclusion by calculating the maximum error-free propagation distance of each map. Map 1 exhibits the longest error-free distance of 915 km following by Map 2 and Map 3 of around 755 km and 737 km, respectively. Note that the error-free distance is determined from the middle channel (channel 8).

6.3.2 Transmission performance under the optimal configuration

The amplification gain ratio η of 0.6 of the hybrid amplification scheme used in the simulations in the previous section has been chosen for the comparison purposes with the experiments. In this section, we confirm the findings of the above by performing an optimisation of the gain ratio to guarantee a fair comparison. Here, we compare only the symmetric map (Map 1) and the asymmetric map (Map 2). The simulation parameters are identical to the previous section for both Map 1 and Map 2 cases.

Figures 6.9 and 6.10 show the contour plot of the error-free transmission distance against the launch peak power and the amplification gain ratio of the symmetric and asymmetric map, respectively. For the symmetric map (Map 1), the optimal configuration corresponds to the gain ratio $\eta = 0.65$ and the launch peak power of 3 dBm. The maximum error-free transmission distance is about 800 km and 1230 km for the worst and the 8^{th} channels, respectively. One may see that, by optimising the gain ratio, the transmission distance can be improved. The simulation results also suggest that the deviation of η by ± 0.1 from its optimal value may lead to a degradation of error-free transmission distance by one map period, which may be acceptable from the engineering point of view.

For the asymmetric map (Map 2), the optimal gain ratio is 0.5 and the optimal peak power is 3 dB. The maximum error-free transmission distance is about 737 km and 1106 km for the worst and the 8^{th} channels, respectively. Again, the optimisation of η helps to improve the transmission distance, too.

Comparing the maximum error-free transmission distances achieved by these two maps, Map 1 still shows a superior performance, which confirms the finding in the previous section.

6.4 Optimisation of the span average dispersion

In our 40 Gb/s transmission systems considered in this thesis, the pulse propagation is considered to fall into a quasi-linear regime. The launch power has to be main-

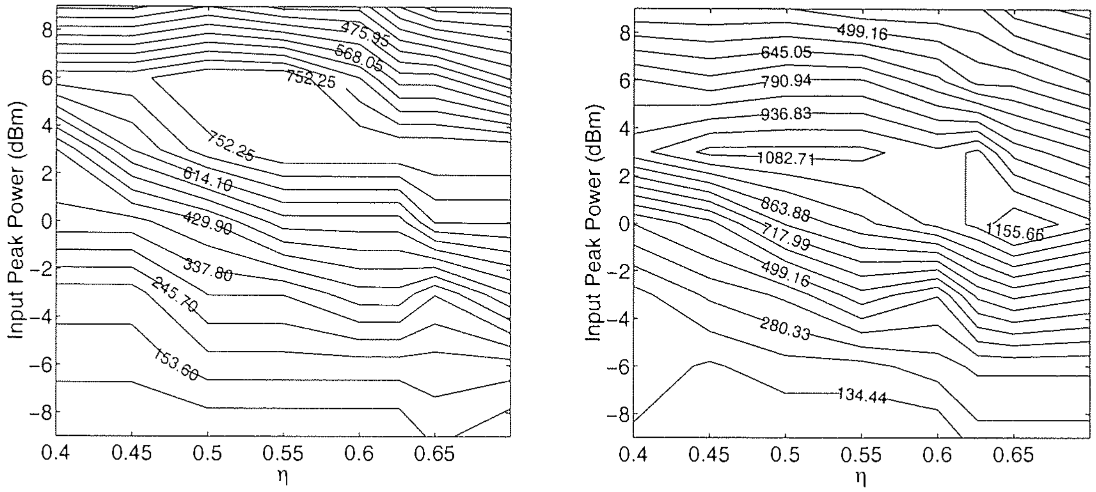

(a) (b)

Figure 6.9: Contour plot showing the optimal error-free transmission distance for the symmetric map (Map 1) against the launch peak power and η. (a) Error-free distance determined from the worst channel. (b) Error-free distance determined from the middle channel (channel 8).

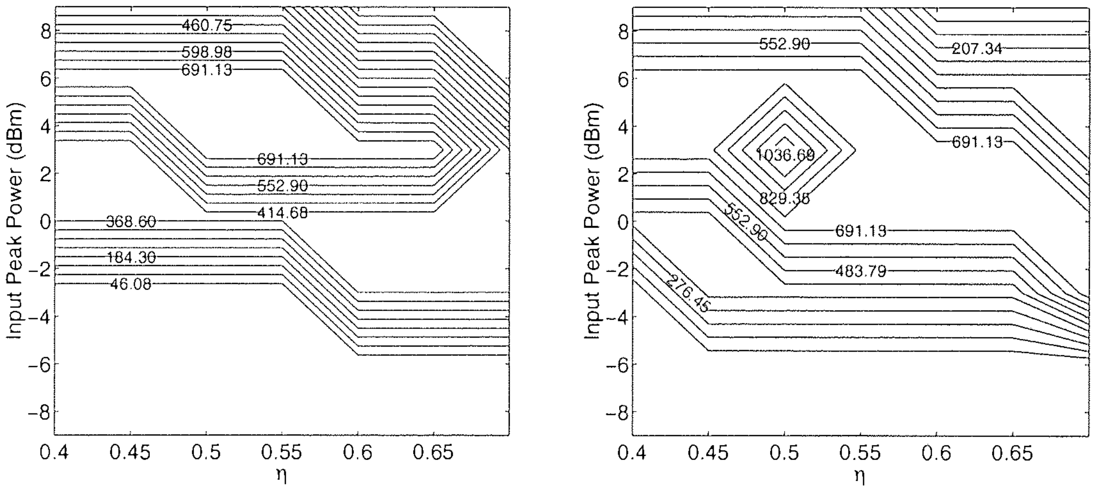

(a) (b)

Figure 6.10: Contour plot showing the optimal error-free transmission distance for the asymmetric map (Map 2) against the launch peak power and η. (a) Error-free distance determined from the worst channel. (b) Error-free distance determined from the middle channel (channel 8).

tained sufficiently high to achieve a desired OSNR. Due to this reason, the pulse propagation is highly affected by the fibre nonlinearity, which becomes a limiting factor through its effects such as SPM, XPM and FWM. To avoid the problems due to nonlinearity, the signal power is not to exceed a certain limit above which the nonlinear effects become detrimental. The discussion in the previous section shows a strategy to find an optimal regime to tackle the nonlinearity while maintaining a desired OSNR to insure the maximum error-free transmission distance.

As the signal transmission is partly considered a nonlinear propagation, the signal spectrum is affected by the nonlinear effects through the nonlinear phase shift across the signal spectrum leading to a nonlinear chirp in the signal pulse. The effect eventually translates into a pulse broadening by the group velocity dispersion, and hence the degradation of signal quality. In a nonlinear transmission regime, a zero average span dispersion map does not guarantee the best transmission performance as it happened in the linear regime. Therefore, the span average dispersion may play an important role in the transmission performance at this bit rate.

In this section, we perform an optimisation of the span average dispersion and investigate its influence on the transmission performance. The transmission system to be considered is depicted in Figure 6.11. The system is a dense WDM 8×40 Gb/s transmission with a reference centre wavelength located at 1.55 μm. The WDM channel spacing is 100 GHz.

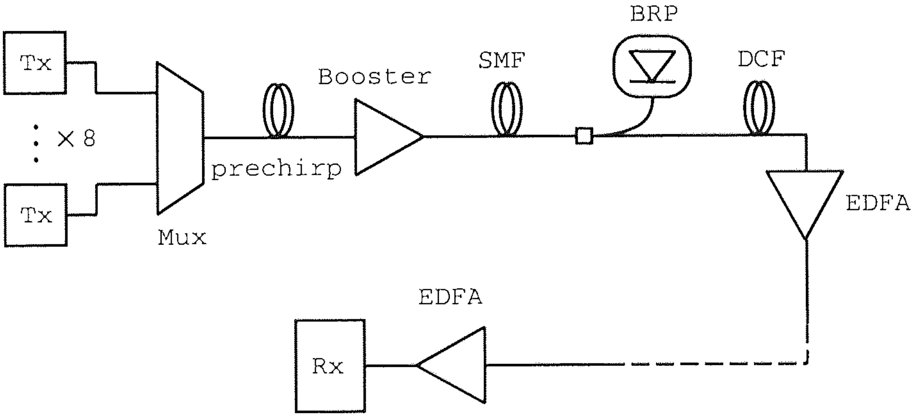

Figure 6.11: Schematic diagram of the 8×40 Gb/s system.

For comparison, we consider two dispersion maps: (1) a symmetric map (Map 1) and (2) an asymmetric map (Map 2) with most features similar to those in the previous section (*see* Figure 6.6) except the fact that the SMF segment here is 100 km long. Again, a segment of DCF is used as a prechirp fibre for Map 1. To vary the span average dispersion $< D >$, the length of DCF in each dispersion map is prescribed to achieve a desired $< D >$. We use a hybrid amplification scheme comprised with a backward pumped DRA and an EDFA to compensate for the fibre losses. The noise figure of each EDFA is 6 dB. The amplification gain ratio η for both cases of dispersion maps is fixed to 0.55.

The optical signal used in the simulations is Gaussian RZ format modulated with a PRBS data pattern. The PRBS length is $2^9 - 1$ per channel. The output peak power of the signal after the multiplexer is fixed to 0 dBm for all cases, and will be boosted to a desired level by an EDFA booster right before the first segment of SMF. The transmission performance is evaluated by means of the Q-factor calculation at each propagation distance. The received optical signal is demultiplxed by a WDM demultiplexer with an optical bandwidth of 80 GHz. The optical filter is a super-Gaussian filter of order 20. The signal in each channel is then detected by a square law detector converting the signal into the electrical domain and electronically filtered by a 5th order electrical Bessel filter.

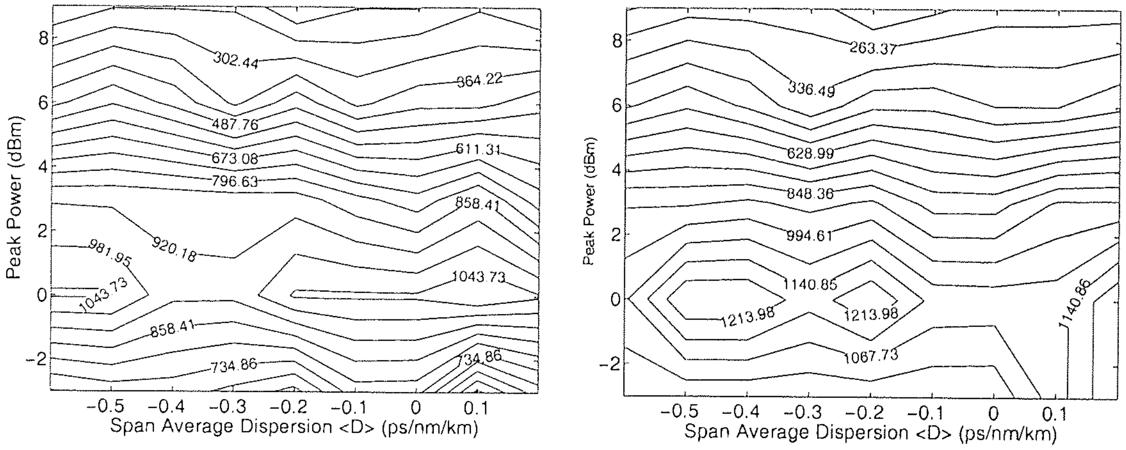

(a) (b)

Figure 6.12: Contour plot showing the optimal error-free transmission distance for the symmetric map (Map 1) against the launch peak power and span average dispersion. (a) Error-free distance determined from the worst channel. (b) Error-free distance determined from the middle channel (channel 4).

The optimisation result for the symmetric map (Map 1) is shown in Figure 6.12 where the contour plot of the maximum error-free transmission distance against the launch peak power and span average dispersion is depicted for the worst and the middle channel (channel 4) in sub-figures (a) and (b), respectively. The results show that there are two maxima for the maximum-error free transmission distance which correspond to $< D >= 0.1$ ps/nm/km and $< D >= -0.5$ ps/nm/km with the optimal peak power of 0 dBm for both maxima. The maximum distance is around 1100 km for the worst channel and is 1287 km for channel 4.

Figure 6.13 illustrates the optimisation results for the asymmetric map (Map 2). Similar to the previous case, the optimal peak power is found to take the value of 0 dBm. There are, again, two maxima for the error-free transmission distance at $< D >= -0.3$ ps/nm/km and $< D >= -0.5$ ps/nm/km with the maximum distance of 1210 km and 1404 km for the worst and the middle channel, respectively.

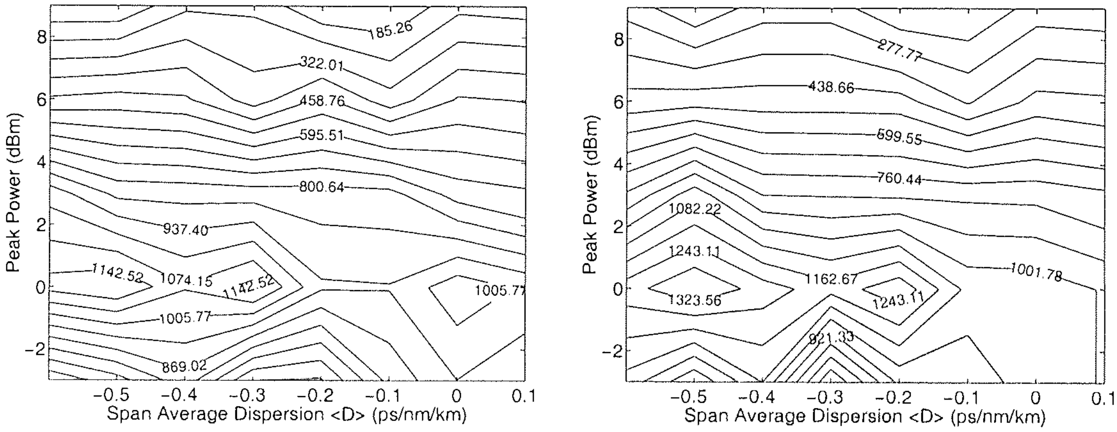

(a) (b)

Figure 6.13: Contour plot showing the optimal error-free transmission distance for the asymmetric map (Map 2) against the launch peak power and span average dispersion. (a) Error-free distance determined from the worst channel. (b) Error-free distance determined from the middle channel (channel 4).

Surprisingly, the results show that the asymmetric map exhibits a slightly better performance than the symmetric map as in the previous cases. However, the difference is only one map period. Therefore, it is still fair to conclude that both maps show a similar performance.

From the analysis in this section, one may find that the optimisation of the span average dispersion may help to improve the transmission performance; although, the improvement is not much as only one map period improvement on average is achieved.

6.5 Conclusions

In this chapter, a study and development of techniques to enhance and optimise the 40 Gb/s based quasi-linear transmission systems have been described. The 40 Gb/s optical transmission technology has become the most promising technique to keep up with the rapid growth of a high demand in massive data communication. However, the economic recession experienced worldwide in these recent years and probably a few years in the future turns the interest of research in the field to an upgrade of the existing systems.

Distributed Raman amplification (DRA), enjoying it resurgence due to an availability of high power semiconductor pump lasers, may be used to enhance the transmission performance of 40 Gb/s systems. The higher noise performance due to its distributed amplification nature makes DRA more attractive compared to its competitor, Erbium doped fibre amplifier (EDFA) and helps to improve the optical signal-to-noise (OSNR) ratio of the transmission. It also allows a possibility to extend the amplification spacing which may result in a reduced overall cost of the systems.

In a high bit rate system such as the 40 Gb/s, the best transmission performance corresponds to a compromise between the requirement of a high OSNR and minimal nonlinear impairments. The use of DRA effectively helps to maintain the minimum signal level well above the noise floor, but has an important problem of the double Rayleigh scattering (DRS) noise at the end of the transmission fibre close to the backward Raman pump (BRP) where the gain is highest, and in the dispersion compensating fibre (DCF) where the DRS coefficient is relatively high. Therefore, a hybrid amplifier that consists of a DRA and EDFA may help to alleviate this problem by avoiding a too high signal power close to the BRP and in the DCF. The rest of the fibre loss is compensated for by the EDFA. The ratio between the DRA and EDFA gains (in dB), or so-called η parameter, must be optimised to achieve the most effective hybrid amplification scheme. Section 6.2 presents a nonlinearity management approach to determine an appropriate η for a transmission system.

To ensure the best transmission performance, an influence of the dispersion maps has been investigated. We studied the impact of three types of dispersion maps including a symmetric and two asymmetric maps on the transmission performance. The results suggest that a well designed dispersion map effectively helps to improve the performance of transmission systems at this high bit rate.

Last, the optimisation of the span average dispersion has been carried out. Its influence on the transmission performance has also been investigated. The optimisation delivers only a map period improvement of the error-free transmission distance. This finding may also suggest that the transmission schemes we considered in this chapter are more limited by the noise than by the nonlinear effects as the nonlinear support for the quasi-linear propagating pulses is rather weak in this system.

Chapter 7

Conclusions

A rapid growth in the demand of massive data communication as a result of the globalisation has stimulated the research and development of several techniques in all areas of optical communication. However, the economic recession, experienced worldwide during the past few years and possibly some years in the future, has pressed a challenge against the developers in attempting to provide a more efficient solution with an economy cost. With these criteria in mind, the trend of optical communication system developments in the end of the last decade and in this decade puts its emphasis on the performance upgrade of already installed systems rather than on the introduction of new systems. Some new techniques, nonetheless, are introduced to enhance the system performance, or to offer a solution to some problems unsolvable by conventional approaches. The technique of exploiting Raman effect in various optical devices, such as wavelength converters and optical amplifiers, is one of the novel techniques proposed to economically enhance the system performance.

This thesis has presented the analyses and designs of some devices and advanced transmission schemes embracing Raman effect. The research was carried out mainly by using numerical modelling techniques.

Firstly, some background on the development of optical fibre communication systems was reviewed in Chapter 1, in which the problems of optical transmission systems and their solutions were addressed in a chronological order as the demand of a higher bit rate has been continuously growing. Some problems remained to be solved, such as the problem of fibre nonlinearity and noise at a high bit rate, have also been stated and thus led to a motivation of this research.

In Chapter 2, a review of theories and properties of optical fibres was presented to aid the understanding of the mechanism behind optical signal transmission within optical fibre. Important fibre characteristics, such as optical losses, chromatic dispersion and fibre nonlinearities were briefly discussed.

Chapter 3 provides a theoretical background on the Raman effect viewed from its historical perspective, beginning when C.V. Raman first observed a phenomenon referred to as spontaneous Raman scattering in 1928, and a discussion on the stimulated version of the scattering, which is the underlying principle of most Raman related applications in optical communication. The most interesting use of stimulated Raman scattering (SRS) is its potential to turn a passive optical fibre into an active gain medium, by which the wavelength conversion and optical amplification may be developed. Raman amplifiers have been proven to help improve the optical signal-to-noise ratio (OSNR) because of its better noise performance and distributed gain structure. Lumped Raman amplifiers, however, have drawn a considerable attention as a breakthrough in the ultra-wide band optical amplifier technology operating in various wavelengths not accessible by other types of optical amplifiers.

Additionally, in this chapter, an overview of the SRS theory to gain an understanding of the process was presented. By means of the simple single damped oscillator model, the approximate Raman gain spectrum can be predicted. The analysis also led to the development of the power balance model used in many parts of this thesis to describe the signal power interaction within Raman based devices. Lastly, the noises in the Raman amplification process were described. Two of the most important sources of noise are amplified spontaneous emission (ASE) and double Rayleigh scattering (DRS). The origin of the ASE noise is the spontaneous Raman scattering process, whereas the DRS noise comes from the amplification of signal or ASE noise scattered back and forth into the signal direction causing multipath interference. The incorporation of the ASE and DRS noises into the power balance model to accurately characterise the Raman based devices has also been described.

The main contributions of this research work have been presented in Chapter 4, Chapter 5 and Chapter 6 starting from the analysis of various types Raman fibre lasers (RFLs) by using a simple discrete power balance model to a further development of the model to govern the signal interaction within a full range of wavelength to characterise Raman amplification in optical transmission systems.

Chapter 4 presents the principle, design, analysis and optimisation of various types of RFLs that have recently drawn a considerable attention not only in the areas of optical communication, but also in other areas such as medicine, biomedical engineering and environmental science. The main advantage of exploiting the SRS process in fibre laser technology is the freedom it gives to operate in an extremely wide range of wavelengths. A cascade of wavelength conversion in combination with the employment of both Germanium (Ge) and Phosphorus (P) doped fibres allows one to design an RFL operating at any wavelength in the range of $1.1 - 1.7$ μm, where some parts of the spectral region may be inaccessible by other types of fibre lasers.

In that chapter, the design and optimisation of a two stage RFL based on Phosphosilicate fibre has been presented. The use of P-doped fibre makes it possible to achieve wavelength conversion from 1061 nm to 1480 nm by using only two stages of conversions, as compared to the required 5-stage scheme if the Ge-doped fibre is used. The key technology is the use of P_2O_5-Raman shift of $\sim$ 1330 cm^{-1} that is nearly three times larger than that of the SiO_2/GeO_2 Raman shift. The cavity of the RFL was optimised to ensure the highest performance. The optimal parameters of the cavity can be deduced from the graphical methods developed in this thesis or by using the full scale optimisation in the parameter space. The results show that the cavity efficiency exhibits a high tolerance to the deviation of its key parameters from their optimal values. Next, the investigation of the slope efficiency spectrum of some RFLs pumped by a double-cladded Yb-doped fibre laser was presented. The results show that the total efficiency spectrum depends mainly on the efficiency spectrum of the Yb-laser.

A technique to achieve radiation at/beyond the wavelength of 1.6 μm was also presented in Chapter 4. A novel design of composite RFL comprised with the concatenation of P- and Ge-doped fibre sections has been proposed. The composite RFL may be configured to provide a radiation spectrum in the range of $1.6 - 1.75$ μm, which is not achievable with typical rare-earth doped fibre lasers.

Finally, the study was extended to the design and analysis of a multiple output wavelength RFL. The novel design, comprised with a combination of a single stage P-doped RFL and a multiple output wavelength RFL based on Ge-doped fibre, may be used to pump flat gain Raman amplifiers in telecom applications. The use of Phosphosilicate core fibre offers a great reduction in the number of stages required and hence results in more stable system and potentially lower cost. Cavity optimisation has been carried out to ensure the high performance. An overall conversion efficiency of 28% has been achieved.

The discrete power balance model used in Chapter 4 was elaborated to cover a full range of wavelengths to provide information of power interaction within a Raman based devices. The results obtained from solving the full frequency model may be used to describe the signal dynamic in direct numerical simulation (by numerically solving the nonlinear Schrödinger equation). The details of the technique, so called generalised Raman amplified gain model, were described in Chapter 5. The approach consists of a combination of the deterministic signal analysis in frequency domain via the full frequency power balance equation and a transient direct numerical NLS simulation. First, the full frequency power balance model is solved to obtain an effective attenuation parameter and noise information. In the second step, the information obtained from the deterministic approach is fed into the direct numerical simulation to solve for other linear and nonlinear effects.

The approach developed in Chapter 5 was used to analyse some 40 Gb/s WDM transmission systems using hybrid amplification described in Chapter 6, where the study and development of various techniques to enhance and optimise the high bit rate quasi-linear transmission systems were presented. The main focus of the study in this research is aimed to develop the techniques to upgrade the existing terrestrial networks to 40 Gb/s per channel systems. In 40 Gb/s systems, the best transmission performance corresponds to a compromise between the requirement of a high OSNR and minimal nonlinear impairments. The use of a distributed Raman amplification (DRA) scheme effectively helps to maintain the minimum signal level well above the noise floor, but bears the important problem of the DRS noise at the end of the transmission fibre close to the backward Raman pump (BRP), where the gain is highest, and in the dispersion compensating fibre (DCF) where the Rayleigh scattering coefficient is relatively high. Therefore, a hybrid amplifier that consists of both DRA and EDFA may help to alleviate this problem by avoiding a too high signal power close to the BRP and in the DCF. The rest of the loss is to be compensated for by the EDFA. The ratio between the DRA and EDFA gains (in dB), or a so-called η parameter, must be optimised to achieve the most effective hybrid amplification scheme. The nonlinearity management approach was presented in this chapter to determine the appropriate η for a transmission system.

To ensure the best transmission performance, the influence of the dispersion maps on the transmission performance have also been investigated by a study of the impact of three types of dispersion maps including a symmetric and two asymmetric maps. The results showed how a well designed dispersion map effectively improves the performance of the transmission system at this high bit rate.

Lastly, an optimisation of the span average dispersion has been carried out. Its influence on the transmission performance has been investigated. The optimisation delivers only an improvement of a map period of the error-free transmission distance. The results suggested that the transmission schemes considered in this chapter are more limited by the noise than by the nonlinear effects.

As for the future work, one area concerning the topics addressed in this thesis is that of multiple output wavelength RFLs with some weak outputs, as required by some second order Raman amplifiers. As experienced in the analysis in Chapter 4, the multiple output RFL showed a sign on instability when one or more output powers are much lower than the others. One way to avoid this problem is to use a seed signal provided by a parametric process for the required weak power output [76, 77, 78]. The use of both Raman and four-wave mixing (FWM) frequency conversion may help to stabilise the weak output [79]. FWM requires a phase matching condition, which is related to the dispersion of the fibre medium. It is, therefore, interesting to investigate the characteristic and performance of this FWM-assisted multiple output wavelength RFL for various types of fibres.

Another area of future work relates to the further development of the Generalised

Raman amplified gain model approach to simulate the Raman amplification in optical transmission systems. In this thesis, the assumption that the Raman related signal dynamic is similar in all amplification spans has been made for simplicity and optimal simulation speed. Future work may concern the verification of this assumption by performing the calculation of the effective attenuation and noise parameters in each span and comparing the results to those obtained by the approach used in Chapter 5.

Appendix A

Fibre specification and data summary

G. 652 Single Mode Fibre (SMF)

Parameters	Value
Attenuation @1455 nm	0.257 dB/km
Attenuation @1550 nm	0.200 dB/km
Dispersion (D)	17 ps/nm/km
Dispersion slope (D_λ)	0.07 ps/nm^2/km
Nonlinear refractive index (n_2)	2.7×10^{-20} m^2/W
Rayleigh scattering coefficient (ϵ) @1455 nm	7.92×10^{-5} km^{-1}
Rayleigh scattering coefficient (ϵ) @1550 nm	6.41×10^{-5} km^{-1}
Core diameter ($2a$)	8.2 μm
Numerical aperture (NA)	0.124
Effective area @1550 nm(A_{eff})	80 μm

Table A.1: Single mode fibre G. 652 specification.

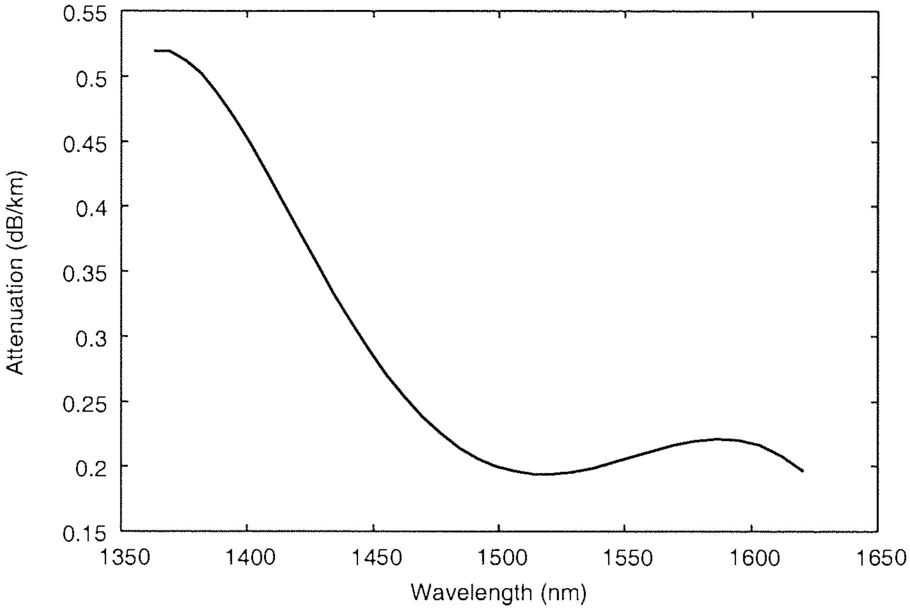

Figure A.1: Attenuation vs. wavelength of the G. 652 SMF.

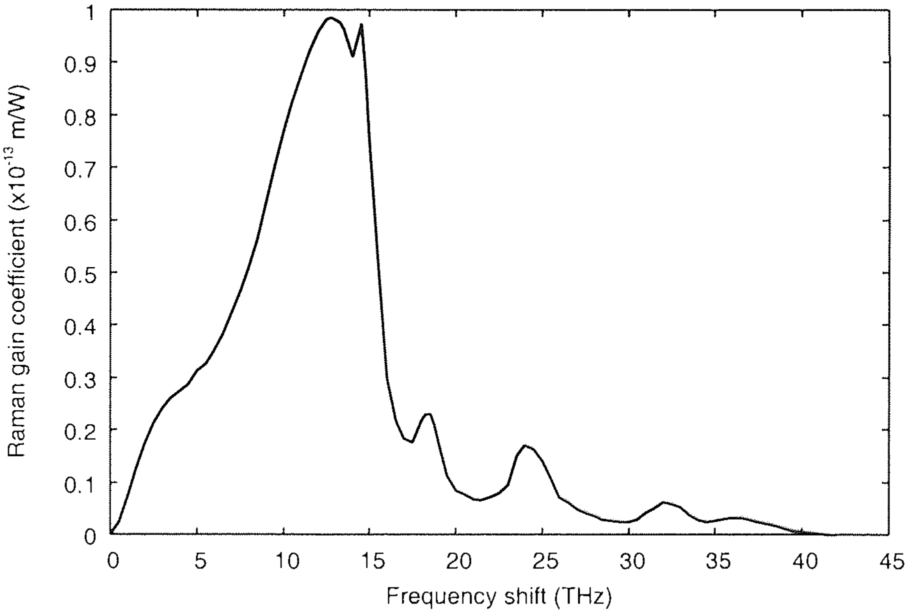

Figure A.2: Raman gain coefficient of the G. 652 SMF measured at the pump wavelength of 1 μm.

Dispersion Compensating Fibre (DCF)

Parameters	Value
Attenuation @1550 nm	0.58 dB/km
Dispersion (D)	-100 ps/nm/km
Dispersion slope (D_λ)	-0.41 ps/nm^2/km
Nonlinear refractive index (n_2)	2.7×10^{-20} m^2/W
Rayleigh scattering coefficient (ϵ) @1455 nm	94.40×10^{-5} km^{-1}
Rayleigh scattering coefficient (ϵ) @1550 nm	60.60×10^{-5} km^{-1}
Effective area @1550 nm(A_{eff})	19 μm

Table A.2: Dispersion compensating fibre specification.

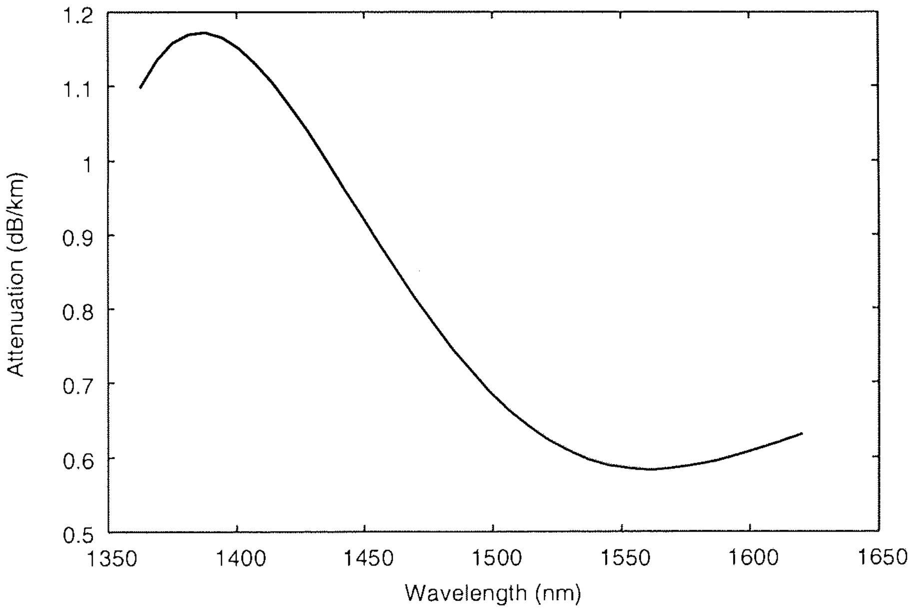

Figure A.3: Attenuation vs. wavelength of the DCF.

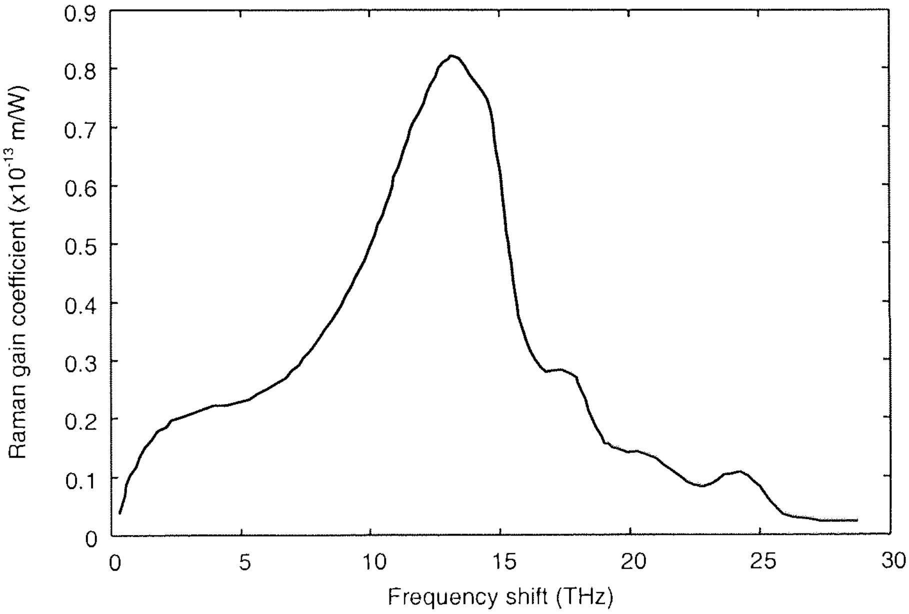

Figure A.4: Raman gain coefficient of the DCF measured at the pump wavelength of 1420 nm.

Appendix B

Split-step Fourier method

The split-step Fourier method has been proven to be the most popular numerical method to solve the nonlinear Schrödinger (NLS) equation. The method is highly efficient in terms of memory requirement and speed. The key factor to the relatively high speed of the method is the high efficiency computation of Fourier transform by using the fast Fourier transform algorithm. As for the simulator used throughout this thesis, the well maintained high performance FFTW package [80] has been exploited. Another significant advantage of the split-step Fourier method is its flexibility to extend to more complicated system simulations comprising with not only the transmission line but other lumped or distributed devices.

The method works by solving the linear and nonlinear parts of the NLS equation separately over a step Δz. Consider the normalised NLS equation (*see* the detailed derivation in Chapter 2)

$$i\frac{\partial q}{\partial Z} + \frac{d(Z)}{2}\frac{\partial^2 q}{\partial T^2} + i\frac{d_3(Z)}{6}\frac{\partial^3 q}{\partial T^3} + s(Z)|q|^2 q = -i\frac{\Gamma}{2}q, \tag{B.1}$$

the equation may be solved in two separate steps as follows:

Nonlinear step In this step, only the nonlinear part is considered. However, it is convenient to include the attenuation coefficient into this step. Thus

$$\frac{\partial q}{\partial Z} - \widehat{N}q = 0, \tag{B.2}$$

where

$$\widehat{N} = is(Z)|q|^2 - \frac{\Gamma}{2}. \tag{B.3}$$

Eq. (B.2) can be easily solved such that

$$q(Z,T) = A\exp(\widehat{N}z), \tag{B.4}$$

where A is a constant. For an advanced step $Z + \Delta Z$, the above equation yields

$$\begin{aligned} q(Z+\Delta Z) &= A\exp(\widehat{N}Z)\exp(\widehat{N}\Delta Z) \\ &= q(Z,T)\exp(\widehat{N}\Delta Z). \end{aligned} \tag{B.5}$$

Therefore, we see that the advanced step is determined by the multiplication of the previous step with $\exp(\widehat{N}Z)$.

Linear step Similarly, only the linear part is considered in this step. However, it is more convenient to work in the frequency domain to get rid off the higher order partial derivative. The Fourier transform of the linear part of the NLS equation yields

$$\frac{\partial\tilde{q}}{\partial Z} - \widehat{D}q = 0, \tag{B.6}$$

where

$$\widehat{D} = -i\frac{\omega^2}{2}d(Z) - i\frac{\omega^3}{6}d_3(Z). \tag{B.7}$$

Again, the advanced step can be determined by solving the above equation and hence

$$\tilde{q}(Z+\Delta Z,\omega) = \tilde{q}(Z,\omega)\exp(\widehat{D}\Delta Z). \tag{B.8}$$

In the integration procedure, the signal must experience both linear and nonlinear step for each ΔZ. However, the nonlinear response is very fast and does not play a critical role at the beginning but rather at the middle of the step. Therefore, the accuracy of the split-step Fourier method can be improved by carrying out each step ΔZ in the following manner. First, the first half of the linear step ($\Delta Z/2$) is carried out, followed by a full nonlinear step. Finally, the signal propagates the second half of the linear step. This increases the accuracy of the calculation to $O(\Delta Z^3)$. When several steps are calculated one after the other, the consecutive half steps can be combined to make full steps; therefore, only the first and last half linear steps are necessary.

Appropriate number of temporal mesh points and distance step size

In order to achieve a high accuracy and maintain the validity of the simulation, one may be concerned with the appropriate choice of the number of temporal mesh and the distance step size settings. The sampling frequency (f_s) is related to the mesh size ($d\tau$) and the number of mesh points as

$$f_s = \frac{1}{d\tau} = \frac{N}{2\ t_b}, \tag{B.9}$$

where N is number of temporal mesh points. For a system with pseudo-random bit sequence (PRBS), the time boundary t_b yields

$$t_b = \frac{N_{bit}}{2\ B}, \tag{B.10}$$

where N_{bit} and B are the number of bit in the PRBS and the bitrate, respectively.

In practice, the number of mesh points N must be chosen in such a way that the whole spectrum of the signal has been properly covered. As a rule of thumb the temporal mesh points $N \geq 32$ points per bit. However, it is necessary to make sure that the chosen number of mesh points allow enough spectral space to cover all signal spectra especially in WDM cases. Figures B.1 and B.2 illustrate an example of the temporal and spectral signal fields. The signal in time domain is a 64-bit PRBS with the bitrate of 40 Gb/s. The require t_b is thus 800 ps. We chose the use 32 mesh points per bit resulting in the sampling frequency of 1.28 THz which is sufficient to cover the whole spectrum of the signal as seen in Figure B.2.

The next question is what the appropriate distance step size (Δ z) should be. Considering a NLS equation with only GVD effect in the spectral domain

$$\frac{\partial \widetilde{Q}}{\partial z} = \frac{k''}{2} \omega^2 \widetilde{Q}, \tag{B.11}$$

its solution is approximately

$$\widetilde{Q} \propto e^{i\phi z}, \tag{B.12}$$

where

$$\phi = \frac{k''}{2} \omega^2. \tag{B.13}$$

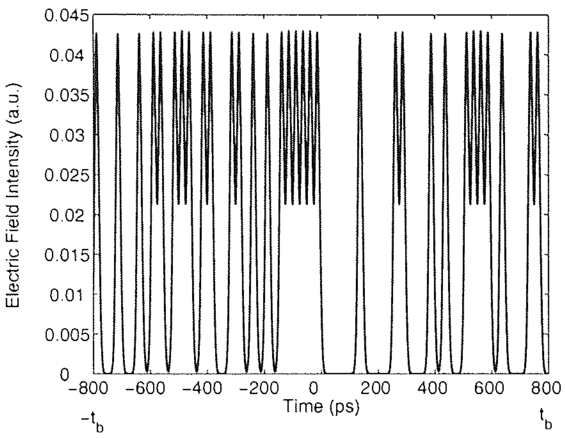

Figure B.1: Temporal signal field.

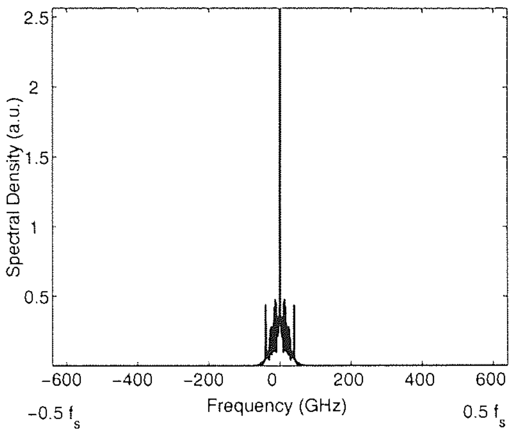

Figure B.2: Spectral signal field.

For an advanced step of the field, we thus obtain

$$\widetilde{Q}(z+\Delta z,\omega)=\widetilde{Q}(z,\omega)\exp(i\frac{k''}{2}\omega^2\Delta z). \tag{B.14}$$

To ensure that the sampling is efficient to guarantee an accuracy of the simulation, the phase rotation step must be small enough, for instance

$$\frac{k''}{2}\Delta\omega^2\Delta z \ll 1, \tag{B.15}$$

thus,

$$\Delta z \ll \frac{2}{k''\Delta\omega^2}, \tag{B.16}$$

where $\Delta\omega$ is a spectral bandwidth which is wide enough to cover the signal spectrum.

For the WDM case, the bandwidth should be $N_{ch}\Delta\omega$, where N_{ch} is number of channels in the WDM system. Therefore, the rule of thumb for an appropriate choice of Δz is

$$\Delta z \ll \frac{2}{k''N^2\Delta\omega^2}, \tag{B.17}$$

or

$$\Delta z \ll \frac{1}{2\pi^2 k''N^2\Delta f^2}, \tag{B.18}$$

where Δf is the spectral bandwidth large enough to cover a signal in one channel, or in other words, the channel spacing.

Appendix C

Modelling of some important devices in the optical transmission system

In Appendix B, the modelling of a optical fibre transmission line by using the numerical split-step Fourier method has been discussed. In this appendix, we provide a brief overview of how to implement important devices and signal monitoring instruments needed for a construction of a full transmission system simulation.

Optical transmitter

In this thesis, we are mainly concerned with the study of transmissions using return-to-zero (RZ) pulses. There are two common types of pulse shapes used in the modern optical transmission systems namely the hyperbolic secant (sech) and the Gaussian pulses. The equation used to model such pulses take the form

$$q(Z,T) = f(T)\exp(-iC_0T^2)\exp(-i\ 2\pi F_{sh}T), \tag{C.1}$$

where the first exponential term governs the linear chirp of the pulse where as the second exponential term is indicates the (normalised) frequency shift F_{sh} of the pulse relative to the reference frequency. $f(T)$ is the pulse shape and may take the form of either

$$f(T) = \sqrt{P_p}\ \mathrm{sech}\left(\frac{T}{T_0}\right) \qquad \text{for a sech pulse,} \tag{C.2}$$

or

$$f(T) = \sqrt{P_p}\exp\left(-\frac{1}{2}\frac{T^2}{T_0^2}\right) \qquad \text{for a Gaussian pulse,} \tag{C.3}$$

where P_p is the normalised peak power. The relations between T_0 and T_{FWHM} for both type of pulses can be found in Eq. (2.44).

In the optical transmission simulation, one may wish to study the effect of pulse-pulse interaction as well as the statistical evaluation of the system performance such as the Q-factor or its corresponding bit error rate (BER). An infinite random sequence may be ideal to evaluate the system BER in this case; however, it is impossible due to the limit of the simulation time and computing resources. An alternative approach is to use a random-like sequence of data so called a pseudo-random bit sequence (PRBS). The theory and discussion of the PRBS property can be found in Ref. [81]. The readers may find it useful to consult Ref. [54] for an efficient implementation of the PRBS.

Optical filter

An optical filter may be applied in the simulation of the optical transmission system by carrying out a member wise multiplication between the signal field in the spectral domain and the filter transfer function. The most common type of the optical filter used in the optical transmission system may be modelled by a (super) Gaussian function. The transfer function of the filter may take the form of

$$H(F) = \exp\left(-\frac{1}{2}\frac{F^{2m}}{F_0^{2m}}\right), \tag{C.4}$$

where $H(F)$ is the filter transfer function of the Gaussian filter with a FWHM spectral width $F_{FWHM} = 2\sqrt{\ln 2}F_0 = 1.665\ F_0$. m is an integer number indicating the filter order.

Lumped amplifier or EDFA

In practice, a lumped amplifier can be incorporate into a simulated transmission line by multiplying the signal field in the spectral domain with a constant gain. Care must be taken, however, for a realisation of noise in the EDFA. The following derivation attempts to describe the implementation of additive noise in the EDFA.

Let us begin by considering an unnormalised power

$$P = P_{norm}|q|^2, \tag{C.5}$$

where P_{norm} is a normalising parameter. The normalised field q may be written in the Fourier transform form by

$$q(T) = \frac{1}{2\pi}\int_{-\infty}^{\infty} d\Omega\ \widetilde{Q}e^{i\Omega T}, \tag{C.6}$$

where $\Omega = \omega T_{norm}$. Therefore Eq. (C.5) can be written in the form

$$P = \frac{P_{norm}}{4\pi^2}\iint_{-\infty}^{\infty} d\Omega d\Omega' \widetilde{Q}(\Omega)\widetilde{Q}^*(\Omega')e^{i(\Omega-\Omega')T}. \tag{C.7}$$

The additive noise after each amplifier is

$$\begin{aligned} P_N &= \frac{1}{2\pi}\int_{-\infty}^{\infty} d\omega N_{sp}\hbar\omega(G-1) \\ &= \frac{1}{2\pi t_{norm}}\int_{-\infty}^{\infty} d\Omega N_{sp}\hbar\omega(G-1), \end{aligned} \tag{C.8}$$

where N_{sp} and G is the spontaneous emission coefficient related to the amplifier noise figure via the relation $F = 2N_{sp}(G-1)/G \simeq 2N_{sp}$ and the amplifier gain, respectively. For the noise field, its autocorrelation is given by

$$< \widetilde{Q}(\Omega)\widetilde{Q}^*(\Omega') >= S_{norm}\delta(\Omega-\Omega'), \tag{C.9}$$

where S_{norm} is the normalised power spectral density of the noise. Substitute Eq. (C.9) into Eq. (C.7), the average power yields

$$\begin{aligned} < P > &= \frac{P_{norm}}{4\pi^2}\iint_{-\infty}^{\infty} d\Omega d\Omega' S_{norm}\delta(\Omega-\Omega')e^{i(\Omega-\Omega')T} \\ &= \frac{P_{norm}S}{4\pi^2}\int_{-\infty}^{\infty} d\Omega. \end{aligned} \tag{C.10}$$

Equate Eq. (C.10) and Eq. (C.8), we thus have

$$S_{norm} = \frac{2\pi N_{sp}\hbar\omega(G-1)}{P_{norm}t_{norm}}. \tag{C.11}$$

From the discussion in Section 5.3.3, we now arrive at the noise variance as follows:

$$\begin{aligned}\sigma^2_{norm} &= \frac{S_{norm}}{\Delta\Omega} = \frac{2\pi N_{sp}\hbar\omega(G-1)}{P_{norm}t_{norm}\Delta\Omega}, \\ &= \frac{2T_b N_{sp}\hbar\omega(G-1)}{P_{norm}t_{norm}}\end{aligned} \tag{C.12}$$

For the numerical implementation of the random noise in simulations, the reader should refer to Section 5.3.3 for more details.

Receiver

At the receiver side, the received optical signal is to be converted into an electrical signal in the form of electric current at the photo-diode. If a PIN is used, the relation between the incoming light power and the converted electric current is

$$I = \mathscr{R}P, \tag{C.13}$$

where P is the incident optical power converted into an electric current I. $\mathscr{R}$ is the responsivity of the PIN [1].

In the simulation, it is a common practice to convert the incident optical power into its corresponding current by simply taking a member wise square of the optical field.

The resulting signal in the electrical domain may be noisy due to the additive noise from optical amplifiers along the transmission line. One thus need to apply an electrical filter to suppress the noise before passing the signal to the analysis part. A Bessel filter is commonly used as the electrical filter. In this thesis, we have employed a 5th order Bessel filter with the following transfer function:

$$H(F) = \prod_{j=1}^{5}\left(\frac{z_j}{z_j - \frac{iF}{F_c}}\right), \tag{C.14}$$

where F_C is the cut-off frequency. The poles of the filter are at

$$\begin{aligned} z_j &= (1.3851 \pm i0.7201), \\ &\quad (0.9606 \pm i1.4756), \\ &\quad 1.5069. \end{aligned} \tag{C.15}$$

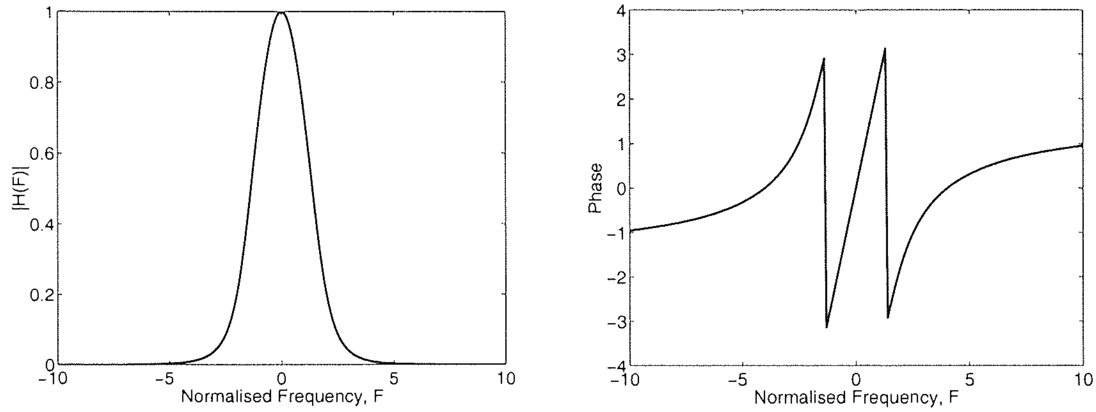

(a) (b)

Figure C.1: Example of the 5th order Bessel electrical filter. (a) The magnitude of the transfer function. (b) Phase of the transfer function.

Chirp

For single pulse simulation, we sometimes need to investigate the evolution of the average pulse chirp along the propagation. The following equation may be used to measure the chirp parameter (as defined in Eq. (C.1):

$$C = \frac{1}{2}\frac{\mathrm{Re}\left(-i\int_{-\infty}^{\infty} Tq^*\frac{dq}{dT}\,dT\right)}{\int_{-\infty}^{\infty} T^2|q|^2 dT}. \tag{C.16}$$

Note that the chirp parameter C defined in Eq. (C.1) is slightly different to what has been defined in Ref. [6] in which the chirp is define through the C_a parameter such that

$$q(Z,T) = f(T)\exp(-i\frac{C_a}{2}\frac{T^2}{T_0^2})\exp(-i\ 2\pi F_{sh}T). \tag{C.17}$$

The relation between these two definition of chirp is as follow:

$$C_a = 2T_0^2 C. \tag{C.18}$$

It is important to emphasise here that the pulsewidth T_0 is the instantaneous pulse width at a considered propagation distance.

Root mean square pulse width

In general, the FWHM pulse width is commonly used to describe the width of a pulse. However, under some circumstances in which the pulse shape becomes asymmetrical due to some effect such as the higher order nonlinearity. It is more convenient to measure the pulse width in the form of the root mean square (RMS) pulse width. The following formula may be used to numerically determine the RMS pulse width of an arbitrary pulse:

$$\sigma = [< T^2 > - < T >^2]^{\frac{1}{2}}, \tag{C.19}$$

where

$$< T^n >= \frac{\int_{-\infty}^{\infty} T^n |q(Z,T)|^2 dT}{\int_{-\infty}^{\infty} |q(Z,T)|^2 dT}. \tag{C.20}$$

Note that for a symmetrical pulse $< T >= 0$.

Timing jitter

In the single pulse simulations, one may need to estimate the timing jitter of the pulse. The evaluation of the timing jitter may be carried out by performing a sufficiently large number of runs with a different set of random additive noises. The whole process must be carried out in the electrical domain which means that the detection and filtering steps are necessary. For each run, calculate the temporal pulse shift from its centre at each considered distance by using the following equation

$$\Delta T = \frac{\int_{-\infty}^{\infty} T|q|^2 dT}{\int_{-\infty}^{\infty} |q|^2 dT}. \tag{C.21}$$

The last step is to perform an ensemble average of the temporal pulse shift to determine the timing jitter as a function of distance.

Q-factor

In optical communications, the performance criterion for digital receiver is governed by the bit-error rate (BER), which is defined as the probability of incorrect identification of a bit by the decision circuit of the receiver. For example, a BER of 1×10^{-9} corresponds to on average one error per a billion bits. In numerical simulations, BER does not seem to be a practical measure for the system performance as an extremely large number of bits are required. However, an estimate of the BER via another statistical value, so called, a Q-factor, is possible. To understand the relation between the BER and Q-factor, we shall follow the derivation of BER from the random signal with noises.

For received signals at a decision instant, the sampled value I fluctuates from bit to bit around and average value I_1 and I_0 for the corresponding "mark" and "space" bit, respectively. The decision circuit compares the sampled value with a decision level I_D and calls it "mark" bit if $I > I_D$ or "space" bit if $I < I_D$.

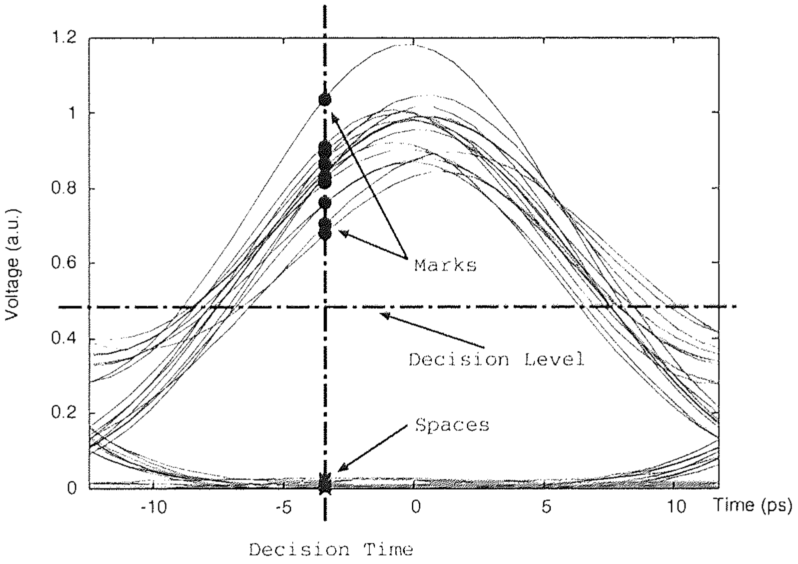

Figure C.2: Evaluation of the Q-factor from an eye diagram.

Figure C.2 shows the eye diagram of the received signal in the electrical domain after detection process. The dots represent the detected mark bits whereas the crosses are the detected space bits. An error occurs if $I < I_D$ for a mark bit or

$I > I_D$ for a space bit due to receiver noise. Thus the error probability is

$$BER = p(1)P(0/1) + p(0)P(1/0), \tag{C.22}$$

where $p(1)$ and $p(0)$ are the probabilities of receiving mark and space bits, respectively. $P(0/1)$ is the probability of deciding space when a mark is received and $P(0/1)$ is the opposite. If the mark and space bits are equally likely to occur, $p(1) = p(0) = 1/2$, thus

$$BER = \frac{1}{2}[P(0/1) + P(1/0)]. \tag{C.23}$$

In general, the noise source are assumed to follow Gaussian statistics. The error probabilities thus take the form:

$$P(0/1) = \frac{1}{\sigma_1\sqrt{2\pi}}\int_{-\infty}^{I_D} \exp\left(-\frac{(I-I_1)^2}{2\sigma_1^2}\right) dI = \frac{1}{2}\text{erfc}\left(\frac{I_1 - I_D}{\sigma_1\sqrt{2}}\right), \tag{C.24}$$

$$P(1/0) = \frac{1}{\sigma_0\sqrt{2\pi}}\int_{I_D}^{\infty} \exp\left(-\frac{(I-I_0)^2}{2\sigma_0^2}\right) dI = \frac{1}{2}\text{erfc}\left(\frac{I_D - I_0}{\sigma_0\sqrt{2}}\right), \tag{C.25}$$

where σ_1^2 and σ_0^2 are corresponding variances of the mark and space detected values. The erfc$(\cdot)$ is the complement error function defined as

$$\text{erfc}(x) = \frac{2}{\sqrt{\pi}}\int_x^{\infty} \exp(-y^2)dy. \tag{C.26}$$

By substituting Eqs. (C.24) and (C.25) in Eq. (C.23), the BER yields

$$BER = \frac{1}{4}\left(\text{erfc}\left(\frac{I_1 - I_D}{\sigma_1\sqrt{2}}\right) + \text{erfc}\left(\frac{I_D - I_0}{\sigma_0\sqrt{2}}\right)\right). \tag{C.27}$$

Eq. (C.27) suggests that the BER depends on the decision level I_D. In practice, I_D is optimised for the best BER. By minimising the BER, the optimal I_D is chosen such that

$$\frac{(I_D - I_0)^2}{2\sigma_0^2} = \frac{(I_1 - I_D)^2}{2\sigma_1^2} + \ln\left(\frac{\sigma_1}{\sigma_0}\right). \tag{C.28}$$

In most cases of practical interest, the last term of the above equation can be neglected resulting in a simple form of eqation from which the optimal I_D can be obtained as such

$$\frac{(I_D - I_0)}{\sigma_0} = \frac{(I_1 - I_D)}{\sigma_1} \equiv Q. \tag{C.29}$$

Thus the expression for I_D is

$$I_D = \frac{\sigma_0 I_1 + \sigma_1 I_0}{\sigma_0 + \sigma_1}. \tag{C.30}$$

The Q-factor can then be obtained from

$$Q = \frac{I_1 - I_0}{\sigma_1 + \sigma_0}. \tag{C.31}$$

Hence the BER with the optimal setting of the decision level is obtained as

$$BER = \frac{1}{2}\mathrm{erfc}\left(\frac{Q}{\sqrt{2}}\right) \simeq \frac{\exp(-Q^2/2)}{Q\sqrt{2\pi}}. \tag{C.32}$$

Note that the above equation is valid only when the Gaussian statistics is assumed for the noises. It is generally more convenient in the numerical simulation works to use the Q-factor as a measure of system performance because there is no need to run the simulations with a too long random signal sequence.

In numerical realisation of the Q-factor measurement in the computer simulations, the process involves signal detection and optimal decision of level and time searching. An algorithm developed by M. Eberhard and V. Mezentsev to calculate the Q-factor from a random signal sequence is to be described here.

The algorithm involves a search for the best Q value from all samples in a bit slot. This process is equivalent to a search for an optimal decision time. For each time instant in the bit slot of all bits, the following procedure is to perform to calculate the Q-factor:-

1. Record the signal amplitude and its associated bit number. For example, the first bit has the detected amplitude for this time instant of 1.2 V, thus the record should contain $(1.2, 1)$, where the first and the second members are signal amplitude and bit number, respectively.

2. Perform a sort of the obtained records by amplitude in the ascending order. The result is shown in Figure C.3. It is convenient to use the C++ "map" standard container or equivalent in other computer languages to store each record as it also has a built-in efficient sorting algorithm.

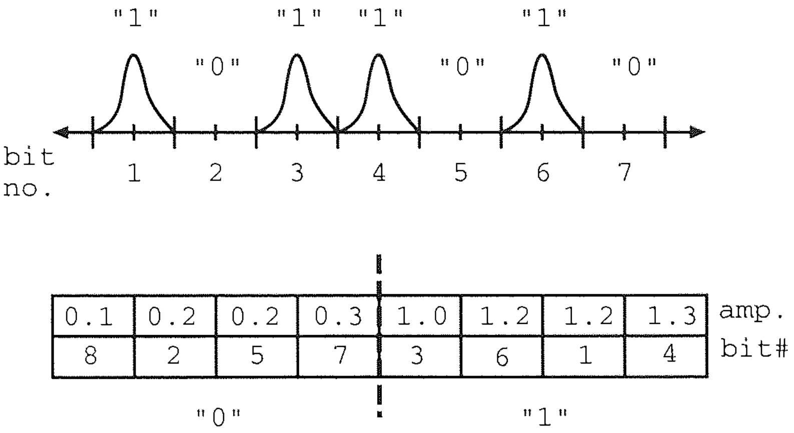

0.1	0.2	0.2	0.3	1.0	1.2	1.2	1.3	amp.
8	2	5	7	3	6	1	4	bit#

Figure C.3: Algorithm to determine the value Q-factor from a sequence of data signal.

3. As we know the number of "mark" and "space" bits, the position of optimal decision level is known instantly. The optimal decision level is represented by the dashed line in Figure C.3. Therefore all records on the left hand side of the decision level are regarded and treated as the "space" bits and vice versa for the "mark" bits.

4. Reconstruct a string of bit sequence from the recorded signals. For instance, a 8-bit sequence from the example in Figure C.3 can be reconstructed as "10110100".

5. Compare the string to the original sequence, rotate the sequence as necessary. If the match is found, calculate the Q-factor from the amplitude information obtained. If no match is found, the situation should be regarded that the Q-factor is uncomputable and return $Q = 0$.

Publications

1. N. Kurukitkoson, H. Sugahara, S.K. Turitsyn, O.N. Egorova, A.S. Kurkov, V.M. Paramonov and E.M. Dianov, "Optimization of two-stage Raman converter based on P-doped fibre: Modelling and experiment." , In the 27th European Conference on Optical Communication (ECOC01), vol. 1, paper Mo.B.3.1, page 74, Amsterdam, 2001

2. N. Kurukitkoson, H. Sugahara, S.K. Turitsyn, O.N. Egorova, A.S. Kurkov, V.M. Paramonov and E.M. Dianov, "Optimisation of two-stage Raman converter based on phosphosilicate core fibre", *Electronics Letters*, vol. 37, no. 21, page 1281, 2001

3. N. Kurukitkoson, S.K. Turitsyn, O.N. Egorova, A.S. Kurkov and E.M. Dianov,"Efficiency spectrum comparison between Germanuim and Phosphorus based Raman fibre converters", In the 2002 OSA Topical Meeting on Optical Amplifiers and Their Applications (OAA), paper OMC4, Vancouver, Canada, 2002

4. N. Kurukitkoson, S.K. Turitsyn,O.N. Egorova, A.S. Kurkov and E.M. Dianov, "Raman fibre laser based on P-doped fibres", In the Rank Prize Funds Mini-symposium on Nonlinear Dynamics of Lasers, UK, 2002

5. N. Kurukitkoson, S.K. Turitsyn,O.N. Egorova, A.S. Kurkov and E.M. Dianov, "Raman fibre laser based on Phosphorus doped fibres", In the 56th Scottish Universities Summer School in Physics: Ultrafast Photonics, UK, 2002

6. E.M. Dianov, A.S. Kurkov, O.I. Medvedkov, V.M. Paramonov, O.N. Egorova, N. Kurukitkoson and S.K. Turitsyn, "Raman fiber source for 1.6 – 1.75 μm spectral region", In the Optical Fiber Conference 2003 (OFC2003), paper MF26, Atlanta, USA, 2003

7. E.M. Dianov, A.S. Kurkov, O.I. Medvedkov, V.M. Paramonov, O.N. Egorova, N. Kurukitkoson and S.K. Turitsyn, "Raman fiber source for 1.6 – 1.75 μm spectral region", *International Journal on Laser Physics*, vol. 13, no. 3, page 397, 2003

8. N. Kurukitkoson, S.K. Turitsyn, A.S. Kurkov and E.M. Dianov. "Multiple output wavelength composite Raman fibre converter", In the 12th International Laser Physics Workshop (LPHYS'03), paper 4.4.2, Hamburg, Germany, 2003

9. N. Kurukitkoson, S.K. Turitsyn, A.S. Kurkov and E.M. Dianov. "Multiple output wavelength composite Raman fibre converter", to be published in *International Journal on Laser Physics*, 2004

10. J.D. Ania-Castañón, I.O. Nasieva, N. Kurukitkoson, S.K. Turitsyn, C. Borsier and E. Pincemin, "Nonlinearity management in hybrid amplification systems", In the 2004 OSA Topical Meeting on Nonlinear Guided Waves and Their Applications, Toronto, Canada, 2004

11. J.D. Ania-Castañón, I.O. Nasieva, N. Kurukitkoson, S.K. Turitsyn, C. Borsier and E. Pincemin, "Nonlinearity management in fiber transmission systems with hybrid amplification", to be published in *Optics Communication*, 2004

Bibliography

[1] J. M. Senior. *Optical fiber communication: principle and practice.* Prentice Hall, 2nd edition, 1992.

[2] I. P. Kaminow and T.L. Koch. *Optical fiber telecommunication IIIA*. Academic Press, MA, 1997.

[3] G. P. Agrawal. *Fiber-Optic Communication Systems.* John Wiley & Suns, New York, 1997.

[4] K.C. Kao and G.A. Hockham. Dielectric-fiber surface waveguides for optical frequencies. *Proceeding of the IEEE*, 133:1151, 1966.

[5] F.P. Kapron, D.B. Keck, and R.D. Maurer. Radiation losses in glass optical waveguides. *Applied Physics Letters*, 17:423, 1970.

[6] G. P. Agrawal. *Nonlinear fiber optics.* Academic Press, London, 2 edition, 1995.

[7] E. Desurvire. *Erbium-doped Fiber Amplifiers.* Wiley Inter-Science Publications, New York, 1994.

[8] M. I. Hayee and A. E. Willner. NRZ versus RZ in 10-40-Gb/s dispersion-managed WDM transmission systems. *IEEE Photonics Technology Letters*, 11(8):991, 1999.

[9] K. Ennser and K. Petermann. Performance of RZ- versus NRZ-transmission on standard single- mode fibers. *IEEE Photonics Technology Letters*, 8(3):443, 1996.

[10] A. Hasegawa and F. Tappert. Transmission of stationary nonlinear optical pulses in dispersive dielectric fibers. I. Anomalous dispersion. *Applied Physics Letters*, 23:142, 1973.

[11] J.P. Gordon and H. A. Haus. Random walk of coherently amplified solitons in optical fiber transmission. *Optics Letters*, 11:665, 1986.

[12] P.L. Chu and C. Desem. Mutual interaction between soliton of unequal amplitudes in optical fibres. *Electronics Letters*, 21:1133, 1985.

[13] A. Mecozzi, J.D. Moores, H. A. Haus, and Y Lai. Soliton transmission control. *Optics Letters*, 16:1841, 1991.

[14] L.F. Mollenauer, J.P. Gordon, and S.G Evangelides. The sliding-frequency guiding filter: an improved form of soliton jitter control. *Optics Letters*, 17:1575, 1992.

[15] M. Nakazawa, E. Yamada, H. Kubota, and H. Suzuki. 10 Gbit/s soliton data transmission over one million kilometers. *Electronics Letters*, 27:1270, 1991.

[16] S. Wabnitz. Suppression of soliton interactions by phase modulation. *Electronics Letters*, 29:1711, 1993.

[17] N. J. Smith, N. J. Doran, W. Forysiak, and F. M. Knox. Soliton transmission using periodic dispersion compensation. *Journal of Lightwave Technology*, 15(10):1808, 1997.

[18] W. Forysiak, K.J. Blow, and N. J. Doran. Reduction of Gordon-Haus jitter by post-transmission dispersion compensation. *Electronics Letters*, 29:1225, 1993.

[19] L.J. Richardson, W. Forysiak, and N. J. Doran. Dispersion-managed soliton propagation in short-period dispersion maps. *Optics Letters*, 25:1010, 2000.

[20] T. Hirooka, T. Nakada, and A. Hasegawa. Feasibility of densely dispersion managed soliton transmission at 160 Gb/s. *IEEE Photonics Technology Letters*, 12(6):633, 2000.

[21] S Boscolo, S. K. Turitsyn, and K.J. Blow. All-optical passive regeneration of 40 Gbit/s soliton data stream using dispersion management and in-line NOLMs. *Electronics Letters*, 37:112, 2001.

[22] T. Ito, K. Fukuchi, Y. Inada, T. Tsuzaki, M. Harumoto, M. Kakui, and K. Fuji. 3.2 Tb/s 1,500 km WDM transmission experiment using 64 nm hybrid repeater amplifiers. In *Optical Fiber Conference*, page PD24, Baltimore, 2000.

[23] T. Tanaka, N. Shimojoh, T. Naito, H. Nakamoto, I. Yokota, T. Ueki, A. Suguyama, and M. Suyama. 2.1-Tbit/s WDM transmission over 7,221 km with 80-km repeater spacing. In *European Conference on Optical Communication*, page PD1.8, Munich, 2000.

[24] S. K. Turitsyn, M. P. Fedoruk, W. Forysiak, and N. J. Doran. Dispersion-Management in fiber communication lines using Raman Amplification. *Optics Communications*, 170(1-3):23, 1999.

[25] http://www.corning.com.

[26] L. du Mouza, G. Le Meur, H. Mardoyan, E. Seve, S. Cussat-Blanc, D. Hamoir, C. Martinelli, D. Bayart, F. Raineri, L. Pierre, B. Dany, O. Leclerc, J. P. Hamaide, L. A. de Montmorillon, F. Beaumont, P. Sillard, P. Nouchi, A. Hugbart, R. Uhel, and G. Grandpierre. 1.28 Tbit/s (32 x 40 Gbit/s) WDM transmission over 2400 km of TeraLight (TM)/Reverse TeraLight (c) fibres using distributed all-Raman amplification. *Electronics Letters*, 37(21):1300, 2001.

[27] B. Zhu, L. Leng, L. E. Nelson, Y. Qian, L. Cowsar, S. Stulz, C. Doerr, L. Stulz, S. Chandrasekhar, S. Radic, D. Vengsarkar, Z. Chen, J. Park, K. S. Feder, H. Thiele, J. Bromage, L. Gruner-Nielsen, and S. Knudsen. 3.08 Tbit/s (77 x 42.7 Gbit/s) WDM transmission over 1200 km fibre with 180 km repeater spacing using dual C- and L-band hybrid Raman/Erbium-doped inline amplifiers. *Electronics Letters*, 37(13):844, 2001.

[28] M. N. Islam. *Raman amplifiers for telecommunications 1*, volume 1. Springer-Verlag, New York, 2003.

[29] D. Marcuse. *Light Transmission Optics.* Van Nostrand Reinhold, New York, 1982.

[30] K. R. Demarest. *Engineering Electromagnetics.* Prentice-Hall, USA, 1998.

[31] A. Hasegawa and Y. Kodama. *Solitons in optical communications.* Clarendon Press, Oxford, 1995.

[32] Y. Emori, K. Tanaka, and S. Namiki. 100nm bandwidth flat-gain Raman amplifiers pumped and gain- equalised by 12-wavelength-channel WDM laser diode unit. *Electronics Letters*, 35(16):1355, 1999.

[33] S. Namiki and Y. Emori. Ultrabroad-band Raman amplifiers pumped and gain-equalized by wavelength-division-multiplexed high-power laser diodes. *IEEE Journal of Selected Topics in Quantum Electronics*, 7(1):3, 2001.

[34] M. N. Islam. Raman amplifiers for telecommunications. *IEEE Journal of Selected Topics in Quantum Electronics*, 8(3):548, 2002.

[35] Nobel foundation. *Les Prix Nobel.* Nobel foundation, Oslo, 1930.

[36] The Nobel prize in Physics 1930: The presentation speech. http://www.nobel.se/physics/laureates/1930/press.html, 2003.

[37] H. A. Szymanski. *Raman spectroscopy, theory and practice.* Plenum, New York, 1970.

[38] R. H. Stolen, E. P. Ippen, and A.R. Tynes. Raman oscillation in glass optical waveguide. *Applied Physics Letters*, 20(2):62, 1972.

[39] R. H. Stolen and E. P. Ippen. Raman gain in glass optical waveguides. *Applied Physics Letters*, 22(6):276, 1973.

[40] A. Bjarklev. *Optical fiber amplifiers: design and system application.* Artech House, 1993.

[41] I. K. Ilev, R. W. Waynant, H. Kumagai, and K. Midorikawa. Double-pass fiber Raman laser - A powerful and widely tunable in the ultraviolet, visible, and near-infrared fiber Raman laser for biomedical investigations. *IEEE Journal of Selected Topics in Quantum Electronics*, 5(4):1013, 1999.

[42] V. I. Karpov, E. M. Dianov, V. M. Paramonov, O. I. Medvedkov, M. M. Bubnov, S. L. Semyonov, S. A. Vasiliev, V. N. Protopopov, O. N. Egorova, V. F. Hopin, A. N. Guryanov, M. P. Bachynski, and W. R. L. Clements. Laser-diode-pumped phosphosilicate-fiber Raman laser with an output power of 1 W at 1.48 μm. *Optics Letters*, 24(13):887, 1999.

[43] K. S. Repasky, L. Meng, J. K. Brasseur, J. L. Carlsten, and R. C. Swanson. High-efficiency, continuous-wave Raman lasers. *Journal of the Optical Society of America B-Optical Physics*, 16(5):717, 1999.

[44] E. Garmire, F. Pandarese, and C.H. Townes. Coherently driven molecular vibrations and light modulation. *Physical Review Letters*, 11:160, 1963.

[45] R. W. Boyd. *Nonlinear Optics*. Academic Press, 1992.

[46] D. Hollenbeck and C. D. Cantrell. Multiple-vibrational-mode model for fiber-optic Raman gain spectrum and response function. *Journal of the Optical Society of America B-Optical Physics*, 19(12):2886, 2002.

[47] R. H. Stolen. Nonliearity in fiber transmission. *Proceeding of the IEEE*, 68(10):1232, 1980.

[48] W.P. Urquhart and P.J. Laybourn. Effective core area for stimulated Raman scattering in single-mode optical fibres. *IEE Proceedings, optoelectronics*, 32(4):201, 1985.

[49] K.J. Blow and D. Wood. Theoretical description of transient stimulated Raman scattering in optical fibers. *IEEE Journal of Quantum Electronics*, 25(12):2665, 1989.

[50] R. G. Smith. Optical power handing capacity of low loss optical fibers as determined by stimulated Raman and Brillouin scattering. *Applied Optics*, 11(11):2489, 1972.

[51] D. V. Gapontsev, S. V. Chernikov, and J. R. Taylor. Fibre Raman amplifiers for broadband operation at 1.3 μm. *Optics Communications*, 166(1-6):85, 1999.

[52] S. A. E. Lewis, S. V. Chernikov, and J. R. Taylor. Broadband high-gain dispersion compensating Raman amplifier. *Electronics Letters*, 36(16):1355, 2000.

[53] N. S. Kim, M. Prabhu, C. Li, J. Song, and K. Ueda. 1239/1484 nm cascaded phosphosilicate Raman fiber laser with CW output power of 1.36 W at 1484 nm pumped by CWYb-doped double- clad fiber laser at 1064 nm and spectral continuum generation. *Optics Communications*, 176(1-3):219, 2000.

[54] W.H. Press, S.A. Teukolsky, W. Vetterling, and B.P. Flannery. *Numerical recipes in C: the art of scientific computing*. Cambridge University Press, 1992.

[55] E. M. Dianov, I. A. Bufetov, M. M. Bubnov, M. V. Grekov, S. A. Vasiliev, and O. I. Medvedkov. Three-cascaded 1407-nm Raman laser based on phosphorus-doped silica fiber. *Optics Letters*, 25(6):402, 2000.

[56] N. Kurukitkoson, H. Sugahara, S. K. Turitsyn, O. N. Egorova, A. S. Kurkov, V. M. Paramonov, and E. M. Dianov. Optimization of two-stage Raman converter based on P-doped fibre: Modelling and Experiment. In *ECOC01*, volume 1, page 74, Amsterdam, 2001.

[57] N. Kurukitkoson, H. Sugahara, S. K. Turitsyn, O. N. Egorova, A. S. Kurkov, V. M. Paramonov, and E. M. Dianov. Optimisation of two-stage Raman converter based on phosphosilicate core fibre: modelling and experiment. *Electronics Letters*, 37(21):1281, 2001.

[58] N. Kurukitkoson, S. K. Turitsyn, O. N. Egorova, A. S. Kurkov, and E. M. Dianov. Efficiency spectrum comparison between Germanium and Phosphorus based Raman fiber converters. In *2002 OSA Topical Meeting on Optical Amplifiers and Their Applications*, volume 1, page OMC4, Vancouver, 2002.

[59] E. M. Dianov and A.M. Prokhorov. Medium-power CW Raman fiber lasers. *IEEE Journal of Selected Topics in Quantum Electronics*, 6:1022, 2000.

[60] E. M. Dianov, A. S. Kurkov, O. I. Medvedkov, V. M. Paramonov, O. N. Egorova, N. Kurukitkoson, and S. K. Turitsyn. Raman fiber source for 1.6-1.75 μm spectral region. In *Optical Fiber Conference*, page MF26, Atlanta, 2003.

[61] E. M. Dianov, A. S. Kurkov, O. I. Medvedkov, V. M. Paramonov, O. N. Egorova, N. Kurukitkoson, and S. K. Turitsyn. Raman fiber source for 1.6-1.75 μm spectral region. *International Journal on Laser Physics*, 13(3):397, 2003.

[62] J. D. Ania-Castanon, S. M. Kobtsev, A. A. Pustovskikh, and S. K. Turitsyn. Simple design method for gain-flattened three-pump Raman amplifiers, 2002.

[63] M. D. Mermelstein, C. Horn, Z. Huang, M. Luvalle, J. C. Bouteiller, C. Headley, and B. J. Eggleton. Configurability of a three-wavelength Raman fiber laser for gain ripple minimization and power partitioning. In *Optical Fiber Conference 2002*, page TuJ2, 2002.

[64] X. Normandin, F. Leplingard, E. Bourova, C. Leclere, T. Lopez, J.J. Guerin, and D. Bayart. Experiment assessment of phospho-silicate fibers for three-wavelength (1427 nm, 1455 nm, 1480 nm) reconfigurable Raman lasers. In *Optical Fiber Conference 2002*, page TuB2, 2002.

[65] N. Kurukitkoson, S. K. Turitsyn, A. S. Kurkov, and E. M. Dianov. Multiple output wavelength composite Raman fibre converter. In *the 12th International Laser Physics Workshop*, page 4.4.2, Hamburg, 2003.

[66] N. Kurukitkoson, S. K. Turitsyn, A. S. Kurkov, and E. M. Dianov. Multiple output wavelength composite Raman fibre converter. *to be published in International Journal on Laser Physics*, 2004.

[67] L. Helczynski and A. Berntson. Comparison of EDFA and bidirectionally pumped Raman amplifier in a 40-Gb/s RZ transmission system. *IEEE Photonics Technology Letters*, 13(7):669, 2001.

[68] D. Marcuse. An alternative derivation of the Gordon-Haus effect. *Journal of Lightwave Technology*, 10(2):273, 1992.

[69] K. Ennser, R. I. Laming, and M. N. Zervas. Analysis of 40 Gb/s TDM-transmission over embedded standard fiber employing chirped fiber grating dispersion compensators. *Journal of Lightwave Technology*, 16(5):807, 1998.

[70] D. Breuer, H.J. Ehrke, F. Kuppers, R. Ludwig, K. Petermann, H.G. Weber, and K. Weich. Unrepeated 40-Gb/s RZ single-channel transmission at 1.55 μm using various fiber types. *IEEE Photonics Technology Letters*, 10(6):822, 1998.

[71] B. Zhu, L. Leng, L.E. Nelson, Y. Qian, L. Cowsar, S. Stulz, C. Doerr, L. Stulz, S. Chandrasekha, S. Radic, D. Vengsakar, Z. Chen, J. Park, K.S. Feder, H. Thiele, J. Bromage, L. Gruner-Nielsen, and S. N. Knudsen. 3.08 Tbit/s (77 x 42.7 Gbit/s) WDM transmission over 1200 km fibre with 100 km repeater spacing using dual C- and L-band hybrid Raman/Erbium-doped inline amplifiers. *Electronics Letters*, 37(13), 2001.

[72] S. Park, A.H. Gnauck, J.M. Wiesenfeld, and L.D. Garrett. 40-Gb/s transmission over multiple 120-km spans of conventional single-mode fiber using highly dispersed pulse. *IEEE Photonics Technology Letters*, 12(8):1085, 2000.

[73] J. Cai, M. Nissov, C. R. Davidson, A.N. Pilipetskii, G. Mohs, H. Li, Y. Cai, E.A. Golovchenko, A. J. Lucero, D.G. Foursa, and N. S. Bergano. Long-haul 40 Gb/s DWDM transmission with aggregate capacities exceeding 1 Tb/s. *Journal of Lightwave Technology*, 20(12):2247, 2002.

[74] J. D. Ania-Castanon, I.O. Nasieva, N. Kurukitkoson, S. K. Turitsyn, C. Borsier, and E. Pincemin. Nonlinearity management in hybrid amplification systems. In *the 2004 OSA Topical Meeting on Nonlinear Guided Waves and Their Applications*, Toronto, 2004.

[75] J. D. Ania-Castanon, I.O. Nasieva, N. Kurukitkoson, S. K. Turitsyn, C. Borsier, and E. Pincemin. Nonlinearity management in fiber transmission systems with hybrid amplification. *to be published in Optics Communications*, 2004.

[76] R. H. Stolen and J.E. Bjorkholm. Parametric amplification and frequency conversion in optical fibers. *IEEE Journal of Quantum Electronics*, QE-18(7):1062, 1982.

[77] G. Cappellini and S. Trillo. Third-order three-wave mixing in single-mode fibers: exact solution and spatial instability effects. *Journal of the Optical Society of America B-Optical Physics*, 8(4):824, 1991.

[78] S. Trillo and S. Wabnitz. Parametric and Raman amplification in birefringent fibers. *Journal of the Optical Society of America B-Optical Physics*, 9(7):1061, 1992.

[79] T. Sylvestre, H. Maillotte, and E. Lantz. Raman-assisted parametric frequency conversion in a normally dispersive single-mode fiber. *Optics Letters*, 24(22):1561, 1999.

[80] M Frigo and S.G. Johnson. FFTW: An adaptive software architecture for the FFT. *IEEE International conference on Acoustics Speech and Signal Processing*, page 1381, 1998.

[81] F.J. MacWilliams and N.J. Sloane. Pseudo-Random sequences and arrays. *Proceeding of the IEEE*, 64(12):1715, 1976.

[82] A. A. Demidov, A. N. Starodumov, X. Li, A. Martinez-Rios, and H. Po. Three-wavelength Raman fiber laser with reliable dynamic control. *Optics Letters*, 28(17):1540, 2003.

[83] X. P. Zheng, F. F. Feng, Y. B. Ye, H. Y. Zhang, and Y. H. Li. Analysis in distributed Raman amplification. *Optics Communications*, 207(1-6):321, 2002.

[84] M. Rini, I. Cristiani, V. Degiorgio, A. S. Kurkov, and V. M. Paramonov. Experimental and numerical optimization of a fiber Raman lasers. *Optics Communications*, 203(1-2):139, 2002.

[85] J. P. Laude. *DWDM Fundamentals, Components, and Applications*. Artech House, 2002.

[86] N. Kurukitkoson, S. K. Turitsyn, O. N. Egorova, A. S. Kurkov, and E. M. Dianov. Raman fibre lasers based on Phosphorus doped fibres. In *the 56th Scottish Universities Summer School in Physics: Ultrafast Photonics*, UK, 2002.

[87] N. Kurukitkoson, S. K. Turitsyn, O. N. Egorova, A. S. Kurkov, and E. M. Dianov. Raman fibre laser based on P-doped fibre. In *the Rank Prize Funds Mini-symposium on Nonlinear Dynamics of Lasers*, UK, 2002.

[88] C. Headley. Configurable multiple-wavelength all-fiber laser for efficient stable Raman amplification. In *Optical Fiber Conference 2002*, page TuB1, 2002.

[89] W. Zhang, J. Peng, X. Liu, and C. Fan. An analytical expression of equivalent noise figure for distributed fiber Raman amplifiers with Rayleigh scattering. *Optics Communications*, 199(1-4):231, 2001.

[90] M. Yan, J. Chen, W. Jiang, J. Li, Jun Chen, and X. Li. Pump depletion induced noise and crosstalk in distributed optical fiber Raman amplifiers. *IEEE Photonics Technology Letters*, 13(7):651, 2001.

[91] S. H. Wang and C. C. Fan. Distributed fiber Raman amplifiers: analytical expression of noise characteristics under complex conditions. *Optics Communications*, 198(1-3):65, 2001.

[92] S. Wabnitz and G. Le Meur. Nonlinear and noise limitations in dispersion-managed soliton wavelength-division multiplexing transmissions with distributed Raman amplification. *Optics Letters*, 26(11):777, 2001.

[93] V. E. Perlin and H. G. Winful. Distributed feedback fiber Raman laser. *IEEE Journal of Quantum Electronics*, 37(1):38, 2001.

[94] T. Okuno, T. Tsuzaki, and M. Nishimura. Novel optical hybrid line configuration for quasi-lossless transmission by distributed Raman amplification. *IEEE Photonics Technology Letters*, 13(8):806, 2001.

[95] I. Morita, K. Tanaka, and N. Edagawa. Benefit of Raman amplification in ultra-long-distance 40 Gbit/s- based WDM transmission using dispersion-flattened fibre span. *Electronics Letters*, 37(8):507, 2001.

[96] D. Chang, S. Lim, M.Y. Jeon, K.H. Kim, and T. Park. Cascaded Raman fibre laser for stable dual wavelength operation. *Electronics Letters*, 37(12), 2001.

[97] H. Suzuki, J. Kani, H. Masuda, N. Takachio, K. Iwatsuki, Y. Tada, and M. Sumida. 1-Tb/s (100 x 10 Gb/s) super-dense WDM transmission with 25-GHz channel spacing in the zero-dispersion region employing distributed Raman amplification technology. *IEEE Photonics Technology Letters*, 12(7):903, 2000.

[98] H. S. Seo and K. Oh. Optimization of silica fiber Raman amplifier using the Raman frequency modeling for an arbitrary GeO_2 concentration in the core. *Optics Communications*, 181(1-3):145, 2000.

[99] K. Rottwitt, J. Bromage, M. Du, and A. J. Stentz. Design of distributed Raman amplifiers. In *ECOC 2000*, volume 2, page 67, Munich, Germany, 2000.

[100] M. Rini, I. Cristiani, and V. Degiorgio. Numerical modeling and optimization of cascaded CW Raman fiber lasers. *IEEE Journal of Quantum Electronics*, 36(10):1117, 2000.

[101] Y. Qian, J. H. Povlsen, S. N. Knudsen, and L. Gruner-Nielsen. Analysis and characterization of dispersion compensating fibers in fiber Raman amplification. In *Optical Amplifiers and Their Applications*, page OMB6, Quebec, Canada, 2000.

[102] M. Prabhu, N. S. Kim, and K. Ueda. Ultra-broadband CW supercontinuum generation centered at 1483.4 nm from Brillouin/Raman fiber laser. *Japanese Journal of Applied Physics Part 2-Letters*, 39(4A):L291, 2000.

[103] M. Prabhu, N. S. Kim, and K. Ueda. Output characteristics of high-power continuous wave Raman fiber laser at 1239 nm using phosphosilicate fiber. *Optical Review*, 7(4):297, 2000.

[104] M. Prabhu, N. S. Kim, L. Jianren, and K. Ueda. Simultaneous two-color CW Raman fiber laser with maximum output power of 1.05 W/1239 nm and 0.95 W/1484 nm using phosphosilicate fiber. *Optics Communications*, 182(4-6):305, 2000.

[105] M. Prabhu, N. S. Kim, and K. Ueda. Simultaneous double-color continuous wave Raman fiber laser at 1239 nm and 1484 nm using phosphosilicate fiber. *Optical Review*, 7(4):277, 2000.

[106] B. Min, W. J. Lee, S. Bae, and N. Park. Efficiency improved modeling of Raman fiber amplifiers based on average power analysis. In *Fifth Optoelectronics and Communications Conference (OECC 2000)*, Chiba, Japan, 2000.

[107] A. Mathur, M. Ziari, M. Fisher, and J. Neff. Over 1W fibre-coupled power from single semiconductor source for pumping of Raman fibre amplifiers and Erbium-doped fibre amplifiers. *Electronics Letters*, 36(5):410, 2000.

[108] F. Matera and M. Settembre. Role of Q-factor and of time jitter in the performance evaluation of optically amplified transmission systems. *IEEE Journal of Selected Topics in Quantum Electronics*, 6(2):308, 2000.

[109] S. A. E. Lewis, S. V. Chernikov, and J. R. Taylor. Fibre-optic tunable CW Raman laser operating around 1.3 μm. *Optics Communications*, 182(4-6):403, 2000.

[110] S. A. E. Lewis, S. V. Chernikov, and J. R. Taylor. Characterization of double Rayleigh scatter noise in Raman amplifiers. *IEEE Photonics Technology Letters*, 12(5):528, 2000.

[111] F. Koch, S. V. Chernikov, S. A. E. Lewis, and J. R. Taylor. Characterisation of single stage, dual-pumped Raman fibre amplifiers for different gain fibre lengths. *Electronics Letters*, 36(4):347, 2000.

[112] N. S. Kim, M. Prabhu, C. Li, J. Song, D. Shen, K. Ueda, and H. J. Kong. Ge-doped Raman fiber amplifier with enhanced signal-to-noise ratio using second Stokes control pulses. *Applied Physics B-Lasers and Optics*, 70(2):169, 2000.

[113] N. S. Kim, M. Prabhu, C. Li, J. Song, and K. Ueda. Output characteristics of P-doped Raman fiber laser at 1484 nm with 2.11W maximum output power pumped by CW 1064 nm Yb-doped double-clad fiber laser. *Japanese Journal of Applied Physics Part 1-Regular Papers Short Notes & Review Papers*, 39(11):6264, 2000.

[114] H. A. Haus. Noise figure definition valid from RF to optical frequencies. *IEEE Journal of Selected Topics in Quantum Electronics*, 6(2):240, 2000.

[115] J. W. Goodman. *Statistical Optics*. CA, 2000.

[116] O.N. Egorova, M. M. Bubnov, I. A. Bufetov, E. M. Dianov, A.N. Guryanov, P.F. Khopin, S.L. Semjonov, and A.V. Shubin. Phosphosilicate-core single mode fibers intended for use as active medium of Raman lasers and amplifiers. In *Photonics East, SPIE*, Boston, MA, 2000.

[117] J. S. Wey, D. L. Butler, M. F. Van Leeuwen, L. G. Joneckis, and J. Goldhar. Crosstalk bandwidth in backward pumped fiber Raman amplifiers. *IEEE Photonics Technology Letters*, 11(11):1417, 1999.

[118] C.M. Weinert, R. Ludwig, W. Pieper, H.G. Weber, D. Breuer, K. Petermann, and F. Kuppers. 40 Gb/s and 4 x 40 Gb/s TDM/WDM standard fiber transmission. *Journal of Lightwave Technology*, 17(11):2276, 1999.

[119] A. Sahara, H. Kubota, and M. Nakazawa. Comparison of the dispersion allocated WDM (10 Gbit/s x 10 channels) optical soliton and NRZ systems using a Q map. *Optics Communications*, 160(1-3):139, 1999.

[120] M. Nissov, K. Rottwitt, H. D. Kidorf, and M. X. Ma. Rayleigh crosstalk in long cascades of distributed unsaturated Raman amplifiers. *Electronics Letters*, 35(12):997, 1999.

[121] H. Masuda and S. Kawai. Wide-band and gain-flattened hybrid fiber amplifier consisting of an EDFA and a multiwavelength pumped Raman amplifier. *IEEE Photonics Technology Letters*, 11(6):647, 1999.

[122] M.E. Lines, W.A. Reed, D.J. Di Giovanni, and J.R. Hamblin. Explaination of anomalous loss in high delta single mode fibres. *Electronics Letters*, 35(12):1009, 1999.

[123] S. A. E. Lewis, S. V. Chernikov, and J. R. Taylor. Triple wavelength pumped silica-fibre Raman amplifiers with 114nm bandwidth. *Electronics Letters*, 35(20):1761, 1999.

[124] S. A. E. Lewis, S. V. Chernikov, and J. R. Taylor. Gain and saturation characteristics of dual-wavelength-pumped silica-fibre Raman amplifiers. *Electronics Letters*, 35(14):1178, 1999.

[125] S. A. E. Lewis, S. V. Chernikov, and J. R. Taylor. Gain saturation in silica-fibre Raman amplifier. *Electronics Letters*, 35(11):923, 1999.

[126] H. Kidorf, K. Rottwitt, M. Nissov, M. Ma, and E. Rabarijaona. Pump interactions in a 100-nm bandwidth Raman amplifier. *IEEE Photonics Technology Letters*, 11(5):530, 1999.

[127] A.K. Atieh, P. Myslinski, J. Chrostowski, and P. Galko. Measuring the Raman time constant for soliton pulses in standard single-mode fiber. *Journal of Lightwave Technology*, 17(2):216, 1999.

[128] M. J. Ablowitz, G. Biondini, S. Chakravarty, and R. Horne. A Comparison Between Lumped and Distributed Filter Models in Wavelength-Division Multiplexed Soliton Systems. *Optics Communications*, 172(1-6):211, 1999.

[129] T. Okamawari, A. Maruta, and Y. Kodama. Reduction of Gordon-Haus jitter in a dispersion compensated optical transmission system: analysis. *Optics Communications*, 149:261, 1998.

[130] J. H. B. Nijhof, N. J. Doran, W. Forysiak, and A. Berntson. Energy enhancement of dispersion-managed solitons and WDM. *Electronics Letters*, 34(5):481, 1998.

[131] H. Masuda, S. Kawai, K. Suzuki, and K. Aida. Ultrawide 75-nm 3-dB gainband optical amplification with Erbium-doped fluoride fiber amplifiers and distributed Raman amplifiers. *IEEE Photonics Technology Letters*, 10(4):516, 1998.

[132] S. Kumar, M. Wald, F. Lederer, and A. Hasegawa. Soliton interaction in strongly dispersion-managed optical fibers. *Optics Letters*, 23(13):1019, 1998.

[133] P. B. Hansen, G. Jacobovitz-Veselka, L. Gruner-Nielsen, and A. J. Stentz. Raman amplification for loss compensation in dispersion compensating fibre modules. *Electronics Letters*, 34(11):1136, 1998.

[134] P. B. Hansen, L. Eskildsen, A. J. Stentz, T. A. Strasser, J. Judkins, J. J. DeMarco, R. Pedrazzani, and D. J. DiGiovanni. Rayleigh scattering limitations in distributed Raman pre- amplifiers. *IEEE Photonics Technology Letters*, 10(1):159, 1998.

[135] G. E. Carlson. *Signal and Linear System Analysis.* John Wiley & Sons, USA, 2nd edition, 1998.

[136] D. Breuer, K. Obermann, and K. Petermann. Comparison of N x 40 Gb/s and 4N x 10 Gb/s WDM transmission over standard single-mode fiber at 1.55 μm. *IEEE Photonics Technology Letters*, 10(12):1793, 1998.

[137] A. V. Oppenheim, A.S. Willsky, and S. H. Nawab. *Signal & Systems.* Prentice Hall, 2nd edition, 1997.

[138] M. Matsumoto and H. A. Haus. Stretched-pulse optical fiber communications. *IEEE Photonics Technology Letters*, 9(6):785, 1997.

[139] B. A. Malomed, F. Matera, and M. Settembre. Performance of optically amplified dispersion-compensated links: reduction of the time jitter for return to zero signals. *Optics Communications*, 143(4-6):193, 1997.

[140] S. Kumar and A. Hasegawa. Quasi-soliton propagation in dispersion-managed optical fibers. *Optics Letters*, 22(6):372, 1997.

[141] S.R. Chinn. Analysis of counter-pumped small-signal fibre Raman amplifiers. *Electronics Letters*, 33(7):607, 1997.

[142] D. Breuer and K. Petermann. Comparison of NRZ- and RZ-modulation format for 40-Gb/s TDM standard-fiber systems. *IEEE Photonics Technology Letters*, 9(3):398, 1997.

[143] P. Wan and J. Conradi. Impact of double Rayleigh backscatter noise on digital and analog fiber systems. *Journal of Lightwave Technology*, 14(3):288, 1996.

[144] G. Tartwijk, R. Essiambre, and G. P. Agrawal. Dispersion-tailored active-fiber solitons. *Optics Letters*, 21(24):1978, 1996.

[145] E. G. Sauter. *Nonlinear optics.* John Wiley&Sons, USA, 1996.

[146] A. Sahara, H. Kubota, and M. Nakazawa. Q-factor contour mapping for evaluation of optical transmission systems: Soliton against NRZ against RZ pulse at zero group velocity dispersion. *Electronics Letters*, 32(10):915, 1996.

[147] F. Matera and M. Settembre. Comparison of the performance of optically amplified transmission systems. *Journal of Lightwave Technology*, 14(1):1, 1996.

[148] D. Mahgerefteh, D. L. Butler, J. Goldhar, B. Rosenberg, and G.L. Burdge. Technique for measurement of the Raman gain coefficient in optical fibers. *Optics Letters*, 21(24):2026, 1996.

[149] C. Headley and G. P. Agrawal. Unified description of ultrafast stimulated Raman scattering in optical fibers. *Journal of the Optical Society of America B-Optical Physics*, 13(10):2170, 1996.

[150] M. N. Zervas and R. I. Laming. Rayleigh-Scattering Effect on the Gain Efficiency and Noise of Erbium-Doped Fiber Amplifiers. *IEEE Journal of Quantum Electronics*, 31(3):468, 1995.

[151] P. Wan and J. Conradi. Double Rayleigh backscattering in long-haul transmission- systems employing distributed and lumped fiber amplifiers. *Electronics Letters*, 31(5):383, 1995.

[152] C. Headley and G. P. Agrawal. Noise characteristics and statistics of picosecond Stokes pulses generated in optical fibers through stimulated Raman scattering. *IEEE Journal of Quantum Electronics*, 31(11):2058, 1995.

[153] S. Kumar, A. Selvarajan, and G.V. Anand. Nonlinear copropagation of two optical pulses of different frequencies in birefringent fibers. *Journal of the Optical Society of America B-Optical Physics*, 11(5):810, 1994.

[154] V. Chandrakumar, J. B. Thomine, and F. Pirio. Numerical simulations for power margins in soliton transmission-systems over transoceanic distances. *Optics Letters*, 19(20):1618, 1994.

[155] C. J. Anderson and J. A. Lyle. Technique for evaluating system performance using Q in numerical simulations exhibiting intersymbol interference. *Electronics Letters*, 30(1):71, 1994.

[156] K. Rottwitt, J. H. Povlsen, A. Bjarklev, O. Lumholt, B. Pederson, and T. Rasmussen. Noise in distributed Erbium-doped fibers. *IEEE Photonics Technology Letters*, 5:218, 1993.

[157] E. Kreyszig. *Advanced Engineering Mathematics*. Wayne Anderson, 7th edition, 1993.

[158] N. S. Bergano, F. W. Kerfoot, and C. R. Davidson. Margin measurements in optical amplifier systems. *IEEE Photonics Technology Letters*, 5(3):304, 1993.

[159] A. Hook. Influence of stimulated Raman scattering on cross-phase modulation between waves in optical fibers. *Optics Letters*, 17(2):115, 1992.

[160] A. C. Newell and J. V. Moloney. *Nonlinear Optics*. Addison-Wesley, CA, 1991.

[161] C.R. Menyuk. Raman effect in birefringent optical fibers. *Optics Letters*, 16(8):566, 1991.

[162] K. X. Liu and E. Garmire. Understanding the formation of the SRS Stokes spectrum in fused-Silica fibers. *IEEE Journal of Quantum Electronics*, 27(4):1022, 1991.

[163] K.J. Blow, R. Loudon, and S.J.D. Phoenix. Exact solution for quantum self-phase modulation. *Journal of the Optical Society of America B-Optical Physics*, 8(8):1750, 1991.

[164] A. Chaplyvy. Limitations on lightwave communications imposed by optical-fiber nonlinearities. *Journal of Lightwave Technology*, 8:1548, 1990.

[165] P. N. Butcher. *The Elements of Nonlinear Optics*. Cambridge Unversity Press, Cambridge, 1990.

[166] K.J. Blow and N. J. Doran. Soliton in optical fibres. In A.D. Boardman, editor, *Nonlinear Waves in Solid State Physics*, page 325. Plenum Press, New York, 1990.

[167] R. H. Stolen, J.P. Gordon, W.J. Tomlinson, and H. A. Haus. Raman response function of silica-core fibers. *Journal of the Optical Society of America B-Optical Physics*, 6(6):1159, 1989.

[168] S. T. Davey, D. L. Williams, B. J. Ainslie, W. J. M. Rothwell, and B. Wakefield. Optical Gain Spectrum of GeO_2-SiO_2 Raman Fiber Amplifiers. *IEE Proceedings-J Optoelectronics*, 136(6):301, 1989.

[169] K.J. Blow and B.P. Nelson. Observation of stimulated Raman scattering and nonlinear pulse broadening at 1.32 μm in monomode optical fibres. *IEE Proceedings, optoelectronics*, 134:161, 1987.

[170] M. Schubert. *Nonlinear Optics and Quantum Electronics*. John Wiley & Sons, 1986.

[171] J.P. Gordon. Theory of the soliton self-frequency shift. *Optics Letters*, 11(10):662, 1986.

[172] E. Desurvire, M. J. F. Digonnet, and H. J. Shaw. Thery and implementatin of a Raman active fiber delay line. *Journal of Lightwave Technology*, LT-4(4):426, 1986.

[173] R. Loudon. Theory of noise accumulation in linear optical-amplifier chains. *IEEE Journal of Quantum Electronics*, QE-21(7), 1985.

[174] A. H. Hartog and M. P. Gold. On the theory of backscattering in single mode optical fibers. *Journal of Lightwave Technology*, LT-2(2):76, 1984.

[175] J. Auyeung and A. Yariv. Spontaneous and stimulated Raman scattering in long low loss fibers. *IEEE Journal of Quantum Electronics*, QE-14(5):347, 1978.